Bridging the Gap in Radiative Transfer Modelling using O_2 A-Band Emissions in the Mesosphere

A Thesis Submitted to the
College of Graduate and Postdoctoral Studies
in Partial Fulfillment of the Requirements
for the degree of Master of Science
in the Department of Physics and Engineering Physics
University of Saskatchewan
Saskatoon

By

Caelia Gardiner

Permission to Use

In presenting this thesis in partial fulfillment of the requirements for a Postgraduate degree from the University of Saskatchewan, I agree that the Libraries of this University may make it freely available for inspection. I further agree that permission for copying of this thesis in any manner, in whole or in part, for scholarly purposes may be granted by the professor or professors who supervised my thesis work or, in their absence, by the Head of the Department or the Dean of the College in which my thesis work was done. It is understood that any copying or publication or use of this thesis or parts thereof for financial gain shall not be allowed without my written permission. It is also understood that due recognition shall be given to me and to the University of Saskatchewan in any scholarly use which may be made of any material in my thesis.

Requests for permission to copy or to make other use of material in this thesis in whole or part should be addressed to:

Head of the Department of Physics and Engineering Physics
116 Science Place
University of Saskatchewan
Saskatoon, Saskatchewan
Canada
S7N 5E2
Or
Dean
College of Graduate and Postdoctoral Studies
University of Saskatchewan
116 Thorvaldson Building, 110 Science Place
Saskatoon, Saskatchewan
S7N 5C9
Canada

Abstract

One of the brightest emission features in the spectral radiance of the atmosphere during the daytime is due to oxygen (O_2) emission. The A-band photochemical emission is found between 758 and 770 nm and is strongly dependent on the temperature in the mesosphere and lower thermosphere (MLT). It begins contributing above 40 km altitude near the stratopause, and is visibly dominant above 60 km. Typically, the study of photochemical emissions at this altitude does not require consideration of extensive scattering processes due to low atmospheric density. As a result, atmospheric models are historically divided between those capable of simulating absorption and multiple scattering processes below the stratopause, and those which can model simple radiative transfer and photochemical emission in the MLT.

The MATS (Mesospheric Airglow/Aerosol Tomography and Spectroscopy) mission is designed to study gravity waves in the MLT and their effect on the structure of polar mesospheric clouds (PMCs). Because of the desire to observe aerosols in the upper atmosphere, an atmospheric model capable of accurately simulating both scattering and emission is required. The original SASKTRAN radiative transfer model was designed in support of the OSIRIS (Optical Spectrograph and Infra-Red Imaging System) instrument on the Odin satellite, and is only capable of modelling absorption and multiple scattering processes, with no inclusion of photochemical emissions. The purpose of this thesis is to design a photochemical emission model of O_2 in the A-band for integration into the original SASKTRAN framework to create an integrated model that handles emission and multiple scattering in a consistent fashion. The upgraded atmospheric model is capable of simulating radiance propagation through the MLT in the presence of PMCs, including absorption, scattering, and photochemical emission. As a result, radiance can be accurately simulated through the entire atmosphere, bridging the gap in atmospheric models that were previously divided between the lower and upper atmosphere. While the primary motivation for this work is in support of the MATS project, the newly designed model has wider applications in any area of study that requires a comprehensive model of atmospheric processes.

Acknowledgements

I would like to express gratitude to the following people:

My supervisors Dr. Adam Bourassa and Dr. Doug Degenstein for their support and guidance throughout my undergraduate degree, summer research positions, and post-graduate work.

The extra help available from the Atmospheric Remote-sensing Group at the University of Saskatchewan: Seth Dueck, for providing the software work in implementing my model into SASKTRAN; Chris Roth and Daniel Zawada for helping me learn Python; and Kimberlee Dubé for listening to all my complaints and leading the way to the end.

My sisters Lauren and Jessie, my mother Jacquie, and my father Gerard: they have been consistently on my side throughout my academic career and are always ready to be my cheerleaders when it is most needed.

Damian, for helping me take care of myself when I am always trying to fit too many things into my life. No less significant is his contribution to proofreading and feedback on how to write and research.

Thank you.

Contents

List of Tables

List of Figures

List of Abbreviations

ARG	Atmospheric Remote-sensing Group
BRDF	Bidirectional reflectance distribution function
EM	Electromagnetic
HITRAN	High-resolution Transmission database
IR	Infrared
LOS	Line of sight
LTE	Local thermal equilibrium
MATS	Mesospheric Airglow/aerosol Tomography and Spectroscopy
MISU	Stockholm University's Department of Meteorology
MJD	Modified Julian date
MLT	Mesosphere and lower thermosphere
NASA	National Aeronautics and Space Administration
NIR	Near-infrared
NLC	Noctilucent
OSIRIS	Optical Spectrograph and Infra-Red Imaging System
PMC	Polar mesospheric clouds
SASKTRAN	Saskatchewan radiative transfer model
SIM	Spectral Irradiance Monitor
SMR	Sub-mm/Mm Radiometer
SOLSTICE	Solar Stellar Irradiance Comparison Experiment
SORCE	Solar Radiation and Climate Experiment
SRC	Schumann-Runge continuum
TP	Tangent point
UTLS	Upper troposphere and lower stratosphere
UV	Ultraviolet
VER	Volume emission rate

Chapter 1

Introduction

The atmospheric airglow is an easily observable phenomenon that occurs at higher altitudes, above about 40 km. It happens as a result of atoms and molecules de-exciting from higher energetic states by spontaneously emitting photons. The molecules are excited to the higher energy states via collisions with other particles and photochemical processes with the incoming radiation field. The number of excited molecules and the probability of them spontaneously emitting is related to the temperature of their environment and the incoming radiation field. Photons emitted by these particles have frequencies which are unique to the species and state that it is in. In this way, observing the photon emissions as a function of frequency provides an insight to the atmospheric state and photochemical dynamics of the mesosphere and lower thermosphere (MLT).

Earth's atmosphere is typically divided into four layers: the troposphere, stratosphere, mesosphere, and thermosphere. Each layer is defined by the direction of temperature gradient throughout, with a temperature inversion occurring at each boundary. Atmospheric pressure decreases exponentially with altitude. The lower layers of troposphere and stratosphere contain Earth's weather and ozone layer, making them important indicators of global climate. The mesosphere and thermosphere lie above, have much lower densities, and seemingly fewer dynamic processes. Historically, these layers have been the subject of fewer studies due to their larger disconnect with the Earth's surface and greater difficulty in observation. The boundary between the mesosphere and thermosphere, the mesopause, has also been generally thought of as a static atmospheric boundary, through which chemical and energy transport do not occur. However, it has

become apparent in recent years that atmospheric gravity waves may create large fluctuations above the MLT, creating significant variations in temperature. Because gravity waves mostly originate in the lower atmospheric layers, this is strong evidence that the mesopause cannot be treated as a static boundary and further research in this region is required to better understand global atmospheric processes.

The field of atmospheric spectroscopy explores the relationship between matter and light. Many atmospheric phenomena involve photonic emission or absorption, processes which are described by spectroscopic theory. Each atom or molecule has its own unique spectral signature due to its electronic structure and the nature of quantum mechanics. Photon emissions and absorptions represent energy transitions within a molecule which can be of electronic, vibrational, or rotational states. The oxygen molecule specifically emits from its second excited electronic state to ground state in a series of spectra named the atmospheric bands, for their common occurrence in atmospheric phenomena and being one of the first observed airglow features. One specific vibrational transition is named the A-band and contains multiple rotational transitions within. The O_2 A-band emission spectrum is centred around 762 nm in the near-infrared (NIR) and is highly sensitive to temperature fluctuations. Because of its strong visibility and temperature dependence, the A-band emission has historically been observed as a means of studying the atmospheric state and temperature at altitudes above 40 km.

Desired atmospheric parameters such as density of constituents and temperature are difficult to measure directly. Spectroscopic processes like the O_2 A-band emission provide light signatures that give clues as to the atmospheric states that produced them. Measuring the radiance spectra of the atmosphere to deduce other parameters is referred to as remote sensing, which requires both an instrument to measure the spectral radiance and a mathematical inversion technique coupled with a forward radiative transfer model to produce geophysical quantities. One such pair is the OSIRIS (Optical Spectrograph and Infra-Red Imaging System) instrument on the Odin satellite and the accompanying

Saskatchewan radiative transfer model, SASKTRAN (named in accordance with previous models in the field and for the SASKatchewan and TRANsfer parts of its description). OSIRIS is a limb-viewing satellite launched into a sun-synchronous polar orbit in 2001 meant to take radiance measurements of the scattered sunlight through the atmosphere across the ultraviolet, visible, and near-infrared areas of the spectrum. SASKTRAN is an atmospheric framework that runs the forward radiative transfer model to simulate radiance spectra for analysis of OSIRIS measurements. Pairing the two allows for inverse modelling to infer atmospheric state as retrievals from OSIRIS measurements of the radiance in the limb.

The MATS (Mesospheric Airglow/aerosol Tomography and Spectroscopy) mission involves designing an instrument for specific use in mesospheric remote sensing. The MATS instrument suite is intended to be launched on a microsatellite to take limb and nadir measurements in the ultraviolet (UV) and NIR regions of the electromagnetic spectrum. UV light scattered from aerosol particles in the MLT can be measured and analysed with tomography to reproduce a three-dimensional model of polar mesospheric clouds (PMCs) in the area. PMC structure is a strong indicator of atmospheric gravity wave effects near the mesopause, allowing the MATS instrument to effectively study gravity wave behaviour in the MLT. NIR measurements in the same region contain A-band emission data which is used to infer the temperature where PMCs are formed. The work presented in this thesis is done in support of the MATS project in order to provide a full forward model capable of simulating the observed radiance spectra near the mesopause.

Producing an accurate forward model of the O_2 A-band emission spectrum demands understanding of the photochemistry required to originally excite the O_2 molecule, the spectroscopic processes which predict the rate of spontaneous emission, and the radiative transfer theory to properly propagate that emission through the atmosphere. Chemical reactions are arranged to produce a density profile of the O_2 molecule excited to A-band

level, denoted O_2^A. This constitutes the O_2^A density photochemical model. Spectroscopy and radiative transfer theory are then used to calculate the rate of photon emission from O_2^A as a function of frequency and altitude. A spectrum of volume emission rate (VER) is found per altitude using the O_2^A density profile from the photochemical model. The final result of the emission model is a radiative source function due to photochemical emission which contains an emission spectrum for each altitude.

The previously mentioned SASKTRAN radiative transfer model was designed for use with the OSRISIS instrument to predominantly study phenomena in the upper troposphere and lower stratosphere (UTLS). Due to higher densities at these lower altitudes, excited species quickly lose their extra energy to molecular collisions and photon emission does not occur often enough to be measurable. As a result, models studying this region, like the original SASKTRAN model, are only required to accurately simulate molecular absorption and multiple solar scattering but not photochemical emission. Separate radiative transfer models have been used when studying mesospheric and thermospheric processes but are lacking in the ability to fully model absorption and multiple scattering features. The purpose of this thesis is to upgrade the original SASKTRAN radiative transfer model to incorporate the combined O_2 A-band photochemical emission model in order to accurately model absorption, multiple scattering, and photochemical emission at any altitude in the atmosphere. The result is the integrated SASKTRAN +A-band emission model, whose full functionality is required to simulate observed radiance spectra in the mesosphere where emissions occur but also in the presence of PMCs, where molecular absorption and scattering have significant effect.

The integrated SASKTRAN +A-band emission model is verified by comparing simulations with actual OSIRIS measurements. The full functionality of the integrated model is also demonstrated by producing simulations with increasing modes of complexity: single scatter, multiple scatter, including albedo, including photochemical emission, and finally simulating a PMC at the desired altitude. Temperature dependence of the A-band

emission spectrum is then confirmed via simulated measurements, confirming the efficacy of the SASKTRAN +A-band model in support of the MATS mission for studying mesospheric phenomena. In demonstrating its use for the MATS project, the SASKTRAN +A-band model is also shown to be a valuable tool in studying more layers of the atmosphere as a whole and therefore bridging the gap in UTLS and MLT radiative transfer modelling techniques.

Chapter 2 provides all background information required to understand the subsequent work. Chapter 3 outlines the theory behind the O_2^A density photochemical model, discussing production and loss mechanisms of the excited O_2^A, and values and references for all reaction rates. The O_2 A-band emission model is described in Chapter 4, where spectroscopy and radiative transfer theory is presented in deriving the photochemical source function required for the radiative transfer equation. Chapter 5 provides details on integrating the two models from Chapter 3 and 4 with the original SASKTRAN radiative transfer model to produce the integrated SASKTRAN +A-band emission model. Verification and application of the model is found in Chapter 6 with simulated MATS instrument observations confirming the value of the upgraded radiative transfer model in studying the phenomena of the MLT region.

Chapter 2

Background

O_2 photochemical emission in the A-band is an easily measurable feature of day glow which occurs predominantly in the mesosphere and lower thermosphere (MLT). Understanding this region of the atmosphere requires a foundation of knowledge regarding the common atmospheric phenomena observed and their connections to other atmospheric layers. Studying the O_2 A-band emission feature also requires a strong basis in molecular spectroscopy, especially as it applies to the atmosphere. Remote sensing of the atmosphere uses spectroscopic applications to measure phenomena like the O_2 A-band. Measured radiance spectra from remote sensing instruments can be interpreted using a radiative transfer model that help determine the atmospheric state at time of measurement. The MATS mission aims to use a microsatellite to measure the O_2 A-band emission feature at altitudes where polar mesospheric clouds (PMCs) occur in order to better understand atmospheric gravity wave structure. The work presented in this thesis focuses on providing a software model of A-band emission in support of the MATS project. Background information in the areas of atmospheric phenomena, spectroscopy, and remote sensing is therefore required to provide context for this research.

Information provided in this chapter is intended as a brief introduction to the subject areas described above. Some content has only a tangential relation and as such is included just for completeness, with the depth of discussion kept at an introductory level. Other material that serves as a more necessary foundation for the specific thesis work presented is only introduced in this chapter, with more details and theory provided in later chapters. An overview of the atmospheric layers and their processes is provided in Section 2.1, followed by specific discussions on the relevant mesospheric processes of airglow, polar

mesospheric clouds, and gravity waves. Section 2.2 gives a solid foundation of molecular spectroscopy theory and how it pertains to atmospheric study. The topic of remote sensing is discussed in Section 2.3 with further details given on the OSIRIS instrument, the SASKTRAN software modelling tool, and the MATS mission. This combination of topics provides a complete and comprehensive basis from which the theory and results of A-band emission modelling may be understood.

2.1 Atmospheric Phenomena

Earth's atmosphere is generally divided into four layers: the troposphere, stratosphere, mesosphere, and thermosphere. The distinction between these layers comes from the temperature gradients observed in each. As is seen in Figure 2.1, temperature decreases from the ground upwards into the troposphere. At the upper boundary of the troposphere, the tropopause, the temperature gradient reverses direction and begins increasing again throughout the stratosphere. Beyond the stratopause, temperature decreases again throughout the mesosphere until the mesopause, and then increases steadily to very high temperatures in the thermosphere. An in-depth discussion on features of these atmospheric layers can be found in Brasseur and Solomon (2005). The key points of these features are summarized below.

The troposphere is the closest layer to the Earth and extends to an altitude of 8 km around the poles and up to 18 km at the equator (an average height of 10 km is shown in Figure 2.1). The temperature decreases steadily upwards through this layer due to the exponential decrease in atmospheric pressure. A parcel of warm air rising adiabatically will expand with decreasing pressure and therefore become colder. The coldest temperatures at the tropopause may be -50°C at the poles or as low as -80°C at the equator. This layer contains approximately 75% of all the air in the atmosphere and almost all the water vapour. It is also heavily turbulent in air flow and thermodynamic processes. As warm air rises and is cooled, it may become denser than its surroundings and therefore may drop again, creating turbulence air flow patterns. Energy may also be carried from lower to higher altitudes through vaporization and condensation of water vapour. A parcel

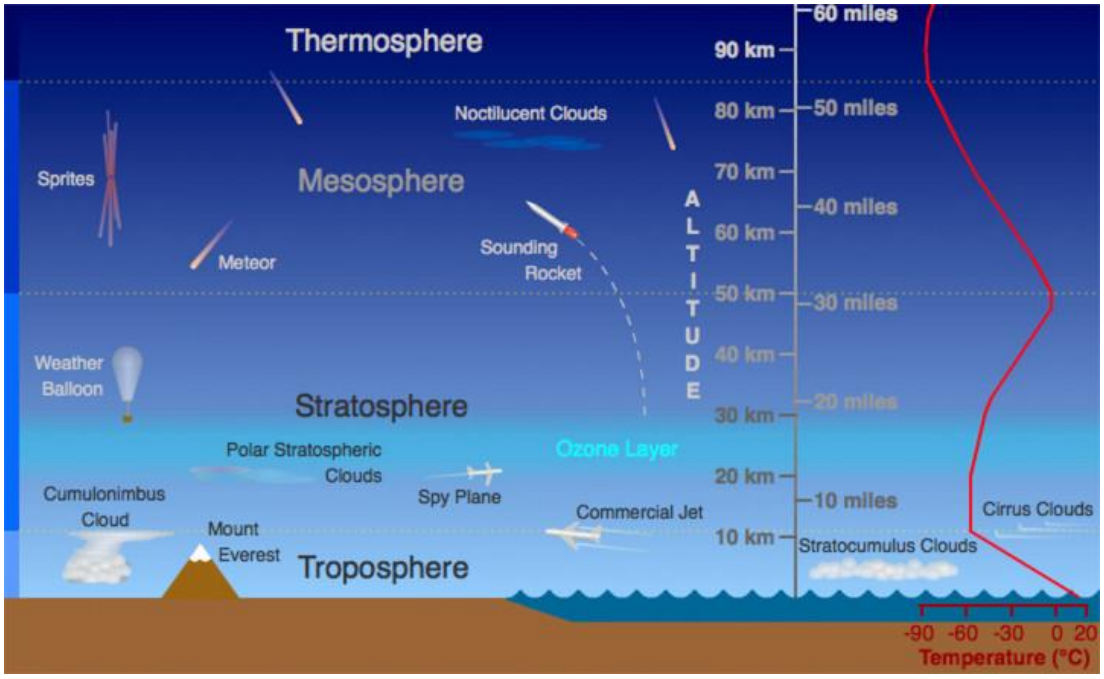

Figure 2.1: The atmospheric layers of the Earth illustrated with average global altitudes, temperature gradients, and common phenomena seen in each layer (UCAR, 2015).

of humid air at a low altitude may lose its water vapour content as it rises due to condensation. The process of condensation deposits energy higher in the troposphere in the form of latent heat. These dynamic processes are the reason Earth's weather occurs in the troposphere.

The stratosphere extends from the top of the tropopause to approximately 50 km altitude. This region contains the ozone layer, which is responsible for much of the Earth's radiative heating. Ozone absorbs sunlight in the ultraviolet (UV) region of the electromagnetic (EM) spectrum and may then radiate thermal energy in the infrared (IR), or photodissociate and impart heat via kinetic energy transfer with other atmospheric particles. Due to this process, the temperature increases from the tropopause upwards through the stratosphere, and can reach up to -3°C (Brasseur and Solomon, 2005). The rising temperature here provides atmospheric stability, in contrast to the turbulence observed in the troposphere. A parcel of air will not rise if the temperature above is warmer than below, preventing significant mixing. Commercial passenger jets tend to reach cruising altitude in the stratosphere to take advantage of the smoother air flow.

There is interest in the interactions between the troposphere and stratosphere. The regions surrounding the tropopause are commonly referred to as the upper troposphere and lower stratosphere (UTLS). In this region the air is fairly well mixed and therefore some cross-over occurs when studying weather (in the troposphere) and the ozone layer (in the stratosphere). Anthropogenic contributions are produced mainly in the troposphere but can be brought into the stratosphere and have significant effects on climate, due to increase in greenhouse gases and depletion in ozone. It is growing more important to study the processes in this region to help understand trends in climate and create policies to correct the damaging effect humans may have on the atmosphere.

Above the stratopause, the mesosphere may reach 80 to 100 km altitude (an average height of 85 km is shown Figure 2.1). Below this layer exists 99% of air density, so atmospheric pressure is extremely low. Temperature decreases again in this region due to the low density of molecules, especially decreasing amounts of ozone. The coldest temperatures in Earth's atmosphere are found at the top of this layer at the mesopause and can be as low as -140°C (Sheese et al., 2010). Because of the extremely low density, atmospheric airglow becomes apparent here (Section 2.1.1), and due to the extremely low temperatures, polar mesospheric clouds (PMCs) sometimes occur as well (Section 2.1.2).

The thermosphere is the outermost layer of the atmosphere, and essentially has the properties of outer space. The altitude of the thermopause varies wildly due to the very low air density, and can be anywhere from 200 to 1000 km. Despite the low pressure, this region is defined separately due the temperature increasing again upwards from the mesopause. This is only due to the exposure of particles to the higher energy x-ray and UV radiation coming from the sun. Because of this exposure, this region is subject to space weather phenomena, such as the aurora. The ionosphere exists within the thermosphere as well, and some satellites in low Earth orbits have flight paths within this region.

In the first three layers of atmosphere – the troposphere, stratosphere, and mesosphere – the major constituents are molecular nitrogen (N_2) at ~80% and molecular oxygen (O_2) at ~20%, with some trace gases. Therefore, the mean molecular weight of air does not vary much with altitude from Earth's surface to the mesopause. The composition in the

thermosphere is very different due to the increasing proportion of atomic oxygen (O), whose density becomes significant above 130 km. In the thermosphere, O_2 and N_2 disappear mostly due to photodissociation from solar radiation.

The region surrounding the mesopause is often referred to as the mesosphere and lower thermosphere, (MLT) which is typically between 50 and 100 km. Because the atmosphere below the MLT is considered well-mixed, and ionospheric processes are observed above, this layer has long been treated as a static boundary with no contained interactions or permeability (Rymdstyrelsen, 2016). However, recent study has revealed the significant dynamics that allow transfer of momentum and energy from below the mesopause into the thermosphere through processes in the MLT (Smith, 2004). Due to this external forcing, the MLT may be the atmospheric region where anthropogenic climate change produces its largest effect (Kramer, 2015). It is also an important driver in the thermosphere in terms of wave input. There have been increasing observations indicating links between thermospheric ionospheric responses to dynamical processes in the troposphere and stratosphere (Rymdstyrelsen, 2016). It is important to consider a comprehensive atmospheric model between all four regions in order to better understand the effect humanity has on the Earth's atmosphere as a global system over greater periods of time. The work in this thesis focuses on phenomena and processes in the MLT region to provide more information on the interactions at this boundary layer.

2.1.1 Airglow

Atmospheric airglow may be observed where air density becomes low enough that molecular collisions become rare. This allows excited species to live long enough to emit their excess energy as photons, contributing to a visible glow in the atmosphere (Figure 2.2). A full discussion of the physics and chemistry that contributes to the various wavelengths of airglow seen in the atmosphere is available in Khomich et al. (2008). The points relevant to this work are summarized below.

Figure 2.2: Nighttime panorama from the International Space Station. The green band above the horizon represents one type of atmospheric airglow, which is visible at certain wavelengths (NASA, 2015).

The mesosphere and thermosphere consist of the basic constituents of nitrogen (N_2), atomic oxygen (O), and molecular oxygen (O_2), with some hydrogen (H_2) and helium (He). There are small amounts of other components, like nitrogen monoxide (NO), carbon monoxide (CO), carbon dioxide (CO_2), dinitrogen oxide (N_2O), water vapour (H_2O), ozone (O_3), and nitrogen dioxide (NO_2). These trace gases contribute to photochemistry, energetics, and photonic emissions in the MLT. Solar radiation gives rise to numerous photochemical processes which in turn induce airglow. This glow occurs both in the day time (dayglow) and at night (nightglow), with different features during each period. Practically any kind of photonic emission that occurs in the atmosphere is dependent on the parameters defining atmospheric state, such as temperature, pressure, density of constituents, and incoming solar radiation. These sensitivities, combined with the relative ease of taking remote optical measurements as opposed to those in-situ, make airglow a valuable means of studying processes above 40 km altitude.

Excitation processes give rise to 25 significant systems of bands and 130 atomic emissions (Khomich et al., 2008). Emissions occur at specific wavelengths due to changes of energy within the particles. These energy transitions are due to electronic structure and vibro-rotational energy values and are discretized according to quantum mechanic rules.

The varying degrees of scale associated with each collection of energy transitions provides systems which contain multiple bands, and bands which contain multiple spectral lines. More details on these processes are included in Section 2.2.

The effect of airglow in some wavelength regions becomes noticeable above 40 km, though it is more generally significant between 80 and 270 km altitude (Khomich et al., 2008). As atmospheric density decreases, the probability of particle collisions follows. In addition, the thinning atmosphere allows more exposure of atmospheric constituents to direct sunlight. Atoms and molecules that are excited by solar radiation, or through other chemical processes, are less likely to de-excite by imparting their excess energy through a kinetic collision. Therefore, the probability of de-excitation via photonic emission increases and airglow occurs. Above 270 km, the air density becomes so low as to no longer produce easily measurable intensities of emissions.

Of particular interest in this work is the atmospheric emission band of the O_2 molecule, a result of an electronic transition between its second excited state and ground state (more details provided in Chapter 3). The atmospheric band, containing the A, B, and γ-bands, is one of the brightest features measurable in dayglow emissions, and has been extensively studied both theoretically and experimentally for almost 100 years (Babcock and Dieke, 1927; Babcock and Herzberg, 1948; Wallace and Hunten, 1968; Bucholtz et al., 1986). O_2 A-band emissions are valuable indicators of atmospheric temperature, which is of particular interest around the MLT where the lowest temperatures in Earth's atmosphere occur. This feature also provides information on the density of products that contribute to its intensity, such as O_3, O_2, and O. The status of these constituents in the MLT is often difficult to measure, making this feature an important tool in understanding the health of our atmosphere on a global scale.

The MATS mission aims to measure EM wavelengths in both the UV and near-IR (NIR) regions, in order to gather information about cloud scattering and airglow respectively. This thesis work is not concerned with the cloud scattering in the UV and instead is focused on the airglow observations in the NIR. MATS is specifically designed

to take measurements of the O_2 A-band emission in order to determine temperatures near the mesopause and in areas where PMCs are forming (Section 2.1.2).

2.1.2 Polar Mesospheric Clouds

While all of Earth's weather is in the troposphere and lower stratosphere, there is a rare type of cloud that exists near the top of the mesosphere. Because these are seen near the polar regions, they are referred to as polar mesospheric clouds, or PMCs (Figure 2.3). They have been observed for more than 100 years, as they can be viewed from the ground under twilight conditions when the sun is below the horizon but is illuminating them in the mesosphere. Because they are only visible from the ground at night, they are also given the name of noctilucent clouds (NLCs) (Cho and Rottger, 1997). Sweden has a latitude of approximately 60°N, at which point these clouds are very visible. Therefore, there has been historical interest in studying PMCs within Sweden contributing somewhat to the focus of the MATS project. While this phenomenon is not directly relevant to this work, discussion is included to provide a deeper understanding of the motivation behind the MATS mission.

Figure 2.3: Noctilucent clouds visible at sunset over Stockholm, Sweden (Videlov, 2014).

PMCs occur in both hemispheres near the summer solstice at high latitudes and in the MLT region, at approximately 82 km altitude (Alpers et al., 2000). The clouds are made of water ice particles that begin forming below the summer mesopause. At polar latitudes, summer mesopause temperatures are at their coldest and can decrease down to -140°C

(Alpers et al., 2000). These extreme temperatures allow water to freeze at such low densities as are present in the mesosphere, and so PMCs may form. Because the formation of these clouds is very sensitive to temperature and water vapour content, their existence is an excellent indicator of small changes in the global atmosphere (Alpers et al., 2000).

Aerosol particles scatter light with a cross-section that depends on the composition of particles, their aggregate state, the particle size, and the wavelength of incident light (Alpers et al., 2000). Measurement of scattered light from clouds of aerosols such as PMCs can provide details on cloud properties, improving our understanding of chemical processes in the lower atmosphere that affect changes in the mesosphere. It is for this reason that the MATS mission plans to measure relevant wavelengths in the UV to better understand the structure and state of PMCs on a global scale.

2.1.3 Gravity Waves

It is widely accepted that atmospheric gravity waves are an essential part of the dynamics of the atmosphere on all meteorological scales (Nappo, 2002). They provide an important link between processes in the lower atmosphere (troposphere, stratosphere, and mesosphere) and the thermosphere and ionosphere by transporting energy and momentum through the MLT region. The topic of atmospheric gravity waves is quite broad and complex, and not the focus of this thesis. However, as with PMCs, a brief background is provided for completeness due to the purpose of the MATS mission. A comprehensive review of the subject is given by Nappo (2002), which is summarized here with emphasis on its relevance to this work.

Because Earth's atmospheric density increases with depth, from high to low altitudes, it may be referred to as a stably stratified fluid, a characteristic of which is its ability to propagate wave motions. There are two dominant processes determining the wave motion of atmospheric fluid: buoyancy and gravity. Due to gravity's contribution to the oscillatory nature of the fluid's motion, these waves are referred to as gravity waves. Gravity waves can occur in all shapes, sizes, and directions.

Gravity waves are typically generated in the troposphere and have a number of sources. Disturbances in the landscape, such as mountains and coastlines, force a horizontal flow

upward. Violent sources like volcanic eruptions suddenly provide vertical ejection of energy. Natural weather phenomena such as thunderstorms and cyclones promote an upward circulation of air that contributes to vertical oscillations. A parcel of air may be disturbed by any one of these sources, forcing it momentarily upward. The air parcel may then fall back down, overshooting its original position and oscillating about equilibrium. This on-the-spot oscillation creates a disturbance that propagates kinetically via molecular collisions vertically through the atmosphere, continuing in a wave-like motion. Energy is therefore provided by these sources in the troposphere, carried via gravity waves upward, and deposited elsewhere. This means of transport is much more rapid than if energy were carried by the mean flow processes of the atmosphere. Therefore, this wave motion is an extremely important component of atmospheric dynamics and contributes to the global atmospheric model.

Gravity waves cannot be seen by themselves but can only be studied by measuring the effects they have on the atmosphere. One such effect of particular interest to the MATS project involves the global coupling processes that govern the cold summer mesopause region (Rymdstyrelsen, 2016). Recent model studies show that gravity waves may create large fluctuations in the 100 to 300 km altitude region over spatial scales of tens to several hundred kilometers. These fluctuations may also be accompanied by temperature variations of 50 K or more and density variations as large as 25% (Rymdstyrelsen, 2016). The dissipation of these waves creates localized regions of heating and cooling over scales of several hundred kilometers. It is apparent that the effect of gravity waves on mesopause temperature alone is significant, let alone the effect on atmospheric modelling in general. These effects are of great interest to the larger MATS science team whose goal is to provide more data on gravity waves around the world.

2.2 Atmospheric Spectroscopy

Many of the phenomena discussed in Section 2.1 cannot be directly observed or easily measured. However, the relationship between particles and light in our atmosphere make it possible to perform remote sensing to infer information about desired parameters.

Spectroscopy refers to the study of interactions between matter and light and is a valuable tool in both measuring and modelling the layers of Earth's atmosphere. A full explanation and derivation of atomic spectroscopy, its rules, and relation to molecular spectroscopy may be found in Bernath (2005). The following discussion focuses more on molecular spectroscopy and how it relates to atmospheric study in both theory and practice. Along with the study of airglow, the subject of atmospheric spectroscopy is the main focus of this thesis work. More details on theory and application are provided in Chapter 4.

Due to its electronic structure and the nature of quantum mechanics, each elemental atom has its own unique spectral signature. It is capable of absorbing or emitting only specific wavelengths in the EM spectrum due to the transition properties of its electronic and rotational energy structure. The hydrogen atom is the simplest example of this, due to its only consisting of a single proton and companion electron. There are only two ways an atom may change energy levels: through electronic orbital transitions or changes in rotational energy. On the quantum scale, both of these energy spectra are discretized, and hence have only specific allowed states. Furthermore, the types of transitions between these energy states are limited to quantum mechanics transition rules. The spectral signature of hydrogen (Figure 2.4) represents both these sets of energy transitions occurring in all their allowable exchanges. Because every element is unique, there are unique energy structures and transitions permitted to each, producing unique spectral signatures.

In the case of molecules, the resulting spectrum relies on the structure of the constituent atoms as well as the geometric shape of the entire molecule. The geometry dictates symmetries or lack thereof in the molecular shape which places constraints on its allowed rotational movement. In addition, when more than one atom is bonded together, there comes another degree of freedom. Atomic bonds within a molecule are often modelled with spring-like properties, as the distance between them may compress and expand due to their energy levels. This type of movement is defined as vibrational energy and is the final

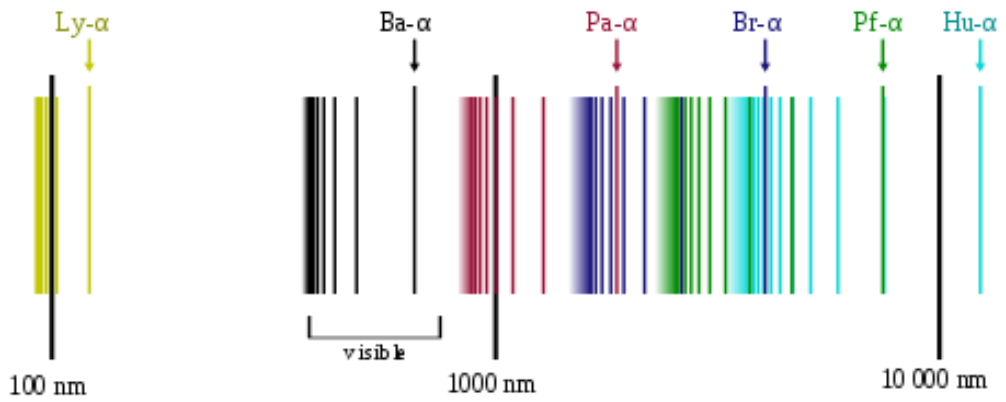

Figure 2.4: Hydrogen spectral series in logarithmic scale. Each line represents an energy transition from one energy state to another (OrangeDog, 2009).

quantized energetic degree of freedom experienced by molecules, along with electronic orbitals and rotational movement. Due to this work's interest in the oxygen molecule specifically, further discussion will be limited to molecular spectra rather than atomic.

Each of the three degrees of energetic freedom experienced by a molecule have different magnitude scales of energy. Transitions in electron structure, caused by electrons exciting or de-exciting to different orbitals within the molecule, require the largest amounts of energy. Figure 2.5 demonstrates the different energy levels allowed for a molecule attributed to electronic structure.

The next smallest energy scale occurs with vibrational energy transitions within the molecule. There are certain allowed vibrational states within each electronic structure. Therefore, any energy transition between two different electronic structures is further split by the allowable vibrational states. This splitting provides a finer structure to the original electron energy levels, demonstrated in Figure 2.6.

Lastly, the hyperfine spectral structure is governed by rotational energy quantum rules. Rotational energy transitions are on a much smaller scale, as each vibrational energy level has multiple allowed rotational states. This provides even further splitting from the original electronic structure and paints a complex picture for spectroscopic study of molecules. Figure 2.7 shows the three different categories of energy levels.

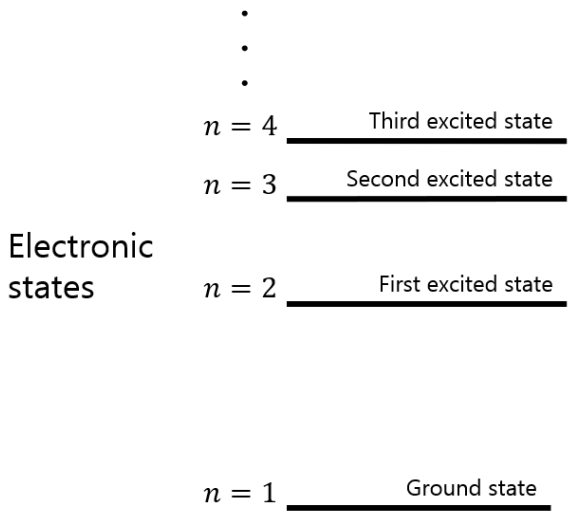

Figure 2.5: Electronic energy levels of an atom or molecule.

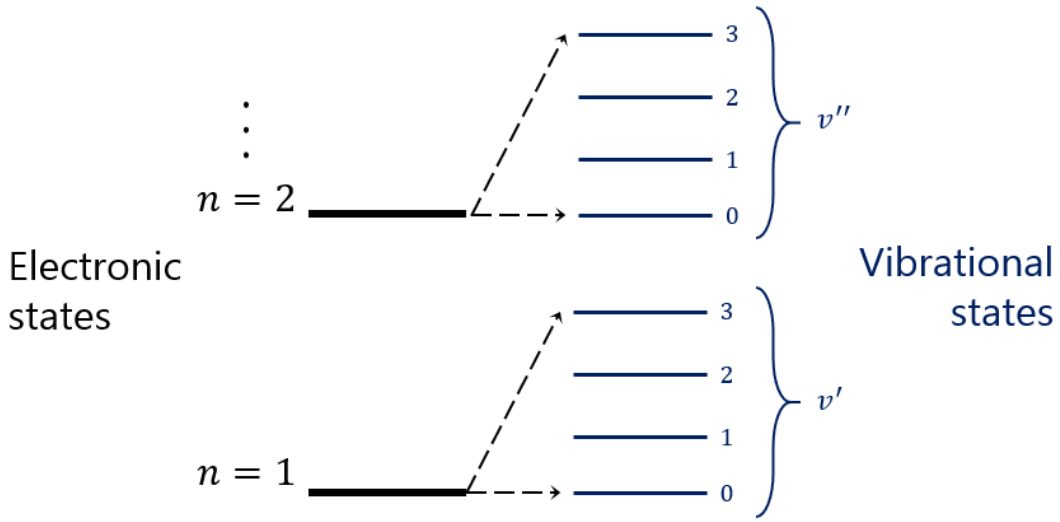

Figure 2.6: The vibrational energy states allowed for each electronic state.

Because each electronic energy level is host to multiple vibrational levels, which in turn contain many rotational transitions, electronic and vibrational transitions are referred to as spectral bands. Rotational transitions contain no finer structure and therefore are referred to as spectral lines rather than bands.

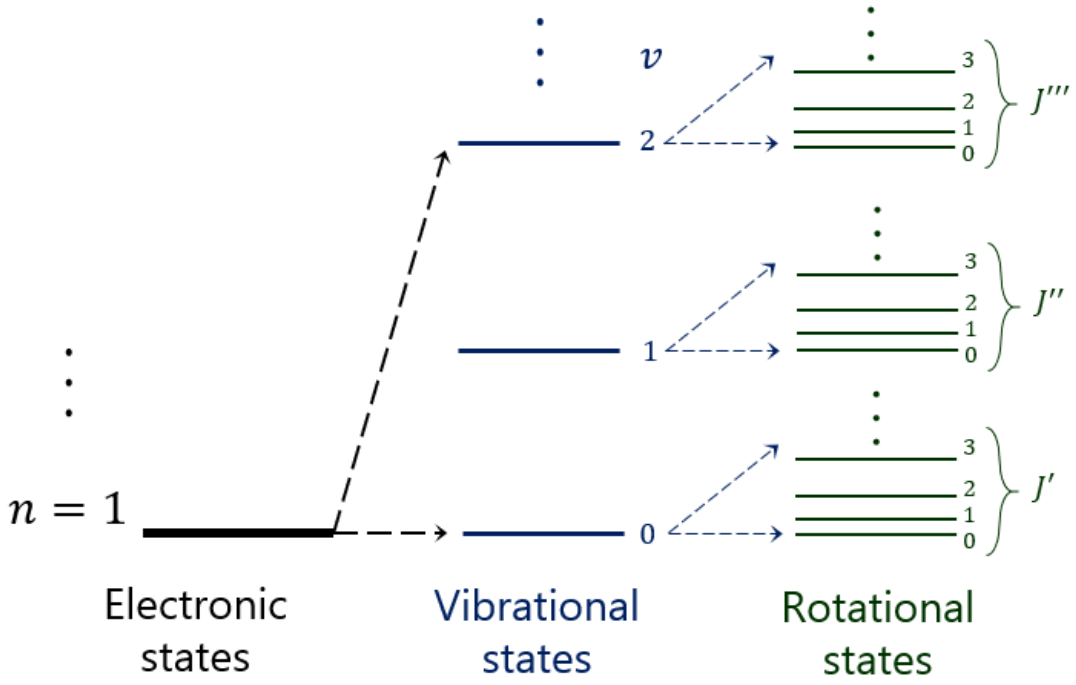

Figure 2.7: Multiple rotational states are permitted for each vibrational state, creating a very detailed picture of the allowed energy levels for a molecule.

All possible transitions may only occur due to absorptions or emissions of photons. Therefore, each transition is associated with a wavelength or frequency, and subsequently each molecule has a unique emission or absorption spectrum. The field of spectroscopy often deals with frequency in terms of wavenumber, with the value of each spectral line referred to as a transition wavenumber. While the central position of the spectral bands and lines described above are determined by quantum rules and therefore are non-variable for a specific molecule, the intensities with which emissions and absorptions occur at these wavelengths may vary depending on other factors. When viewing a plot of line intensities versus transition wavenumber, the rotational spectral lines appear as lobes arranged around a central vibrational wavelength. The number and shape of the lobes vary according to molecular geometry and environmental factors. An example of a two-lobed vibro-rotational spectral band is depicted in Figure 2.8.

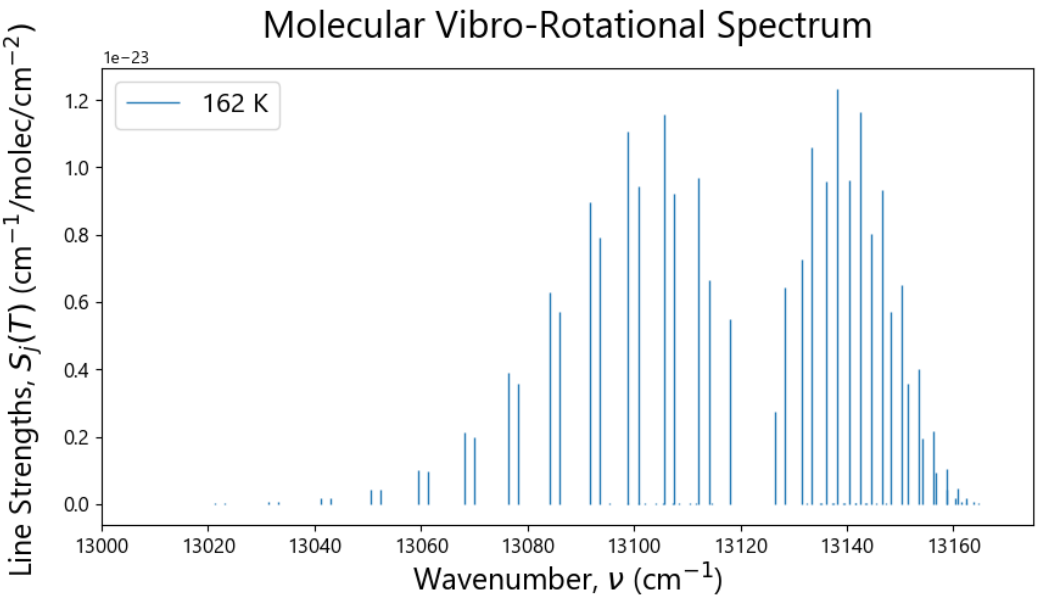

Figure 2.8: Two-lobed vibro-rotational energy transition spectrum. The central wavenumber represents the energy difference between two pure vibrational states. Each spectral line represents allowed transitions between rotational states.

For greater clarity on the relationship between the energy level diagram in Figure 2.7 and the spectral line intensity plot in Figure 2.8, consider a single vibrational energy transition, with multiple allowed rotational transitions (Figure 2.9). A true transition between $v = 0$ and $v = 1$ would produce a photon of some central wavelength, λ_{cent}, which would indicate a transition between $J' = 0$ and $J'' = 0$. Sometimes this type of transition is forbidden, in which case the closest wavelength transitions are between $J' = 0$ and $J'' = 1$ (labeled as λ_1), or $J' = 1$ and $J'' = 0$ (labeled as λ_2). In this way, the transition wavelengths are constructed for each molecule in a unique arrangement.

The intensities of the lines plotted in Figure 2.8 are proportional to the product of two things: the number of molecules excited to the energy levels involved in the transition, and the probability of a transition happening between the two levels. The population of energy states, N, decreases as the energy level increases according to the laws of thermodynamics and Boltzmann statistics. The probability of a transition occurring, P_{tran}, generally increases with the energy level due to the relative instability of higher energy states. Figure

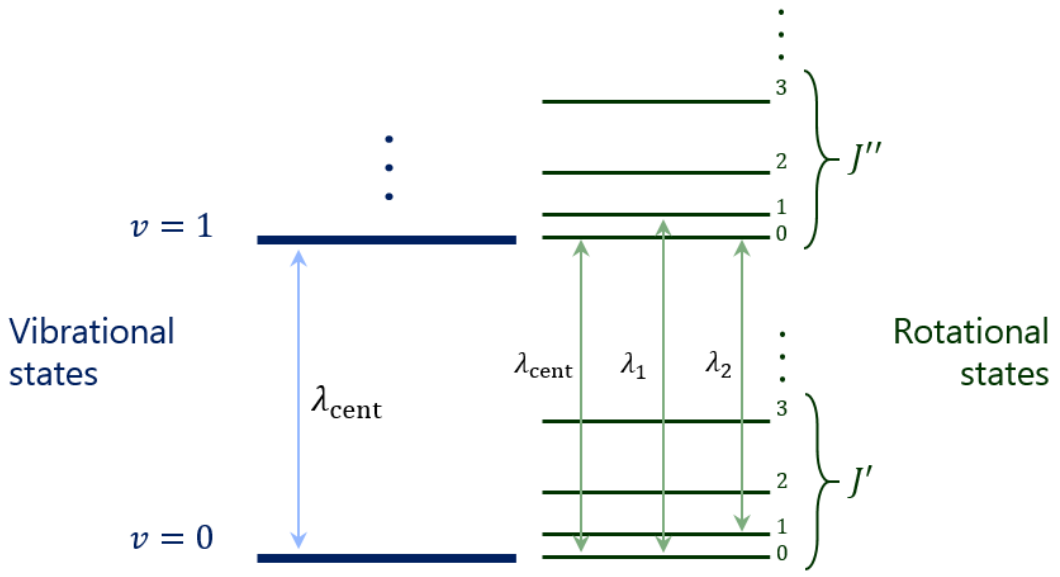

Figure 2.9: Transitions between energy levels are characterized by the wavelength of photon which would facilitate the transition. The pure transition between electronic or vibrational states is referred to as a central wavelength because the wavelengths of rotational transitions are arranged around it.

2.10 demonstrates these opposing trends and their product, which come together to produce a bell-curve. Each lobe pictured in Figure 2.8 is the result of this process. The number of lobes and how they are situated for each molecule is derived from the quantum rotational transition rules and is discussed in more detail in Chapter 4.

Notice in Figure 2.8 that the rotational spectral lines surround the central vibrational wavelength. The area closer to the centre is referred to as the core, and the tail ends of the lobes on the outside as the wings. The core of the spectrum includes the rotational energy transitions between lower rotational energy levels, and the wings represents transitions between higher rotational energy levels. Recall that line intensities are partly dependent on population of states, which in turn is dependent on temperature according to the Boltzmann distribution. The core region of spectral transition lines corresponds to population of lower energy levels, and therefore has greater intensities at lower temperatures when the lower energy states are more likely to be populated. Alternatively, higher temperatures allow population of energy levels further away from the centre,

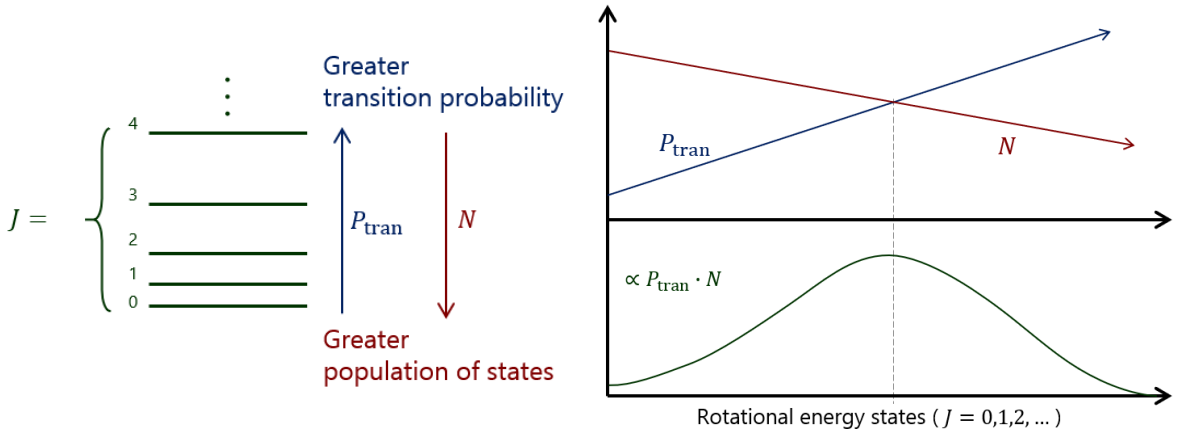

Figure 2.10: While the probability of a transition occurring increases with energy level, the population of states decreases (left). The opposing trends produce a product of a Gaussian shape (right), which is proportional to the lobes of spectral line intensity vs. wavelength in Figure 2.8.

subsequently increasing intensity at the wings rather than in the core. Figure 2.11 shows the effect that temperature has on the shape of a vibro-rotational spectral band with respect to temperature. Notice for lower temperatures, the lobes appear taller and narrower, whereas for higher temperatures, they are wider and flatter.

While the position of each spectral line is immovable for a given molecule, the spectral line intensities are heavily dependent on temperature and density of molecules in excited energy states. Temperature and density are fundamental properties of atmospheric state and the ability to determine these parameters is key in atmospheric study. Absorption and emission cross-sections of atmospheric constituents may be derived from their spectral line intensities and observable absorption and emission spectra are easily connected to their respective cross-sections. Therefore, spectroscopy provides an instrumental link between observable phenomena in the atmosphere and the initial atmospheric state that produced them, making it an important tool in atmospheric research. More detailed information as it pertains to the O_2 molecule and its emissions in the A-band is included in Chapters 3 and 4.

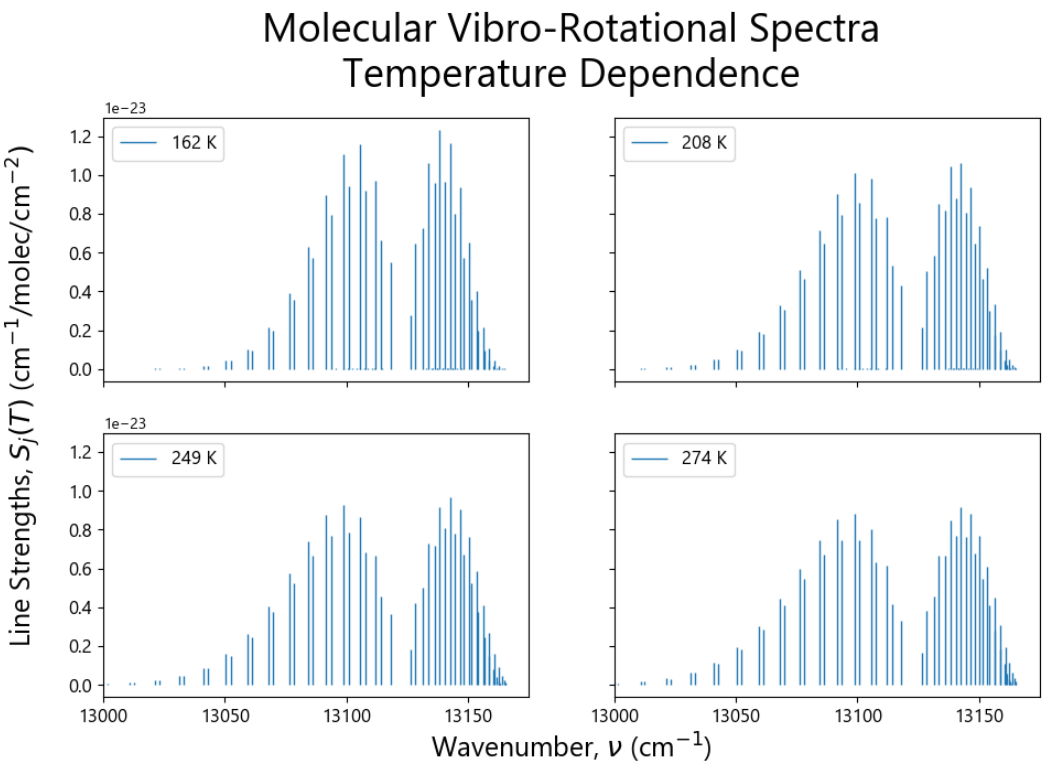

Figure 2.11: A two-lobed molecular spectral band depicting changes in temperature. At low temperatures, line intensities are greatest near the core due to population of lower energy levels. As temperature increases, higher energy levels are populated and line intensities in the wing regions increase in contrast with lines near the core. The shape of the spectral line intensity graph provides information on the temperature of molecules absorbing or emitting.

2.3 Remote Sensing Instruments and Tools

The processes by which light propagates through the atmosphere is described by radiative transfer theory, which is discussed in further detail in Chapter 4. Two significant processes that affect radiative transfer, especially in the MLT region, are atomic and molecular emission and absorption. It can be difficult to directly observe and study these processes, due to the relative difficulty in reaching higher altitudes in our atmosphere. Parameters of interest typically include the pressure and temperature variance with altitude, the composition of the atmosphere, and the density of its constituents. With more plentiful measurements of these parameters around the world at various altitudes, many atmospheric phenomena may be better understood, from weather to climate to aurora and

geomagnetic storms. Due to the links between matter and light given through spectroscopy, it is possible to measure the spectra of light as it propagates through the atmosphere and use these measurements to determine many of the desired parameters. This is the nature of atmospheric remote sensing. With comprehensive and powerful atmospheric models which incorporate radiative transfer and spectroscopy, optical data may be used inversely to infer the original state of the atmosphere.

Both instruments relevant to this thesis perform passive remote sensing on satellite platforms viewing on a tangent line through the atmosphere, referred to as the atmospheric limb (see Chapter 5 for more details). This limb geometry provides observations of incident light from the sun travelling through the atmosphere and gathered by the instrument. By spectrally resolving the measurements, this data provides information on the scattering properties of the section of atmosphere being viewed, as well as absorption and emission from species in the line of sight. Specific wavelength regions can be selected to identify the spectral signatures associated with desired species and produce plots of spectral line intensities as depicted in Figure 2.11, which may then be used as previously discussed to infer atmospheric state.

The work presented in this thesis is largely in support of the MATS mission, which is designed to measure light intensity in the UV and NIR regions of the EM spectrum. The spectrographic nature of the MATS instrument, combined with the viewing geometry through the limb, is reminiscent of an older spectrograph instrument designed by the Atmospheric Remote-sensing Group (ARG) at the University of Saskatchewan, named the Optical Spectrograph and Infra-Red Imaging System (OSIRIS). OSIRIS was launched on the Swedish satellite Odin and has been providing spectral data in the optical range from the troposphere to the MLT for 15 years. In conjunction, the SASKTRAN software model was designed to simulate OSIRIS measurements with high accuracy and has been used to produce many data products throughout the OSIRIS mission's lifetime. Many researchers involved with MATS have been involved with the OSIRIS and SASKTRAN projects over the years, giving it a strong heritage with the ARG research group and requiring a substantial understanding of the instruments and tools that come before. The work

presented in this thesis is designed as an addition to the existing SASKTRAN framework, and also uses OSIRIS measurements for verification of simulations. Some background material for each is provided here, along with further details on the MATS mission from Sweden.

2.3.1 OSIRIS on Odin

The Odin satellite was launched in 2001 into a near circular sun-synchronous orbit with an altitude of approximately 620 km. It orbits along the dusk-dawn terminator with a period of 96 minutes. The satellite originally served as a combined aeronomy/astronomy mission and includes two instruments: the Sub-mm/Mm Radiometer (SMR) and the Optical Spectrograph and InfraRed Imaging System (OSIRIS). While the SMR used for aeronomy is no longer functioning, the OSIRIS instrument is still operating, 15 years past its predicted end of life and data is still being gathered from it to this day (Llewellyn et al., 2004).

The OSIRIS instrument is designed to take measurements by viewing the atmospheric limb. Limb geometry consists of looking through the Earth's atmosphere along a tangent line, referred to as the line of sight. Limb viewing differs from occultation in that it does not require that the sun or moon be in the field of view. These types of observations contain information from a variety of scattering and photon emission sources that would be insignificant and immeasurable in occultation measurements. Scattered (single, multiple, albedo) and emitted photons may all enter the instrument's field of view along the line of sight (Bourassa et al., 2008). Figure 2.12 demonstrates the geometry and scattering sources of measurements taken by OSIRIS in the atmospheric limb. More details on the OSIRIS limb-viewing geometry are included in Section 2.3.2.

The Odin satellite which carries the OSIRIS instrument is designed to nod up and down along its flight path, allowing OSIRIS to remain unmoving and still provide vertical scans of the atmosphere. The Optical Spectrograph (OS) part of OSIRIS gathers data in the optical wavelength range from 280 to 810 nm with approximately 1 nm resolution (Roth

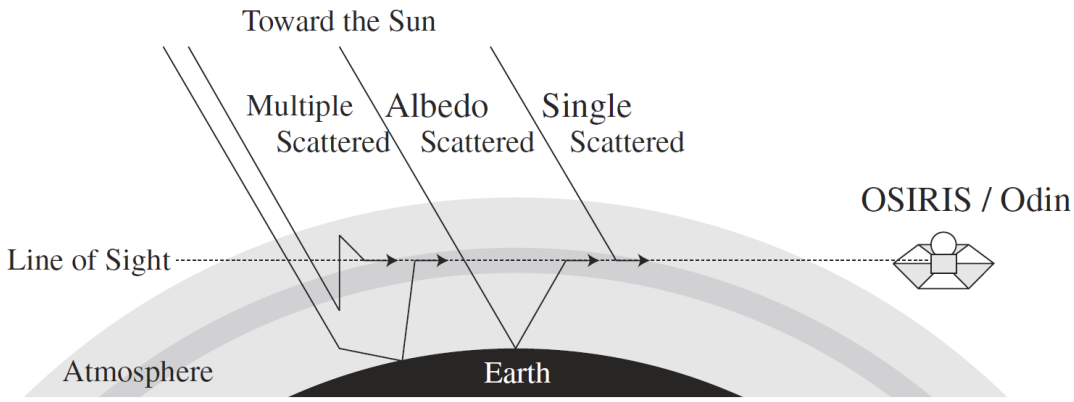

Figure 2.12: The limb scatter measurement technique (Bourassa et al., 2008).

et al., 2007). The satellite is capable of providing measurements from 7 to over 100 km altitude with measurements occurring every 1 km at lower stratospheric tangent altitudes, increasing to every 2 km at the highest tangent altitudes (Roth et al., 2007). Measurements made by the OS portion of OSIRIS are suitable for retrieval of temperature profiles, as well as number density profiles of both ozone and aerosol (Sheese et al., 2010; Sheese et al., 2011; Roth et al., 2007). Any comparisons or demonstrations done in this work will be from measurements taken by the OS instrument of OSIRIS.

While many of the spectral features visible in an OSIRIS measurement are due to scattering and absorption processes, some of the strong emission features become visible above 40 km altitude. The O_2 A-band emission feature has significant intensity in the MLT and can be easily observed in OSIRIS measurements. Figure 2.13a demonstrates a full OSIRIS spectrum measured at four altitudes, and Figure 2.13b provides a magnified plot of the A-band feature. Notice below 40 km O_2 exhibits strong absorption in this same band, which is to be expected in higher density regions with more frequent molecular collisions. It is this exact feature, from approximately 759 to 767 nm in the NIR region, that MATS is designed to measure.

2.3.2 The Original SASKTRAN Radiative Transfer Model

Shortly following the launch of the OSIRIS instrument on the Odin satellite, an accompanying radiative transfer model was developed. SASKTRAN is an atmospheric framework that runs the forward radiative transfer model to simulate radiance spectra for

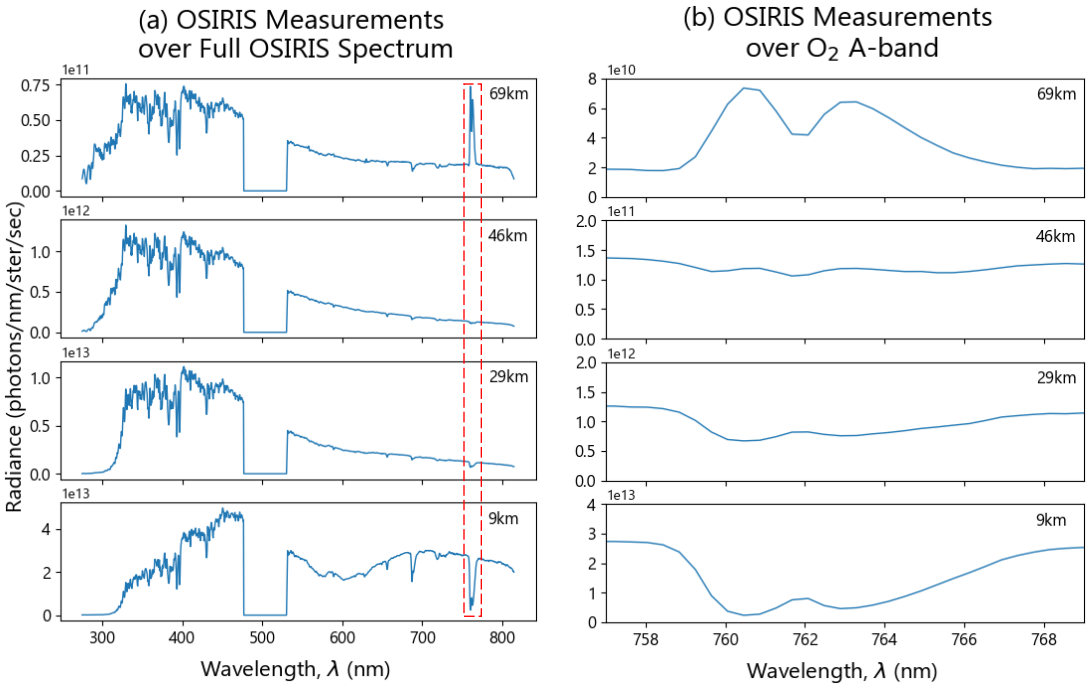

Figure 2.13: (a) OSIRIS measurements shown over the entire instrument spectrum, spanning the UV, visible, and NIR range, the red box highlighting the A-band region. (b) OSIRIS measurements of the atmospheric A-band, demonstrating emission contributions above 40 km altitude.

comparison with OSIRIS measurements (Figure 2.13) (Bourassa et al., 2007). These simulations are used to provide retrievals of atmospheric parameters through inversion processes (not discussed in this thesis). SASKTRAN uses the geometry of a spherical shell atmosphere of variable resolution, where each limb measurement of the OSIRIS instrument is characterized as a line of sight, each with a single tangent point to a corresponding spherical shell. The altitude at this tangent point is named the tangent altitude. A more detailed description of the SASKTRAN geometry is given in Chapter 5.

While many modifications have been made since its creation, before the work done in this thesis, SASKTRAN remained only capable of modelling scattering and absorption processes. Thermal or photochemical emissions as photon sources were not considered in the forward model. A background of this original SASKTRAN is provided here. More intricate details on the radiative transfer theory used in the SASKTRAN model are included in Chapter 4. Chapter 5 provides a discussion about the integration between the

original SASKTRAN model and the A-band photochemical emission model to produce the integrated SASKTRAN +A-band emission model.

The algorithm of the original model is outlined in detail by Bourassa et al. (2008) and summarized here. The model sums all radiance seen in the line of sight as an integrated value from the end of the straight-line path, or the line of sight, all the way to the observer using the radiative transfer equation,

$$I(\vec{r}_0, \hat{\Omega}) = \int_{s_1}^{0} J(s, \hat{\Omega}) \exp(-\tau(s,0))\, ds + \tilde{I}(s_1, \hat{\Omega}) \exp(-\tau(s_1,0)) \ , \tag{2.1}$$

where $I(\vec{r}_0, \hat{\Omega})$ is the radiance viewed by the observer, $J(s, \hat{\Omega})$ is the radiance source term, $\tilde{I}(s_1, \hat{\Omega})$ is any original radiance at the end of the path, and $\exp(-\tau(s,0))$ represents attenuation through the atmosphere due to the Beer-Lambert law due to atomic and molecular absorption. The path of the line of sight is set by s going from the end of path at s_1 and observer location at 0. Sources of radiation considered along the line of sight, $J(s, \hat{\Omega})$, are due to solar scattering. It is the operational purpose of the original SASKTRAN model to estimate the source function along the observer line of sight.

Original SASKTRAN uses a method of successive orders to apply this integration multiple times along rays traced in a spherical atmosphere. This process is initialized by the solar irradiance incident upon the atmosphere. The first order source term is produced by the first scatter of the solar beam (single-scatter). Light from this single-scattered source is propagated throughout the atmosphere and scattered again at all locations to produce the second order source term. The second source is scattered to produce the third order term, and so forth. For atmospheric scattering in the optical region, the magnitude of the terms diminishes quickly, and the algorithm typically converges within 8 to 10 orders. A key aspect of the SASKTRAN algorithm is a subdivision of the source terms, including ground radiance, by scattering order. Therefore, the user can decide to what order of scattering the model employs in the propagation.

The SASKTRAN model uses an Earth centred coordinate system defined by the polar axis and the prime meridian. In this coordinate system, the z-axis is directed from the

centre of the Earth to the North Pole, the x-axis points towards the prime meridian, and the y-axis is set according to a standard right-handed system. The surface of the oblate spheroid that represents the shape of the Earth is approximated to within 100 m of the gravitational shape of the Earth. By user configuration, the observer can be located anywhere in three-dimensional space looking in any direction. Solar position can be calculated with ephemeris software given the location and time or can be set explicitly. Configuration may also be set by defining the tangent point altitude and solar angles, and having the other parameters determined by the model.

The user may finally choose a wavelength range and resolution, as well as decide which atmospheric constituents to include in the modelling process. This wide range of choices, together with the successive orders method and accounting for ground-scattered radiation, makes the original SASKTRAN a unique and powerful tool useful for many applications in the field of aeronomy.

The SASKTRAN radiative transfer model was developed specifically to support efficient density profiles retrievals of aerosol and trace gases from limb scatter measurements (Bourassa et al., 2007). To obtain retrievals of atmospheric profiles, the forward model must be inverted to receive a radiance measurement and produce the original atmospheric state. Retrieval processes are complicated and varied, and not the subject of this work. More information on retrieval methods used with SASKTRAN are available in Bourassa et al. (2007) and Roth et al. (2007).

Since its conception, SASKTRAN has been used many times to help provide retrievals of atmospheric constituents, namely O_3 and aerosols (Roth et al., 2007; Bourassa et al., 2007; Degenstein et al., 2009; Bourassa et al., 2011; Bathgate, 2010). These retrievals are largely performed in the upper troposphere and lower stratosphere (UTLS), due to the interest of ozone and aerosol densities and their effect on climate. These types of studies have been strongly supported by the original SASKTRAN, as its multiple scattering and absorption considerations are dominant features in the UTLS. Photochemical and thermal emissions were not included in the original SASKTRAN model as they are typically

insignificant in these lower altitude regions due to the higher pressure and therefore higher rate of molecular collisions.

Retrievals of atmospheric profiles into the MLT have been performed by using other simpler radiative transfer models which also include emission features (Sheese, 2009; Sheese et al., 2010; Sheese et al., 2011). Temperature retrievals have been determined using radiance measurements of the O_2 A-band emission feature from the OSIRIS instrument (Figure 2.13). However, these previous works retrieve the temperature profiles using the O_2 A-band photochemical emission model along with a rudimentary radiative transfer model, ignoring multiple scattering. While this method is generally acceptable at altitudes above 40 km (Bucholtz et al., 1986), it is problematic when studying PMCs, which exhibit strong scattering due to aerosol content (Section 2.1.2). In support of future MATS measurements, the purpose of the work presented in this thesis is to integrate the O_2 A-band photochemical emission model into the original SASKTRAN, creating a more comprehensive atmospheric radiative transfer model named the integrated SASKTRAN +A-band emission model. This is not only beneficial for the study of PMCs, but also for other aerosols in the MLT, and for further study around the stratopause where photon emissions are no longer negligible.

2.3.3 The MATS Mission

Section 2.1.3 introduces atmospheric gravity waves and their importance in understanding dynamical processes that traverse the MLT. Gravity waves may not be directly observed and must be studied via the effects they have on the atmosphere. In order to study gravity waves in the MLT region, where they tend to deposit the energy sourced from below, atmospheric phenomena in the mesosphere must be observed. The O_2 A-band contribution to mesospheric dayglow (Section 2.1.1) is a bright emission feature in the NIR and easily measurable. The scattering of UV light off aerosol particles is a well-understood measurable process and can be used to derive properties of PMCs (Section 2.1.2). Both the density of excited O_2 molecules and the particles in PMCs are affected by the wave motion provided by gravity waves. Therefore, performing observations of these mesospheric phenomena allows indirect observation of gravity wave structure in the MLT.

The MATS (Mesospheric Airglow/aerosol Tomography and Spectroscopy) microsatellite mission aims to perform measurements in the UV and NIR for the purposes of recreating gravity wave structures in the MLT (Rymdstyrelsen, 2016). The project is funded by the Swedish National Space Board and being developed by Stockholm University's Department of Meteorology (MISU). While there are already multiple existing satellite missions taking global measurements of MLT structure, they only address a limited spatial range of the gravity wave spectrum. Figure 2.14 summarizes the capabilities of these existing instruments, with the red region illustrating the gap in data relevant to gravity wave study. The overlapping shaded area represents MATS's capabilities, which fill in the missing data at smaller vertical and horizontal wavelengths.

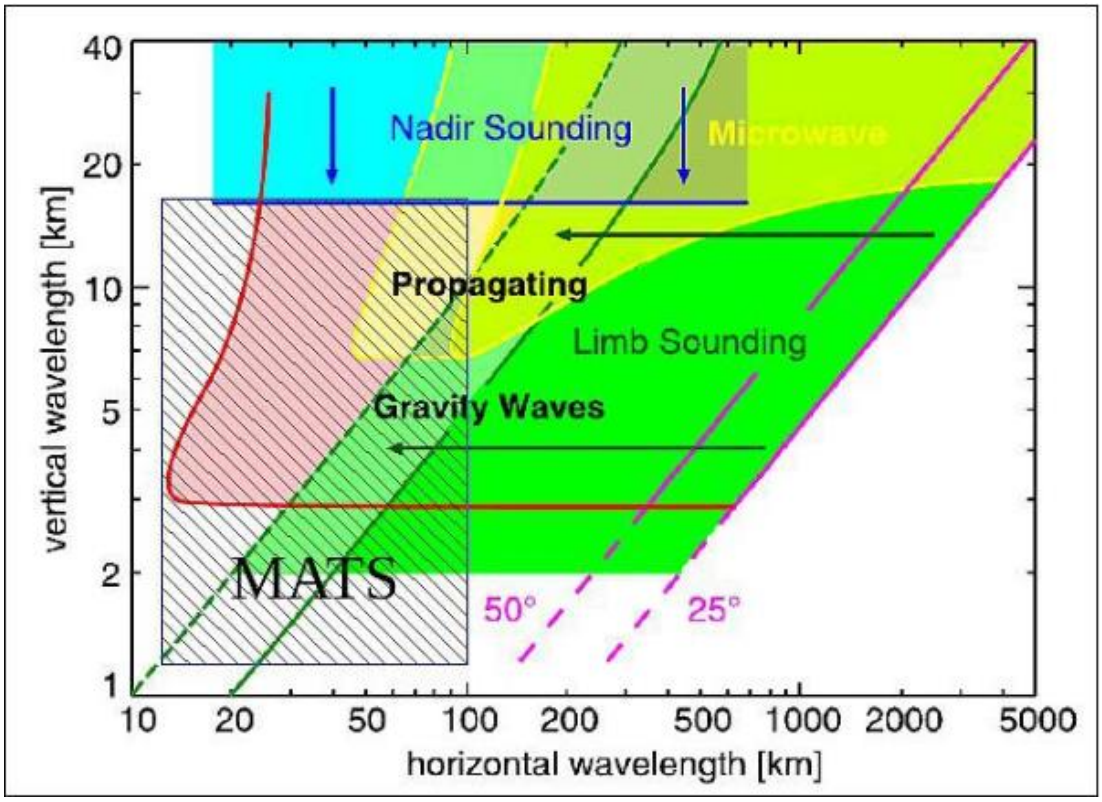

Figure 2.14: The red area represents the gap in the instrument coverage of gravity waves in the MLT region (Rymdstyrelsen, 2016).

MATS is preparing to launch as a secondary payload in the next few years into a sun-synchronous dawn-dusk orbit, at approximately 600 km altitude. It is designed to measure the two aforementioned atmospheric phenomena: photochemical emission in the O_2 A-band and scattered UV light from PMCs. This will be achieved by imaging the limb of the atmosphere in UV and NIR wavelengths, between the altitudes of 50 and 100 km (Rymdstyrelsen, 2016). By observing the mesosphere from many different directions, it is possible to tomographically reconstruct a three-dimensional picture of the existing structures (Figure 2.15) (MISU, 2016). Even more information can be obtained by combining tomography with spectroscopy. As discussed in Section 2.2, temperature profiles may be retrieved from measurements of the O_2 A-band emission spectra. Density and size of aerosol particles may be derived from measurements of scattered UV light. By collecting data from the mesosphere for a period of two years in bandwidths and spatial scales previously unmeasured, MATS will allow us to address a wide range of scientific questions about this remote part of the atmosphere.

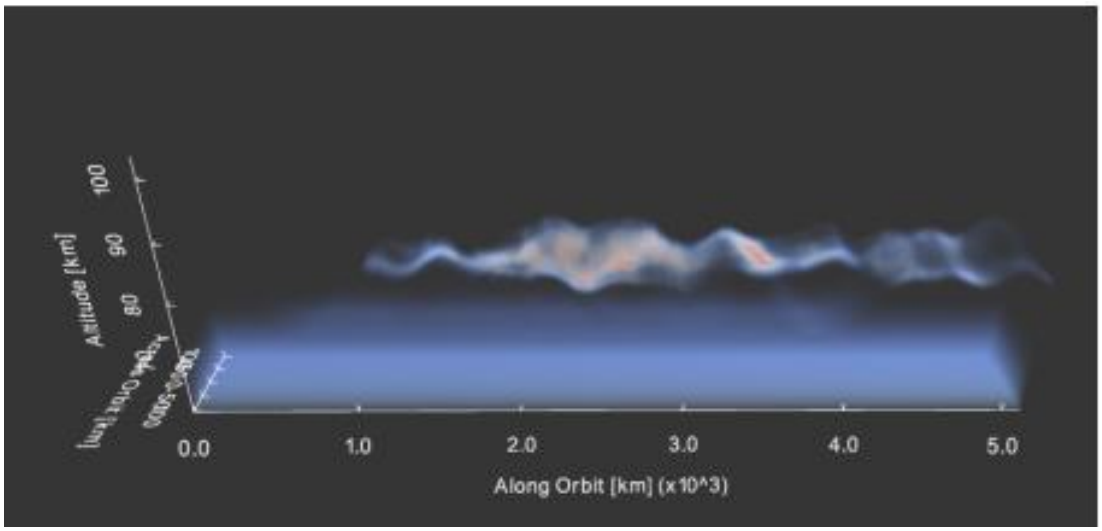

Figure 2.15: Recreated 3D model of NLC from simulated MATS measurements (MISU, 2016).

2.4 Chapter Summary

Earth's atmosphere is a multi-layered dynamic system that contains many phenomena, the study of which leads to better understanding of weather processes and our global climate. O_2 A-band emission is an easily observable atmospheric phenomena that contributes to the airglow in the mesosphere and lower thermosphere (MLT), where air density becomes low enough that molecular collisions become rare (Section 2.1.1). Polar mesospheric clouds (PMCs) occur around this altitude as well, appearing in both hemispheres near the summer solstice and at high latitudes (Section 2.1.2). Both the A-band emission feature and PMCs are valuable temperature indicators, specifically near the mesopause where the atmosphere reaches its lowest temperatures. Three-dimensional analysis of PMCs can also reveal gravity wave structures in the MLT, which require more study and cannot be directly observed (Section 2.1.3). The MATS mission intends to take measurements of scattered light at the altitude where PMCs occur in order to recreate the cloud structures for gravity wave research. Measurements of the O_2 A-band at the same altitudes will provide information on the temperature of the atmosphere where PMCs occur.

Measuring and modelling the processes which result in the A-band emission requires a background in molecular spectroscopy, especially as it pertains to atmospheric research (Section 2.2). Each molecule has its own unique spectral signature relating to its electronic structure and the quantum rules of vibrational and rotational energy transition (Figure 2.9). The A-band spectra of O_2 is particularly susceptible to temperature changes, making it extremely valuable for inferring the atmospheric state in the MLT. One instrument to have observed this feature is the OSIRIS instrument on the Odin satellite (Section 2.3.1), which takes measurements of scattering sunlight in the atmospheric limb (Figure 2.14). Radiance measurements can be simulated for comparison with the SASKTRAN radiative transfer model, which was designed for the OSIRIS mission and is capable of modelling an atmosphere with absorption and multiple scattering, but not photon emission (Section 2.3.2). The MATS instrument (Section 2.3.3) is designed to take radiance measurements in a region of the atmosphere where all three spectroscopic processes occur, so the

SASKTRAN model must be updated to include photochemical emissions in the A-band as a source function. The purpose of this work is to create a more comprehensive atmospheric radiative transfer model named the integrated SASKTRAN +A-band emission model, which is capable of modelling the A-band emission feature at altitudes in the MLT where PMCs occur to support future measurement analysis for the MATS project.

Chapter 3

The O_2^A Density Photochemical Model

In order to interpret measurements of the O_2 A-band emission spectrum, an accurate forward model of the process leading to the emission must be created. A-band photon emissions in the MLT are directly related to the amount of O_2 molecules excited to the necessary energy level, denoted O_2^A. The excited O_2^A density is easily modeled in a state of photochemical and thermal equilibrium as a combination of production and loss mechanisms in what is hereby referred to as the O_2^A density photochemical model. There are four subprocesses that contribute to the production of O_2^A and two subprocesses that dictate its loss. The result of the photochemical model presented in this chapter is the density of O_2^A above 40 km altitude in photochemical and thermal equilibrium on the period of time relevant to the emission process. Density is presented as profiles through the MLT, represented respectively with regards to each contributing process and as a total. The total density profile is further used in the following chapter to determine the photochemical emission source function required for radiative transfer modelling through the atmosphere.

Background information on general atmospheric spectroscopy is provided in the previous chapter. A more detailed discussion of molecular spectroscopy as it pertains to the O_2 molecule in atmospheric research is included in Section 3.1. Density of species is modelled using the continuity equation in certain states of equilibrium, which is stated in Section 3.2. Section 3.3 describes the four subprocesses that contribute to O_2^A production, and Section 3.4 explains the loss mechanisms. A short summary of the photochemical model and its results are provided in Section 3.5. The resultant density profiles are an

integral component in determining the amount of photon emission in the A-band and must be derived before attempting to model any radiative processes in the MLT.

3.1 The O_2 Atmospheric Bands

There are four main ways in which the internal energy of a molecule may change: translational kinetic energy (temperature), rotational kinetic energy, vibrational kinetic energy, and the distribution of electric charge within the molecule. In situations with local thermal equilibrium (LTE), collisions between molecules tend to equalize the distribution of the total internal energy. This ensures that for any given temperature above 0 K, a predictable percentage of molecules may be found in any given energy state, which means there is a predictable set of allowed transitions available within any macroscopic sample of gas. These allowed transitions correspond to quantized energy changes in terms of rotational, vibrational, and electronic energies. The electronic energy differences are typically the largest, followed by vibrational, and then rotational, and are characterized in terms of photon wavelengths or frequencies. The allowable wavelengths can be absorbed or emitted to change energy levels, and therefore make up the unique absorption or emission signatures of each molecule (Petty, 2006; Bernath, 2005).

Of interest for the oxygen molecule are the first three electronic states, denoted in spectroscopic notation as X (ground electronic state), a (first excited electronic state), and b (second excited electronic state). The molecular term symbol is used to further describe each level and has the relevant general form

$$^{2S+1}\Lambda^{(+/-)}_{(g/u)} \tag{3.1}$$

where S is the total spin quantum number, and Λ is the orbital angular momentum (where 0, 1, 2, 3 = Σ, Π, Δ, Φ). The superscript $(+/-)$ describes the reflection symmetry of the orbital state about the internuclear axis and is only necessary when $\Lambda = 0$ (Σ). Otherwise, all higher values of Λ exhibit twofold orbital degeneracy, including both + and – (denoted as $\pm$). Lastly, the subscript (g/u) gives the reflection symmetry of the electronic state about the molecular centre and is only needed for homonuclear diatomic molecules.

Because O_2 is a diatomic molecule with two of the same nuclei (homonuclear), all states of O_2 require this subscript symbol (Bernath, 2005). The molecular term symbols for the first three electronic states for O_2 are shown in Table 3.1.

Table 3.1: Molecular term symbols for first three electronic states of O_2.

Electronic state (symbol)	**Spin quantum number**	**Orbital angular momentum**	**Orbital state symmetry** (+/−)	**Electronic state symmetry** (g/u)	**Molecular term symbol**
Ground (X)	1 $(2S+1=3)$	$\Lambda = 0$ (Σ)	−	g	$O_2(X^3\Sigma_g^-)$
First (a)	0 $(2S+1=1)$	$\Lambda = 2$ (Δ)	N/A	g	$O_2(a^1\Delta_g)$
Second (b)	0 $(2S+1=1)$	$\Lambda = 0$ (Σ)	+	g	$O_2(b^1\Sigma_g^+)$

Transitions between the ground and the second excited state ($X \leftrightarrow b$) are referred to as the atmospheric band of O_2, so-called due to their being commonly observed in atmospheric research. This second excited state $O_2(b^1\Sigma_g^+)$ contains three allowed vibrational states, $v = 0, 1, 2$. The atmospheric band of O_2 consists of transitions from the ground state $O_2(X^3\Sigma_g^-, v = 0)$ to any of these three vibrational states. These three vibrational transitions are referred to as the A-band, B-band, and γ-band and each is associated with a central vibrational transition wavelength or wavenumber (Table 3.2, Figure 3.1). Because the full spectroscopic notation is cumbersome, these three excited energy states are hereby represented by shorthand as O_2^A, O_2^B, and O_2^γ.

Table 3.2: The atmospheric band of O_2 (Babcock and Dieke, 1927).

Spectral Region	**Transition**	**Central Transition Wavelength** (nm)	**Central Transition Wavenumber** (cm^{-1})
A-band	$O_2(X^3\Sigma_g^-, v = 0) \leftrightarrow O_2(b^1\Sigma_g^+, v = 0)$ (ground to zeroth vibrational state)	762	13 123
B-band	$O_2(X^3\Sigma_g^-, v = 0) \leftrightarrow O_2(b^1\Sigma_g^+, v = 1)$ (ground to first vibrational state)	689	14 749
γ-band	$O_2(X^3\Sigma_g^-, v = 0) \leftrightarrow O_2(b^1\Sigma_g^+, v = 2)$ (ground to second vibrational state)	629	15 898

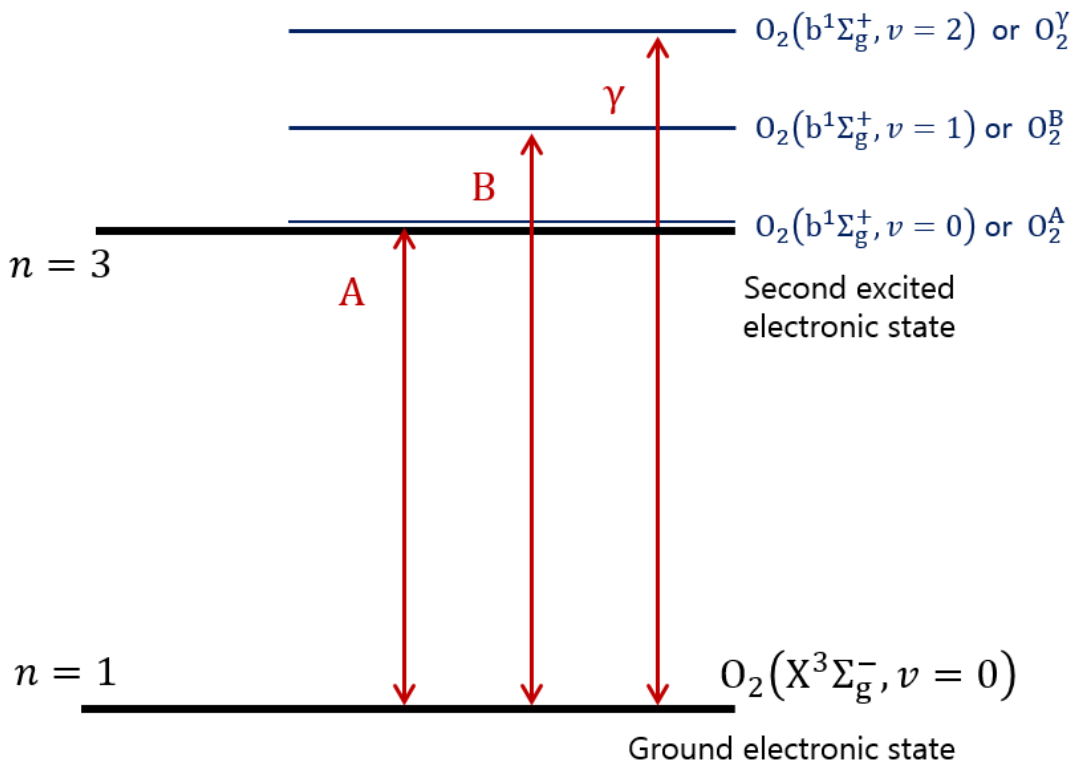

Figure 3.1: The three allowed vibrational states of the O_2 atmospheric band.

3.2 Density of O_2^A

Of the three vibrational transitions of the atmospheric band, the A-band is of most interest (electronic state transition from $v' = 0$ to $v'' = 0$). Because it is one of the brightest emission features in the near-infrared, it is easily observed and measured (background given in Section 2.1.1) (Bucholtz et al., 1986). The excited O_2^A molecule has a relatively long lifetime at ~12 sec, as compared to other excited molecular states (Babcock and Dieke, 1927). In a denser atmosphere, as in the troposphere or stratosphere, it loses its excess energy to collisions before it has time to spontaneously emit. Above 40 km altitude, the air density is low enough to begin to allow emissions to occur, making the A-band measurable (Bucholtz et al., 1986). The rate of A-band photon emission is directly proportional to the density of O_2^A (see Chapter 4), therefore it is essential to establish a model that can determine the density profile of O_2^A in a given atmospheric state.

The density of a chemical compound at a given point of the atmosphere is derived from the continuity equation (Brasseur and Solomon, 2005),

$$\frac{\partial[x]}{\partial t} + \nabla \cdot ([x]\vec{v}) = S_x \ , \tag{3.2}$$

where $[x]$ is the number density of a chemical species x, $\vec{v}$ is the velocity of mass flow through a volume of air, and S_x is the source function of species x. The first term on the left-hand side, $\partial[x]/\partial t$, describes the local rate of change of species density in time at a fixed point in space. The second term on the left-hand side, $\nabla \cdot ([x]\vec{v})$, represents the bulk motion of a species moving at group velocity $\vec{v}$. Due to the relatively short lifetime of O_2^A, as compared to transport processes, and the low density of air above 40 km, the effects of transport can be neglected, eliminating both terms on the left-hand side at steady state. This leaves the source function as

$$0 = S_x \ . \tag{3.3}$$

The net chemical source term, S_x (molec/cm^3/sec), can be expressed in terms of chemical productions and losses,

$$S_x = P_x - L_x[x] \ , \tag{3.4}$$

where P_x (molec/cm^3/s) describes gross chemical production of x, and L_x (s^{-1}) is the loss coefficient which is multiplied by the density of species. From Equations 3.3 and 3.4, the steady state density of a species can be determined in terms of its productions and losses. For the desired species at hand, O_2^A, the density profile (molec/cm^3) may be established as

$$\left[O_2^A\right] = \frac{P^{O_2^A}}{L^{O_2^A}} \ . \tag{3.5}$$

All chemical reactions occur at rates defined by their respective reaction rate coefficients. These may be denoted by variables A, k, g, or J, which each define a different type of process. Rate variables denoted by A are referred to as Einstein coefficients, which characterize spontaneous photon emission reactions in units of s^{-1}. Variables labeled k

represent either combination rates or quenching rates. Combination coefficients (s^{-1}) define the rate at which two separate products come together to produce a final combined product, whereas quenching coefficients (cm^3/s) describe the rate of collisional energy quenching between products. Photochemical reaction rates, represented by g (s^{-1}), are also called g-factors and belong with any photon absorption processes. Photolysis coefficients are denoted by J (s^{-1}) and indicate photodissociation reactions. All relevant rate coefficients are discussed with their respective reactions in the following Sections 3.3, 3.4, and 3.5, and listed at the end of this chapter in Table 3.3.

3.3 Production Mechanisms of O_2^A

There are four processes that have been found to contribute to the density of O_2^A above 40 km (Bucholtz et al., 1986):

1) Photon absorption in the A-band (resonant scattering), $P_1^{O_2^A}$.
2) Photon absorption in the B-band and subsequent quenching, $P_2^{O_2^A}$.
3) Collisional excitation of ground state O_2 from $O(^1D)$, $P_3^{O_2^A}$.
4) The two-step Barth process from two atomic oxygen, $P_4^{O_2^A}$.

The total production rate of O_2^A has units of molec/cm^3/s and is the sum of the production rates due to each of the above four processes,

$$P_{\text{tot}}^{O_2^A} = P_1^{O_2^A} + P_2^{O_2^A} + P_3^{O_2^A} + P_4^{O_2^A} \ . \tag{3.6}$$

The final O_2 vibrational transition process, absorption in the γ-band, is deemed negligible in comparison to A and B-band absorptions, and so is not considered for the purposes of this model (Bucholtz et al., 1986).

3.3.1 Photon Absorption in A-Band

The simplest mechanism of O_2^A production involves photon absorption in the A-band, around $\lambda = 762\ \text{nm}$ or $\nu = 13\,123\ \text{cm}^{-1}$ (Figure 3.2). The absorption imparts enough

energy to the ground state O_2 to excite up to the O_2^A electronic state. The chemical reaction is written as

$$O_2 + h\nu_{\text{A-band}} \rightarrow O_2^A \ . \tag{3.7}$$

The gross production rate due to this absorption is

$$P_1^{O_2^A} = g_A[O_2] \tag{3.8}$$

where g_A (s^{-1}) is the photochemical reaction rate, and $[O_2]$ (molec/cm^3) is the number density of ground state O_2. The reaction rate, g_A, is dependent on attenuated solar flux throughout the atmosphere and therefore must be calculated as a profile before use in the photochemical model (Section 4.3.3).

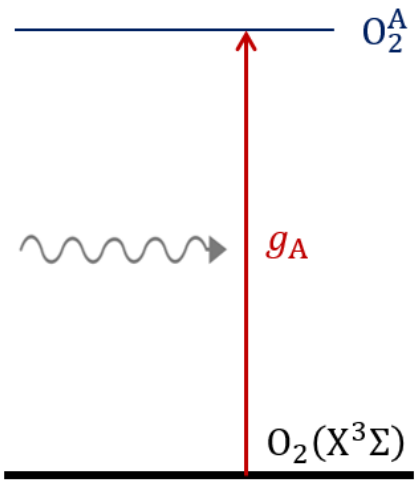

Figure 3.2: Photons are absorbed in the A-band by ground state O_2 with photon absorption reaction rate g_A to produce excited O_2^A.

3.3.2 Photon Absorption in B-Band and Subsequent Quenching

Another source of O_2^A comes from the more highly-excited O_2^B molecules. When ground state O_2 absorbs photons in the B-band, around $\lambda = 689\ \text{nm}$ or $\nu = 14\,749\ \text{cm}^{-1}$, it is excited to the second vibrational state in the atmospheric band, $O_2(b^1\Sigma_g^+, v = 1)$ or O_2^B. This has the chemical reaction and production rate equations respectively of

$$O_2 + h\nu_{\text{B-band}} \rightarrow O_2^B \tag{3.9}$$

$$P^{O_2^B} = g_B[O_2] \tag{3.10}$$

where g_B (s^{-1}) is the photochemical reaction rate of B-band absorption, and $[O_2]$ is again the number density of ground state O_2.

Molecules in the excited O_2^B state can de-excite to ground states of O_2 through various means, and in such a case not contribute to production of O_2^A. Spontaneous emission from the O_2^B molecule can occur in the 771 nm wavelength, to bring the molecule down to the first vibrationally excited ground state, $O_2(X^3\Sigma_g^-, v = 1)$.

$$O_2^B \rightarrow O_2\left(X^3\Sigma_g^-, v = 1\right) + h\nu_{771\,\text{nm}} \tag{3.11}$$

$$L_{\text{emi}}^{O_2^B} = A_{771} \tag{3.12}$$

The Einstein coefficient A_{771} (s^{-1}) describes the probability of spontaneous emission in the 771 nm wavelength (Table 3.3).

The excited O_2^B will also experience electronic quenching and become ground state O_2 when colliding and reacting with ozone, O_3.

$$O_2^B + O_3 \rightarrow 2O_2 + O \tag{3.13}$$

$$L_{O_3}^{O_2^B} = k_{3B}[O_3] \tag{3.14}$$

The quenching coefficient k_{3B} is in units of cm^3/s and is included in Table 3.3.

The desired O_2^A state is created when excited O_2^B undergoes collisional quenching with both O and O_2 (ground state), and nitrogen (N_2),

$$O_2^B + O, O_2, N_2 \rightarrow O_2^A + O, O_2, N_2 \ . \tag{3.15}$$

These reactions are mechanisms for both loss of O_2^B and production of O_2^A, and so each has an associated loss coefficient and production rate, with respective quenching coefficients

k_{0B}, k_{1B}, k_{2B} (cm^3/s) (Table 3.3). The total loss coefficient of O_2^B due to quenching is the sum of all the separate quenching loss coefficients due to O, O_2, N_2, and O_3,

$$L_{qu}^{O_2^B} = k_{0B}[O] + k_{1B}[O_2] + k_{2B}[N_2] + k_{3B}[O_3] \ . \tag{3.16}$$

The total production rate O_2^A due to B-band absorption and subsequent quenching of is the sum of each individual production rate,

$$P_{qu}^{O_2^A} = k_{0B}[O][O_2^B] + k_{1B}[O_2][O_2^B] + k_{2B}[N_2][O_2^B] \ . \tag{3.17}$$

The density profile of O_2^B can be determined using the same derivation from the continuity equation as in Equation 3.5,

$$[O_2^B] = \frac{P^{O_2^B}}{L^{O_2^B}} = \frac{g_B[O_2]}{A_{771} + k_{0B}[O] + k_{1B}[O_2] + k_{2B}[N_2] + k_{3B}[O_3]} \tag{3.18}$$

where $P^{O_2^B}$ is defined in Equation 3.10, and $L^{O_2^B}$ is the sum of the previously stated loss coefficients of O_2^B due to emission and quenching (Equations 3.12 and 3.16). Figure 3.3 illustrates all possible transitions that occur when producing the O_2^A excited state from photon absorption in the B-band.

3.3.3 Collisional Excitation by O(^{1}D)

The ground state of atomic oxygen is a triplet state with the notation O(^{3}P) and the first electronically excited state is the singlet O(^{1}D). This O(^{1}D) state can impart its energy via collisions with ground state O_2 to produce excited O_2^A molecules.

O(^{1}D) atoms are produced from photolysis of O_2 and O_3 molecules in specific bandwidths. The photolysis of O_2 occurs in the Lyman-α wavelength ($\lambda = 121.6$ nm, $\nu = 82\,237\ cm^{-1}$) (Equation 3.19) and in the Schumann-Runge continuum (SRC) ($130\ nm < \lambda < 175\ nm$, $57\,143\ cm^{-1} < \nu < 76\,923\ cm^{-1}$) (Equation 3.20). Photolysis of O_3 happens within the Hartley bands ($198\ nm < \lambda < 309\ nm$, $32\,362\ cm^{-1} < \nu < 50\,505\ cm^{-1}$). These chemical reactions are listed below with their respective production rates of the singlet oxygen, O(^{1}D).

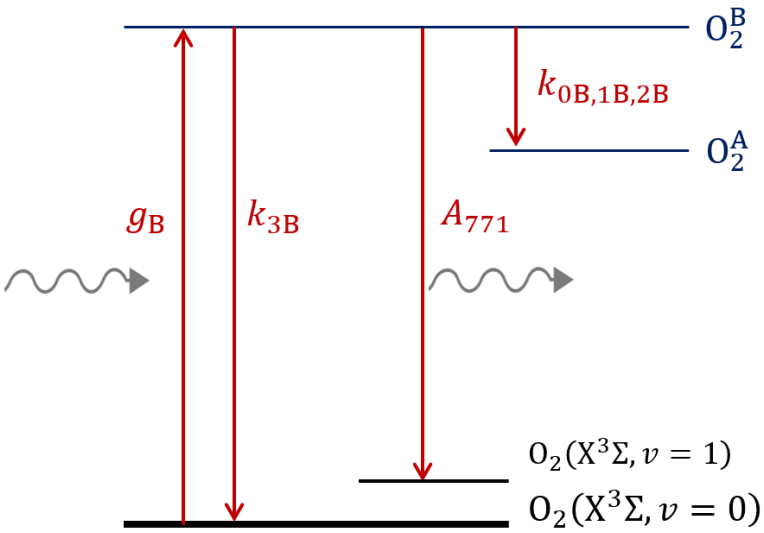

Figure 3.3: Photons are absorbed in the B-band by ground state O_2 with reaction rate g_B to produce excited O_2^B. O_2^B molecules are de-excited back to ground state through spontaneous emission with Einstein coefficient A_{771} and collisional quenching with O_3 with quenching rate k_{3B}. O_2^A is produced from O_2^B collisional quenching with O, O_2, and N_2 (quenching rates of k_{0B}, k_{1B}, and k_{2B} respectively).

$$O_2 + h\nu_{Ly\alpha} \rightarrow O(^1D) + O(^3P) \tag{3.19}$$

$$O_2 + h\nu_{SRC} \rightarrow O(^1D) + O(^3P) \tag{3.20}$$

$$O_3 + h\nu_{Har} \rightarrow O(^1D) + O_2(a^1\Delta) \tag{3.21}$$

The total production rate of singlet $O(^1D)$ due to photolysis is the sum of the production rates of each listed reaction above:

$$P^{O(^1D)} = J_L[O_2] + J_S[O_2] + J_H[O_3] \ . \tag{3.22}$$

The photolysis coefficients J_L, J_S and J_H (s^{-1}), like the g-factors in the previous two reactions, also depend on attenuated solar flux throughout the atmosphere and are therefore altitude dependent. Their profile calculation methods are explained in Section 4.3.3.

The excited singlet oxygen state O(^{1}D) can de-excite via spontaneous emission to its ground state via the reaction

$$O(^1D) \rightarrow O(^3P) + h\nu_{630\,nm} \tag{3.23}$$

with loss coefficient

$$L_{emi}^{O(^1D)} = A_{1D} \tag{3.24}$$

where A_{1D} (s^{-1}) is the Einstein coefficient for spontaneous emission in the 630 nm wavelength (Table 3.3). O(^{1}D) can also be lost due to collisional quenching with other atmospheric constituents,

$$O(^1D) + O_2, N_2 \rightarrow O(^3P) + O_2, N_2 \ , \tag{3.25}$$

with total loss coefficient

$$L_{qu}^{O(^1D)} = k_1[O_2] + k_2[N_2] \tag{3.26}$$

where values for the quenching coefficients k_1 and k_2 (cm^3/s) are listed in Table 3.3.

The excited state of O_2^A is produced by a certain percentage of the reaction in Equation 3.25. The production rate of O_2^A due to O(^{1}D) collision is then determined as a ratio φ (Table 3.3) of the production rate of any excited O_2*,

$$P_3^{O_2^A} = \varphi k_1[O_2][O(^1D)] \ . \tag{3.27}$$

The density profile of O(^{1}D) is determined again through the continuity equation (Equation 3.5),

$$[O(^1D)] = \frac{P^{O(^1D)}}{L^{O(^1D)}} = \frac{J_L[O_2] + J_S[O_2] + J_H[O_3]}{A_{1D} + k_1[O_2] + k_2[N_2]} \ , \tag{3.28}$$

where $P^{O(^1D)}$ is the sum of photolysis production rates in Equation 3.22, and $L^{O_2^B}$ is the sum of loss coefficients in Equations 3.24 and 3.26. Figure 3.4 illustrates the photolysis of O_2 and O_3 to create the excited O(^{1}D), which can then be lost to emissions or collisions, and can produce O_2^A from collisions with ground state O_2.

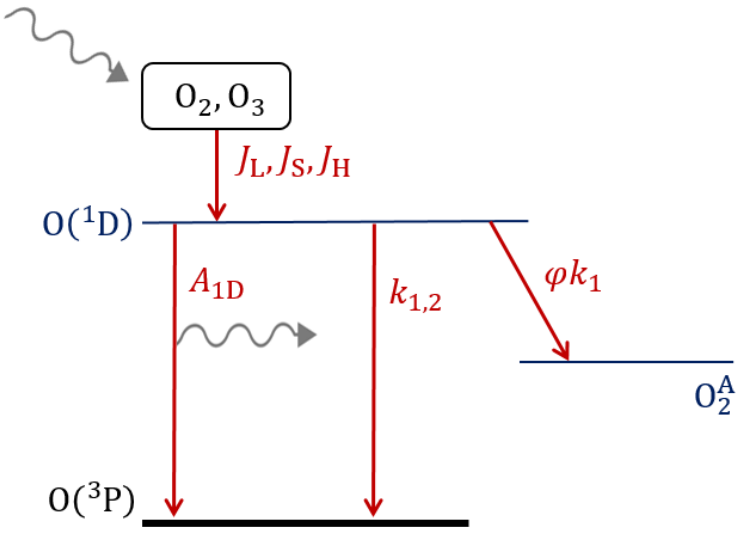

Figure 3.4: Photolysis of O_2 and O_3 produces excited singlet $O(^1D)$ with photolysis coefficients J_L, J_S, and J_H. Singlet $O(^1D)$ can be de-excited to its ground triplet state $O(^3P)$, due to spontaneous emission with Einstein coefficient A_{1D} or collisional quenching with O_2 or N_2 with quenching rates k_1 and k_2. The quenching reaction with O_2 can also produce excited O_2^A with the probably of quenching rate φk_1.

3.3.4 The Two-Step Barth Process

The fourth and final significant contribution to O_2^A density above 40 km is due to the recombination of O to make O_2. This was originally thought to occur in one reaction, as the Chapman reaction (Chapman, 1931),

$$O(^3P) + O(^3P) + O(^3P) \rightarrow O_2 + O(^1S) \ , \tag{3.28}$$

where $O(^3P)$ is the ground triplet state of O and $O(^1S)$ is the second electronically excited singlet state. Later, Barth and Hildebrandt (1961) proposed a two-step reaction,

$$O(^3P) + O(^3P) + M \rightarrow O_2^* + M \tag{3.29}$$

$$O_2^* + O(^3P) \rightarrow O_2 + O(^1S) \ , \tag{3.30}$$

where M is an atmospheric O_2 or N_2 molecule, and O_2* is an unknown excited state of the O_2 molecule. This two-step reaction is referred to as the Barth process and has been further

validated via laboratory and rocket experiments from Slanger and Black (1977) and Witt et al. (1978).

Photon emissions in the A-band have been observed in association with this mechanism, but not in a way that satisfies the identification of O_2^* as O_2^A (Witt et al., 1978). McDade et al. (1986) determines the production of the excited O_2^A state molecule as a quenched product of the more highly excited intermediate O_2^* state. The proposed transfer mechanism and derived production rate of O_2^A are summarized here.

Highly excited O_2^* is produced via recombination of atomic oxygen as is demonstrated in the first step of the Barth process in Equation 3.29. The production rate of O_2^* is

$$P^{O_2^*} = \alpha k_{1*}[O]^2[M] \tag{3.31}$$

where α is the ratio efficiency of the reaction and k_{1*} (cm^6/s) is the reaction rate of recombination. This highly excited O_2^* can be lost from quenching to ground state through collisions with other atmospheric constituents,

$$O_2^* + O_2, O, N_2 \rightarrow O_2 + O_2, O, N_2 \ , \tag{3.32}$$

and can also be lost due to spontaneous emission in an unknown frequency from the highly excited state down to ground state O_2 via the reaction

$$O_2^* \rightarrow O_2 + h\nu \ . \tag{3.33}$$

The total loss coefficient of the highly excited oxygen state O_2^* is then due to all the quenching reactions in Equation 3.32 and the emission reaction in Equation 3.33,

$$L^{O_2^*} = k_{2*}^{O_2}[O_2] + k_{2*}^{O}[O] + k_{2*}^{N_2}[N_2] + A_3 \ , \tag{3.34}$$

where coefficients $k_{2*}^{O_2}$, k_{2*}^{O}, and $k_{2*}^{N_2}$ (cm^3/s) are the quenching reaction rates, and A_3 (s^{-1}) is the Einstein coefficient for spontaneous emission in the unknown frequency.

The excited intermediate O_2^* can also be quenched, not only to ground state, but to the desired O_2^A state when colliding with ground state O_2, giving the production rate of O_2^A due to the Barth process,

$$O_2^* + O_2 \rightarrow O_2^A + O_2 \tag{3.35}$$

$$P_4^{O_2^A} = \gamma k_{3*}[O_2][O_2^*] \ , \tag{3.36}$$

where γ is the ratio efficiency of the reaction and k_{3*} (cm^3/s) is the quenching reaction rate. The density profile of O_2^* is defined again with the continuity equation (Equation 3.5),

$$[O_2^*] = \frac{P^{O_2^*}}{L^{O_2^*}} \ . \tag{3.37}$$

Here, however, there is some nuance. McDade et al. (1986) illustrates that there is some difficulty in determining the altitude profiles of the separate quenching rates $k_{2*}^{O_2}$, k_{2*}^{O}, and $k_{2*}^{N_2}$ in Equation 3.34 because the scale heights of O_2 and N_2 density are so similar that their separate components cannot be resolved. Therefore, the following approximation is used:

$$L^{O_2^*} = \alpha\gamma k_{3*}\left\{\frac{A_3}{\alpha\gamma k_{3*}} + C^{O_2}[O_2] + C^{O}[O]\right\} \tag{3.38}$$

where C^{O_2} and C^{O} are dimensionless fitting coefficients. Note here that the N_2 density profile is treated as a ratio with the O_2 profile and included in the C^{O_2} fitting coefficient.

Substituting Equations 3.31 and 3.38 into Equation 3.37, the coefficient α is eliminated,

$$[O_2^*] = \frac{k_{1*}[O]^2[M]}{\gamma k_{3*}\left\{\frac{A_3}{\alpha\gamma k_{3*}} + C^{O_2}[O_2] + C^{O}[O]\right\}} \ , \tag{3.39}$$

allowing the production rate of O_2^A due to the Barth mechanism from Equation 3.36 to become:

$$P_4^{O_2^A} = \frac{k_{1*}[O]^2[M][O_2]}{\frac{A_3}{\alpha\gamma k_{3*}} + C^{O_2}[O_2] + C^{O}[O]} \ . \tag{3.40}$$

It was further determined by McDade et al. (1986) that spontaneous emission is responsible for less than 10% of the total loss of O_2^*, allowing its related term $A_3/\alpha\gamma k_{3*}$ in the denominator to be neglected, and providing the final production rate of O_2^A as:

$$P_4^{O_2^A} = \frac{k_{1*}[O]^2[M][O_2]}{C^{O_2}[O_2] + C^{O}[O]} \quad . \tag{3.41}$$

The recombination reaction rate k_{1*} and fitting coefficients C^{O_2} and C^{O} are included in Table 3.3 with values and references. The density profile of M is taken to be the sum of the O_2 and N_2 density profiles. Figure 3.5 shows the two-step Barth process, from the recombination of atomic oxygen to produce higher level O_2^* to the quenching to produce desired O_2^A.

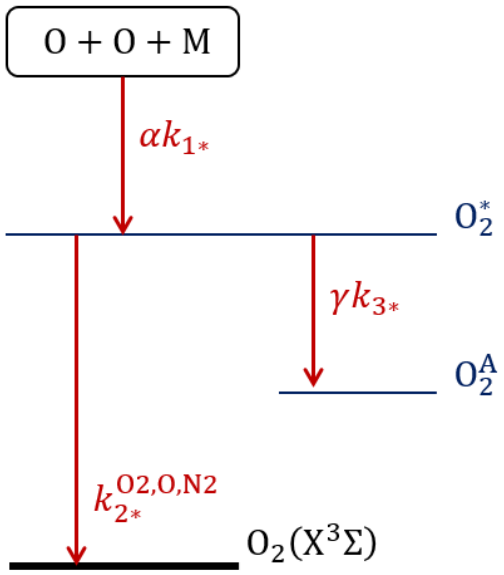

Figure 3.5: The two-step Barth process involves combination of atomic oxygen produces a highly excited state of O_2 with reaction rate αk_{1*}. The highly excited O_2^* can de-excite to ground state O_2 via collisions with O, O_2, and N_2 with respective quenching rates k_{2*}. The less excited O_2^A state can then be produced by the collisional reaction with O_2 with the reaction rate γk_{3*}.

3.4 Loss Mechanisms of O_2^A

The excited electronic state O_2^A can be lost to two different processes (Bucholtz et al., 1986). The first process is that which produces the desired A-band photon through spontaneous emission,

$$O_2^A \rightarrow O_2 + h\nu_{A\text{-band}} \tag{3.42}$$

$$L_{emi}^{O_2^A} = A_{1\Sigma} \ , \tag{3.43}$$

where $A_{1\Sigma}$ (s^{-1}) is the Einstein coefficient for spontaneous emission in the A-band, spectrally averaged over the entire wavelength range (Table 3.3). The second process is through electronic quenching with atmospheric constituents,

$$O_2^A + N_2, O_3, O_2, O \rightarrow O_2 + N_2, O_3, O_2, O \tag{3.44}$$

$$L_{que}^{O_2^A} = k_{1A}[N_2] + k_{2A}[O_3] + k_{3A}[O_2] + k_{4A}[O] \ , \tag{3.45}$$

where k_{1A}, k_{2A}, k_{3A}, and k_{4A} (cm^3/s) are quenching coefficients whose values are listed in Table 3.3. The total loss coefficient for the electronically excited O_2^A molecule is the sum of loss coefficients in Equations 3.43 and 3.45,

$$L^{O_2^A} = A_{1\Sigma} + k_{1A}[N_2] + k_{2A}[O_3] + k_{3A}[O_2] + k_{4A}[O] \ . \tag{3.46}$$

3.5 Model Summary and Results

The density profile of the excited O_2^A molecule can be determined through implementation of the photochemical model outlined in this chapter (Bucholtz et al., 1986). The steps are summarized below.

1) Input density profiles are required for N_2, O_3, O_2, and O, as well as atmospheric temperature profiles. Chapter 5 discusses the nature of these inputs in more detail, while Chapter 6 provides data sources.

2) All values of rate coefficients are required. The spontaneous emission coefficients and reaction rates for combination and quenching processes, represented by A and k respectively, are either single values or simply calculated based on temperature profiles. These values are listed with references in Table 3.3. The photon absorption rates and photolysis coefficients, denoted by g and J, are dependent on attenuated solar flux and require more extensive calculation. More details on these factors are given in Section 4.3.3, although they are also listed for completeness in Table 3.3.

3) The total production rate of O_2^A, $P_{tot}^{O_2^A}$ (Equation 3.6), must be calculated. It is the sum of the four processes outlined in Section 3.3, culminating in Equations 3.8, 3.17, 3.27, and 3.41, which are listed again here.

$$P_{tot}^{O_2^A} = P_1^{O_2^A} + P_2^{O_2^A} + P_3^{O_2^A} + P_4^{O_2^A} \tag{3.47}$$

$$P_1^{O_2^A} = g_A[O_2] \tag{3.48}$$

$$P_2^{O_2^A} = (k_{0B}[O] + k_{1B}[O_2] + k_{2B}[N_2])[O_2^B] \tag{3.49}$$

$$P_3^{O_2^A} = \varphi k_1[O_2][O(^1D)] \tag{3.50}$$

$$P_4^{O_2^A} = \frac{k_{1*}[O]^2[M][O_2]}{C^{O_2}[O_2] + C^{O}[O]} \tag{3.51}$$

4) The total loss coefficient of O_2^A, $L^{O_2^A}$, may be determined as a sum of the loss processes described in Section 3.4 and is given in Equation 3.46.

$$L^{O_2^A} = A_{1\Sigma} + k_{1A}[N_2] + k_{2A}[O_3] + k_{3A}[O_2] + k_{4A}[O] \tag{3.52}$$

5) The density of O_2^A is given by the continuity equation in Equation 3.5 and is a ratio of the values calculated in steps 3 and 4 above.

$$[O_2^A] = \frac{P^{O_2^A}}{L^{O_2^A}} \tag{3.53}$$

Figure 3.6 illustrates the density profiles of O_2^A due to each of its four contributive processes, as well as the total profile. Note that the production profile due to collisional excitation with $O(^1D)$ is separated to show the source of the photolysis (from O_2 or O_3). The results presented in Figure 3.6 are produced by atmospheric parameters chosen for verification purposes with OSIRIS measurements. Details on the chosen inputs are given in Chapter 6. Table 3.3 contains all necessary chemical reaction rates with their references and units.

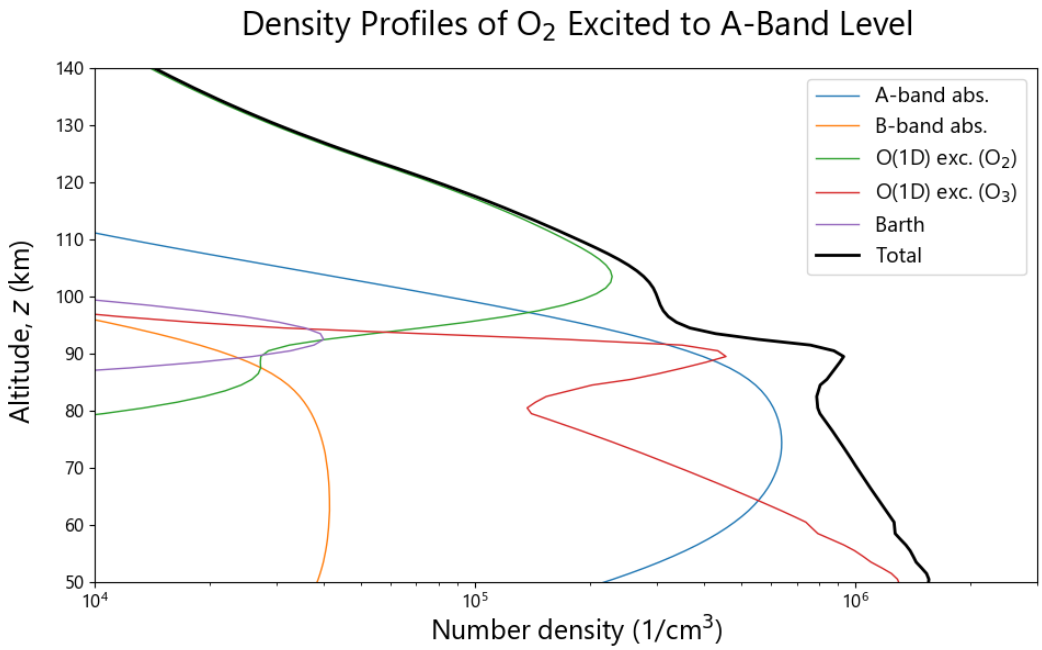

Figure 3.6: Number density of O_2^A as altitude profiles due to each contributing photochemical process.

Table 3.3: Reaction rates and coefficients necessary for completion of the O_2^A density photochemical model.

Reaction Description	Reaction Equation & Number	Rate Variable	Value & Reference
Section 3.3.1 – Photon Absorption in the A-Band			
Photon absorption in the A-band	$O_2 + h\nu_A \rightarrow O_2^A$ Equation 3.7	g_A	See Section 4.3.3
Section 3.3.2 – Photon Absorption in the B-Band			
Photon absorption in the B-band	$O_2 + h\nu_B \rightarrow O_2^B$ Equation 3.9	g_B	See Section 4.3.3
Spontaneous emission from O_2^B excited state	$O_2^B \rightarrow O_2 + h\nu_{771}$ Equation 3.11	A_{771}	0.070 s^{-1} (Yankovsky and Manuilova, 2006)
Collisional quenching of O_2^B	$O_2^B + O_3 \rightarrow 2O_2 + O$ Equation 3.13	k_{3B}	3.0 x 10^{-10} cm^3/s (Yankovsky and Manuilova, 2006)
Collisional quenching of O_2^B	$O_2^B + O \rightarrow O_2^A + O^*$ Equation 3.15	k_{0B}	4.5 x 10^{-12} cm^3/s (Yankovsky and Manuilova, 2006)
Collisional quenching of O_2^B	$O_2^B + O_2 \rightarrow O_2^A + O_2^*$ Equation 3.15	k_{1B}	4.2 x 10^{-11} exp(-312/T) cm^3/s (Yankovsky and Manuilova, 2006)
Collisional quenching of O_2^B	$O_2^B + N_2 \rightarrow O_2^A + N_2^*$ Equation 3.115	k_{2B}	5.0 x 10^{-13} cm^3/s (Yankovsky and Manuilova, 2006)
Section 3.3.3 – Collisional Excitation Due to O(^{1}D)			
Photolysis of O_2 in Lyman-α line	$O_2 + h\nu_{Ly\alpha} \rightarrow O(^1D) + O(^3P)$ Equation 3.19	J_L	See Section 4.3.3
Photolysis of O_2 in Schumann-Runge cont.	$O_2 + h\nu_{SRC} \rightarrow O(^1D) + O(^3P)$ Equation 3.20	J_S	See Section 4.3.3
Photolysis of O_3 in Hartley bands	$O_3 + h\nu_{Har} \rightarrow O(^1D) + O_2(a^1\Delta)$ Equation 3.21	J_H	See Section 4.3.3
Spontaneous emission from O(^{1}D) excited state	$O(^1D) \rightarrow O(^3P) + h\nu_{630}$ Equation 3.23	A_{1D}	6.81 x 10^{-3} s^{-1} (Kernahan and Pang, 1975)
Collisional quenching of O(^{1}D)	$O(^1D) + O_2 \rightarrow O(^3P) + O_2^*$ Equation 3.25	k_1	3.3 x 10^{-11} exp(55/T) cm^3/s (Sander et al., 2006)
Collisional quenching of O(^{1}D)	$O(^1D) + N_2 \rightarrow O(^3P) + N_2^*$ Equation 3.25	k_2	2.15 x 10^{-11} exp(110/T) cm^3/s (Sander et al., 2006)
Collisional excitation of O_2 to O_2^A	$O(^1D) + O_2 \rightarrow O(^3P) + O_2^A$ Equation 3.25	φk_1	φ = 0.95 (Green et al., 2000)

Section 3.3.4 – Two-Step Barth Process			
Combination of atomic oxygen	$O(^3P) + O(^3P) + M \rightarrow O_2^* + M$ Equation 3.29	k_{1*}	4.7 x 10^{-33} exp(300/T)^2 cm^6/s (McDade et al., 1986)
Collisional quenching of highly excited O_2^*	$O_2^* + O_2, O, N_2 \rightarrow O_2 + O_2, O, N_2$ Equation 3.32	C^{O_2}, C^O	6.6, 19 (McDade et al., 1986; Sheese, 2009)
Section 3.4 – Loss Mechanisms of O2A			
Spontaneous emission from O_2^A excited state	$O_2^A \rightarrow O_2 + h\nu_A$ Equation 3.42	$A_{1\Sigma}$	0.085 s^{-1} (Burch and Gryvnak, 1969)
Collisional quenching of excited O_2^A	$O_2^A + N_2 \rightarrow$ products Equation 3.44	k_{1A}	1.8 x 10^{-15} exp(45/T) cm^3/s (Sander et al., 2006)
Collisional quenching of excited O_2^A	$O_2^A + O_3 \rightarrow$ products Equation 3.44	k_{2A}	3.5 x 10^{-11} exp(-135/T) cm^3/s (Sander et al., 2006)
Collisional quenching of excited O_2^A	$O_2^A + O_2 \rightarrow$ products Equation 3.44	k_{3A}	3.9 x 10^{-17} cm^3/s (Sander et al., 2006)
Collisional quenching of excited O_2^A	$O_2^A + O \rightarrow$ products Equation 3.44	k_{4A}	8.0 x 10^{-14} cm^3/s (Sander et al., 2006)

3.6 Chapter Summary

The A-band of the O_2 molecule is one of three vibrational transitions allowed in the second electronic state transition named the atmospheric band (Section 3.1, Figure 3.1). A-band emissions are observed when the O_2 molecule is excited to this electrovibrational state, denoted O_2^A, and spontaneously emits to de-excite to ground level. The density of excited O_2^A molecules is therefore of interest and can be modelled with the continuity equation at steady state (Section 3.2). In the case of photochemical and thermal equilibrium, and in the period of time where atmospheric transport can be neglected, the source function of the continuity equation is zero. This leaves the O_2^A density to be represented simply as the ratio between its total photochemical productions and losses (Equation 3.5).

There are four mechanisms that contribute to the production of excited O_2^A above 40 km: photon absorption in the A-band, photon absorption in the B-band and subsequent quenching, collisional excitation by O(^{1}D), and the two-step Barth process (Section 3.3). The total production rate of O_2^A is the sum of the production rates from each of these four processes. There are only two mechanisms by which O_2^A is lost: spontaneous emission in

the A-band, and collisional quenching with other atmospheric constituents (Section 3.4). The complete photochemical model which describes all processes is summarized in Section 3.5 and an example of O_2^A density profiles depending on each contributing process is shown in Figure 3.6. All chemical reactions and their respective reaction rates are listed in Table 3.3.

The total density profile shown in Figure 3.6 represents a spectrally averaged number density across the A-band. The rate of photon emission in the A-band from the excited O_2^A molecule is directly proportional to the density and called the volume emission rate (VER). Because the density profile of O_2^A is spectrally averaged, the VER profile derived from it above will also be a single value across the A-band. The purpose of this work is to study the more detailed information contained in the spectrally resolved rotational lines of the vibrational A-band transition and their relationship with temperature (Figure 2.11). While no spectroscopy theory is employed in the propagation of the photochemical model, its result is used to determine the line position and intensity information of the A-band and eventually obtain a spectral VER (Chapter 4). This spectral information may then be used in radiative transfer theory to provide a photochemical emission source term, which can be integrated into the original SASKTRAN framework to produce the SASKTRAN +A-band emission model for accurate modelling of A-band emissions in the MLT (Chapter 5).

Chapter 4

The O_2 A-Band Emission Model

Photon emission in the A-band from the appropriately excited O_2 molecule can be modelled using standard spectroscopic and radiative transfer theory. This feature occurs as a result of an energy transition of O_2 from the excited A-band level down to ground level through the process of spontaneous emission. A-band emissions represent a change in electronic and vibrational energy state of the O_2 molecule, but a finer structure appears in the A-band spectrum due to quantum transition rules of rotational energies. Absorption cross-sections of O_2 in the A and B-bands are required to derive reaction rates of photochemical reactions outlined in Chapter 3 and are calculated from rotational line strengths and atmospheric broadening. Attenuated solar flux is also needed for photolysis reaction rates and is derived using basic radiative transfer theory and the Beer-Lambert Law. Determination of these reaction rates allows accurate calculation of the density profile of O_2^A, as is presented in at the end of Chapter 3.

The probability of spontaneous photon emission occurring at each of the rotational transition frequencies is also dependent on the temperature dependent line strength spectra and atmospheric broadening. The spectrally dependent Einstein coefficient for spontaneous emission is derived in terms of the spectroscopic line strengths and a volume emission rate (VER) is produced. The spectral VER is normalized to produce an emission weighting function which can be applied to each point of the total density profile of O_2^A yielded by the photochemical model. Finally, a photochemical emission source function is produced for use as a source term in the radiative transfer model. This result represents the observable radiative signature of complex photochemistry occurring in the MLT and as such provides valuable insight to the dynamics of the upper atmosphere.

The O_2 A-band emission model handles all spectroscopic and radiative transfer theory required for determination of the desired emission source function. Sections 4.1 and 4.2 describe the spectroscopic theory and data required to derive all other parameters. Section 4.3 explains derivation of the reaction rates required for Chapter 3 photochemical reactions. Spectral emission theory is discussed in Sections 4.4 and 4.5, after which point the density profile result from Chapter 3 is required. Finally, the spectral VER may be calculated as a function of altitude and wavenumber, and used to produce the photochemical emission source function for O_2 emitting in the A-band above 40 km. The work detailed in this chapter is essential for incorporating the A-band O_2 photochemical model into the original SASKTRAN radiative transfer model, as is the full purpose of this thesis. The combination of the photochemical model in Chapter 3 and the emission model described in this chapter creates the complete O_2 A-band photochemical emission model.

4.1 Spectroscopic Line Strengths

Section 3.1 describes the first three electronic states of the O_2 molecule (Table 3.1), and states that energy transitions between the ground electronic state $O_2(X^3\Sigma_g^-)$ and second excited electronic state $O_2(b^1\Sigma_g^+)$ are referred to as the atmospheric band. It also explains there are three vibrational states within the atmospheric band that correspond to the A, B, and γ-bands of O_2 energy transitions. The A-band represents no vibrational state change within the electronic transition ($v' = 0$ to $v'' = 0$), the B-band represents a change from $v' = 0$ to $v'' = 1$, and the γ-band from $v' = 0$ to $v'' = 2$. Energy transitions occur due to absorption or emission of a photon, and therefore are associated with electromagnetic wavelengths or wavenumbers (Table 3.2).

Rotational state transitions require even smaller energies than vibrational transitions. Therefore, the vibrational transitions described by the A, B, and γ-bands each have their own finer array of rotational transitions within. The effect of rotational transitions is to split up the pure vibrational transition lines (Petty, 2006). If the variable ΔJ represents the change in rotational quantum states with a change in vibrational states, we can say that a pure vibrational transition occurs when $\Delta J = 0$, and absorption/emission will occur

at a central wavenumber ν_0. The small band surrounding this frequency is referred to as the Q branch and is typically a forbidden transition in most systems due to conservation of energy. For cases of $\Delta J = +1$, there is an increase in rotational state with the vibrational state, which requires higher energies and therefore corresponds to higher wavenumbers. This is known as the R branch. Finally, in cases where $\Delta J = -1$, there is a decrease in rotational quantum number, which requires lower energies for the transitions and thus lower wavenumbers. This is named the P branch (Petty, 2006) (Figure 4.1).

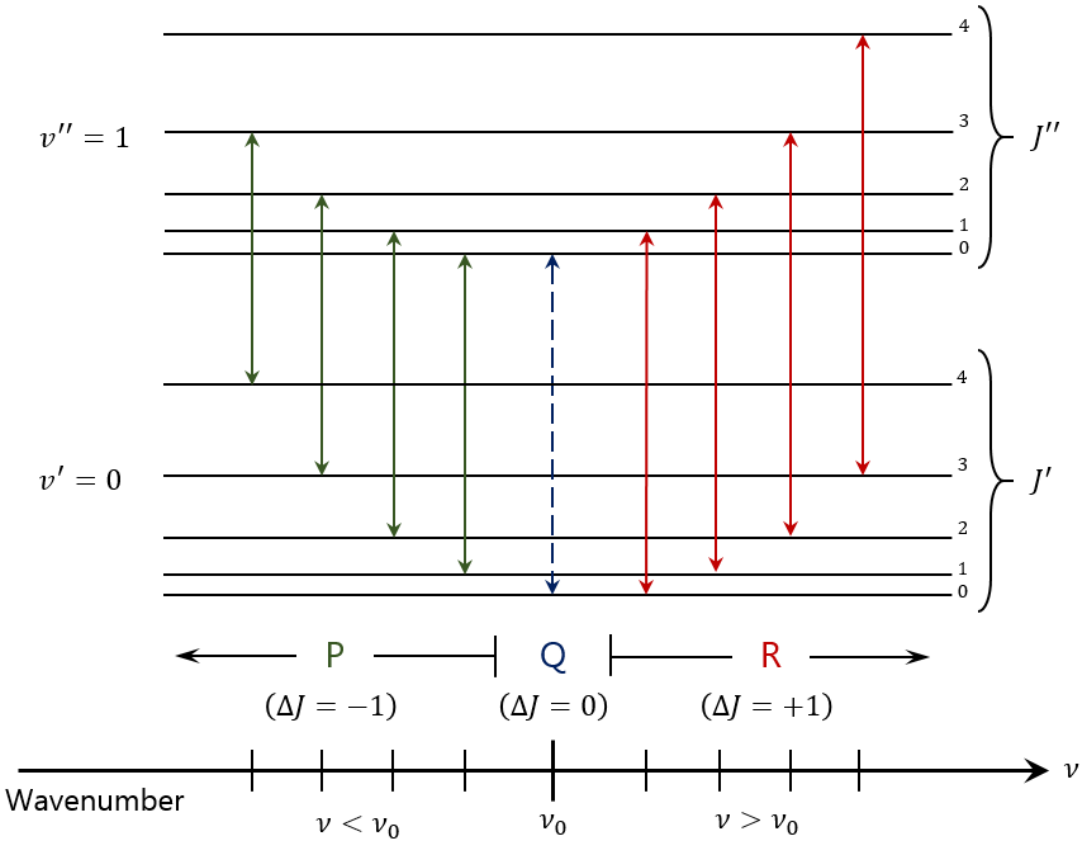

Figure 4.1: P, Q, and R branches of rotational transitions within vibrational transitions.

The rotational-vibrational spectrum of the oxygen molecule has only P and R branches, because its linear arrangement forbids transitions with $\Delta J = 0$. Therefore, the signature spectra of the A, B, and γ-bands each have two lobes with a gap in the middle. Each rotational transition is associated with a specific wavelength or wavenumber, dependent

on quantum transition rules. Each rotational transition also has an intensity, or strength. As a result, for each the A, B, and γ-bands, there is a spectrum of line strengths at allowed line positions, or transition wavenumbers. Due to its insignificance in comparison with the A and B-band absorptions, the γ-band will no longer be included in this discussion (Bucholtz et al., 1986).

In spectroscopy theory, energies are typically discussed in terms of wavenumber. The line positions are defined by transition wavenumbers, ν_j (cm^{-1}), and rely on quantum transition rules. The line strengths, $S_j(T)$, have units of cm^{-1}/molecule/cm^{-2}, and are temperature dependent. The subscript j indicates there are discrete, un-evenly spaced transition wavenumbers through which calculations must be enumerated. Each index of j represents a transition from one lower state to the next higher state. The two-lobed spectra unique to the A and B-bands can be determined theoretically through first principles, or empirically through measurements.

The HITRAN (HIgh-resolution TRANsmission) database is a line-by-line compilation of spectroscopic parameters measured at a standard temperature T_s and stored in a widely recognized and well-documented standard format (Rothman et al., 1998). More details on the HITRAN database as it pertains to the required data for the A-band model are provided in Chapter 5. The line strengths for the many different molecules that are stored in HITRAN correspond to the formula given by Rothman et al. (1998) as

$$S_j(T_s) = \frac{h\nu_j}{c}\frac{n_0(T_s)}{n_{\text{tot}}}\left(1 - \exp\left(-\frac{hc\nu_j}{kT_s}\right)\right)B_{01} \ . \tag{4.1}$$

The constants h, c, and k are the Planck constant (6.6256 x 10^{-27} cm^2 kg), the speed of light (2.9979 x 10^{10} cm/s), and the Boltzmann constant (1.3806 x 10^{-16} cm^2 kg/s^2/K) respectively. The ratio n_0/n_{tot} describes the number density of molecules in the lower state, n_0, which is temperature dependent, divided by the total number density of all molecules, n_{tot}. The final variable, B_{01}, is the Einstein coefficient for absorption, which is species dependent but invariant in temperature.

Because measurements for $S_j(T_s)$ are taken at the standard temperature, the right-hand side of Equation 4.1 does not need to be known directly. However, it is desirable to obtain values for S_j that depend on any temperature, rather than just standard temperature, T_s. A temperature dependent line strength equation can be derived by starting with a ratio with Equation 4.1.

$$\frac{S_j(T)}{S_j(T_s)} = \frac{n_{0,j}(T)}{n_{0,j}(T_s)} \frac{\left(1 - \exp\left(-hc\nu_j/kT\right)\right)}{\left(1 - \exp\left(-hc\nu_j/kT_s\right)\right)} \tag{4.2}$$

The lower state number density at the j-th transition, $n_{0,j}$, can be defined in the existence of LTE with Boltzmann statistics as

$$n_{0,j}(T) = n_{\text{tot}} \left(\frac{g_{0,j}}{Q(T)}\right) \exp\left(-\frac{hcE_{0,j}^{\nu}}{kT}\right) \tag{4.3}$$

where g_0 is the degeneracy of the lower state, $Q(T)$ is the state population partition function, and E_0^{ν} is the energy value of the lower state in wavenumber units (cm^{-1}). Substituting Equation 4.3 into Equation 4.2 gives

$$\frac{S_j(T)}{S_j(T_s)} = \frac{Q(T_s) \exp\left(hcE_{0,j}^{\nu}/kT_s\right)}{Q(T) \exp\left(hcE_{0,j}^{\nu}/kT\right)} \frac{\left(1 - \exp\left(-hc\nu_j/kT\right)\right)}{\left(1 - \exp\left(-hc\nu_j/kT_s\right)\right)} \ . \tag{4.4}$$

Rearranging the exponential terms containing the lower state energy levels yields

$$S_j(T) = S_j(T_s) \frac{Q(T_s)}{Q(T)} \exp\left(\frac{hcE_{0,j}^{\nu}}{k}\left(\frac{T - T_s}{TT_s}\right)\right) \frac{\left(1 - \exp\left(-hc\nu_j/kT\right)\right)}{\left(1 - \exp\left(-hc\nu_j/kT_s\right)\right)} \ . \tag{4.5}$$

Recall that the subscript j is used to index the state transition from lower to higher energy, and appears as a subscript on any variable that depends on transition wavenumber which must be enumerated through each allowed transition.

Atmospheric temperatures range in the region of interest range from 100 to 400 K (Brasseur and Solomon, 2005). Within these ranges, and for the wavenumber values associated with the A and B-band transitions, the exponential term at the end of Equation

4.5 becomes negligible. Therefore, the temperature dependent line strength equation reduces to

$$S_j(T) = S_j(T_s)\frac{Q(T_s)}{Q(T)}\exp\left(\frac{hcE_{0j}^{v}}{k}\left(\frac{T-T_s}{TT_s}\right)\right) . \tag{4.6}$$

McClatchey et al. (1973) also presents a temperature-dependent line strength formula of the same form as Equation 4.6, where the partition function $Q(T)$ is said to be the product of both the vibrational and rotational specific partition functions,

$$Q(T) = Q_v(T)Q_r(T) . \tag{4.7}$$

In the temperature range of interest, the vibrational partition function remains approximately constant (McClatchey et al., 1973), allowing the ratio between variable temperature and standard temperature to reduce to unity,

$$\frac{Q_v(T_s)}{Q_v(T)} \cong 1.00 . \tag{4.8}$$

The rotational partition function has a directly linear temperature dependence (McClatchey et al., 1973),

$$\frac{Q_r(T_s)}{Q_r(T)} = \frac{T_s}{T} . \tag{4.9}$$

Therefore, the temperature dependent line strength formula used in reference to the HITRAN database standard temperature measurements has the final form (McClatchey et al., 1973; Rothman et al., 1996; Bucholtz et al., 1986),

$$S_j(T) = S_j(T_s)\frac{T_s}{T}\exp\left(\frac{hc}{k}E_{0j}^{v}\left(\frac{T-T_s}{TT_s}\right)\right) , \tag{4.10}$$

where the lower state energy of each transition, E_{0j}^{v}, is also available from the HITRAN database.

Figure 4.2 shows the rotational spectra of the A and B-bands respectively. Notice the two distinct lobes representing the P and R branches, with a gap in the middle signifying

the lack of Q branch transitions. Note also the temperature dependence of the line strengths, in that the spectral shape widens out with increasing temperatures. A magnification of one of the transition lines shows that the line strength has no width and is merely a discrete value determined by quantum rules.

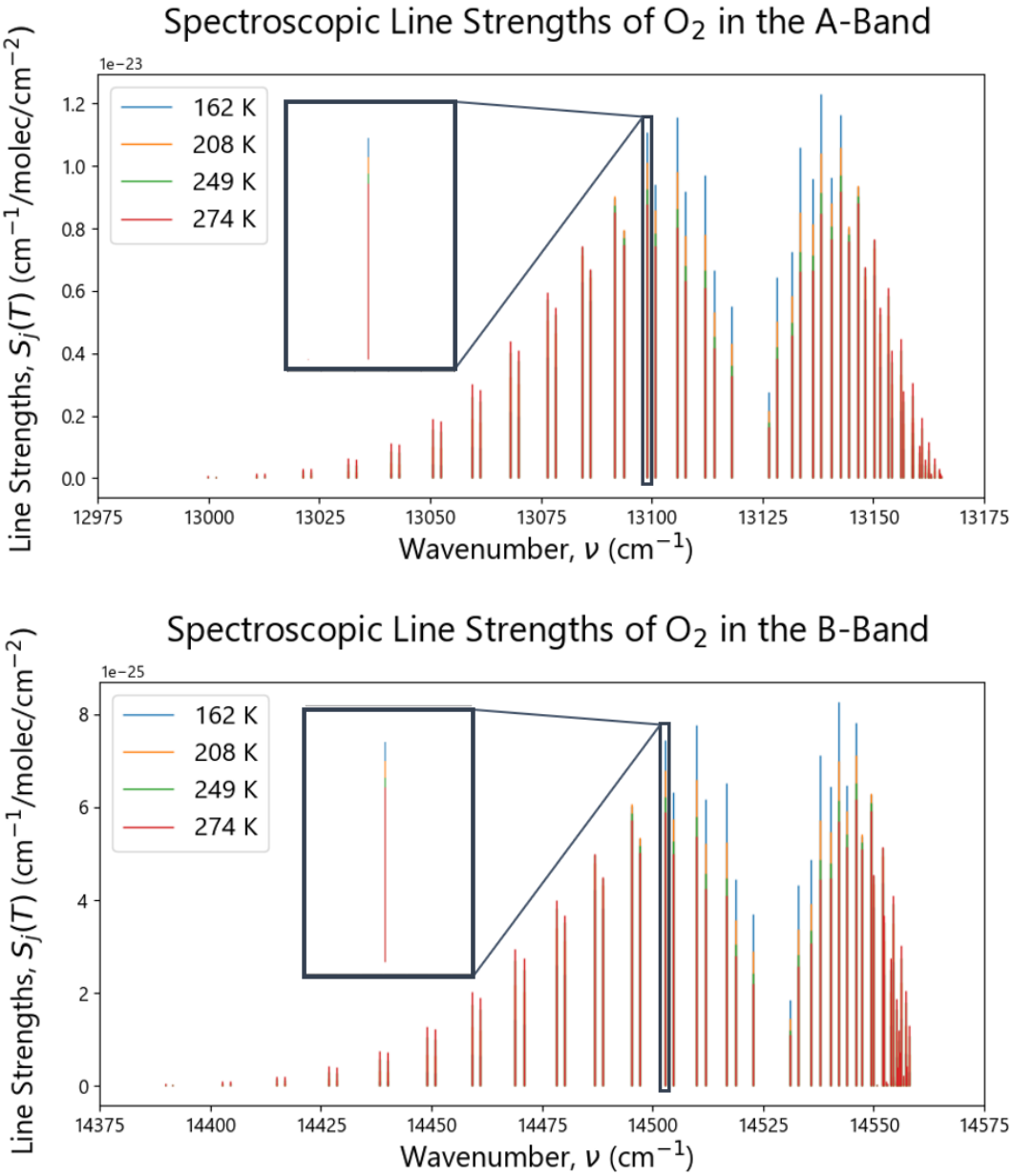

Figure 4.2: Temperature dependent rotational spectra from O_2 in the A and B-bands, calculated from HITRAN measurements at a standard temperature. A magnification of one transition line shows no width in the line strength.

4.2 Atmospheric Line Broadening

In theory, energy transitions in the rotational spectra of the A and B-bands (Figure 4.2) can only occur at the precise transition wavenumber allowed by quantum rules. However, in the atmosphere, broadening of these lines may occur via three processes (Petty, 2006):

1) Natural broadening is due to the uncertainty principle. Its effect is so small that it is considered negligible for this work.
2) Pressure broadening occurs when collisions between molecules impart energy to disrupt natural transitions between states. Photonic emission of oxygen in the A-band does not become significant in the atmosphere until 40 km altitude, at which point the pressure is low enough for this process to also be negligible (Petty, 2006; Bucholtz et al., 1986).
3) Doppler broadening has to do with random translational movements of molecules in a gas. Their relative velocities Doppler-shift the wavenumbers at which energy transitions can occur. In the lower pressure environment of the MLT above 40 km, this is the dominant broadening effect, and the only one considered for this photochemical model (Petty, 2006; Bucholtz et al., 1986).

The Doppler line shape is a Gaussian distribution that depends on any given wavenumber of interest, ν, and the transition wavenumber, ν_j, both in units of cm^{-1} (Petty, 2006):

$$D(\nu) = \frac{1}{\alpha\sqrt{\pi}} \exp\left[-\left(\frac{\nu - \nu_j}{\alpha}\right)^2\right] . \tag{4.11}$$

The parameter α denotes the line half-width at half maximum of the profile, has wavenumber dimensions cm^{-1}, and depends on temperature in the following relationship:

$$\alpha(T) = \frac{\nu_j}{c}\left(\frac{2kT}{m}\right)^{1/2} \tag{4.12}$$

where c is the speed of light (2.9979 x 10^{10} cm/s), k is the Boltzmann constant (1.3806 x 10^{-16} cm^2 $kg/s^2/K$), and m is the mass of the O_2 molecule (5.314 x 10^{-23} g/molecule). The

line shape in Equation 4.11 therefore has units of $1/\text{cm}^{-1}$ from its inverse dependence on α, and can be normalized such that:

$$\int_{-\infty}^{\infty} D(\nu)\, d\nu = 1 \tag{4.13}$$

Lastly, because the Doppler line shape depends on transition wavenumber, ν_j, it can be enumerated to match the previous discussion regarding line strength using the line position index j. Therefore, there are j number of line shapes, each dependent on the respective transition wavenumber:

$$D_j(\nu, T) = \frac{1}{\alpha_j(T)\sqrt{\pi}} \exp\left[-\left(\frac{\nu - \nu_j}{\alpha_j(T)}\right)^2\right]; \quad \alpha_j(T) = \frac{\nu_j}{c}\left(\frac{2kT}{m}\right)^{1/2} \tag{4.14}$$

Note carefully the difference between discrete indexed transition wavenumber ν_j and the effectively continuous array of any given wavenumber, ν. It can be seen from Equation 4.14 that Doppler broadening of a transition line is both wavenumber and temperature dependent, which is further illustrated in Figure 4.3.

4.3 Photochemical Reaction Rates and Photolysis Coefficients

All the chemical reactions involved in the photochemical model outlined in Chapter 3 have an associated reaction rate coefficient (listed in Table 3.3). All reaction rates are spectrally independent, while some also have a relation to altitude. The altitude relation is typically exhibited in terms of a simple temperature dependence, but both photon absorption processes and the photolysis reactions depend on the amount of solar flux propagated through the atmosphere. Therefore, they must be calculated in terms of attenuated solar flux and absorption cross-section.

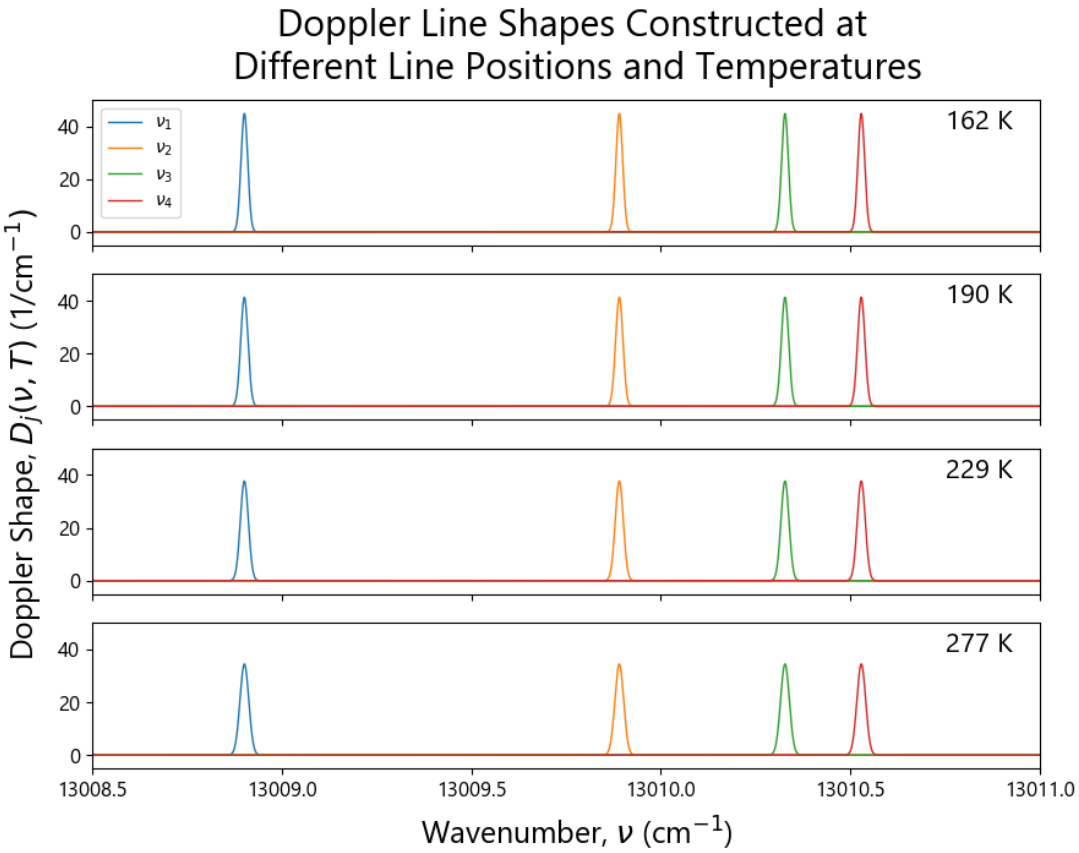

Figure 4.3: One Doppler line shape is made centred on each transition wavenumber (of which four are pictured above). As temperature increases, the width of the Gaussian increases, necessitating a decrease in height to satisfy the normalization.

4.3.1 Absorption Cross-Sections

The absorption cross-section, $\sigma(\nu, T)$ (cm^2/molec), of the oxygen molecule at any given temperature, T, is obtained by applying the Doppler line shape in Equation 4.14 to the line strengths in Equation 4.10, and summing over each transition wavenumber, ν_j,

$$\sigma(\nu, T) = \sum_j S_j(T) D_j(\nu, T) \ , \tag{4.15}$$

where the independent variable ν is an effectively continuous array of wavenumbers, and the independent variable T represents the temperature profile fed into the model as part of the atmospheric state (see Chapter 5 for further explanation of atmospheric state, and refer to Chapter 6 section for choice of atmospheric state data). Because the temperature

is provided as a profile, it is directly related to altitude, and therefore the absorption cross-section in Equation 4.15 has an implicit altitude dependence.

The absorption cross-section must be calculated over both the A and B-bands for the oxygen molecule. Figure 4.4 illustrates the structure of the absorption spectra of both bandwidths, and at various temperatures. Notice that this is a similar shape to the line strengths spectra displayed in Figure 4.2, but with each line having the smooth Gaussian shape of the Doppler line shape (Figure 4.3) rather than a single vertical line with no width.

4.3.2 Attenuated Solar Flux

The Beer-Lambert Law can be used to describe the attenuation of electromagnetic radiation through the atmosphere. The derivation given by Petty (2006) yields a general form of attenuated spectral radiance between two points, s_1 and s_2:

$$I_\lambda(s_2) = I_\lambda(s_1) \exp\left[-\int_{s_1}^{s_2} k(s)\, ds\right] \tag{4.16}$$

where I_λ (W/m^2/ster/nm) represents monochromatic radiance at wavelength λ (nm), and k (m^{-1}) is the extinction coefficient of the medium as a function of distance. The integral term represents the optical path between two points, referred to as optical depth in the case of vertical paths:

$$\tau(s_1, s_2) \equiv \int_{s_1}^{s_2} k(s)\, ds \tag{4.17}$$

Optical depth is a dimensionless non-negative number and is zero when $s_1 = s_2$ or when $k(s) = 0$ between the two points.

Because of the dimensionless nature of the optical depth, the radiance in Equation 4.16 can instead be expressed in terms of non-directional spectral photon flux, F_λ (photons/s/cm^2/nm). The two points s_1 and s_2 are chosen as altitudes, where $s_1 = z$ is any point within the atmosphere and s_2 is chosen to be the top of the atmosphere, z_∞.

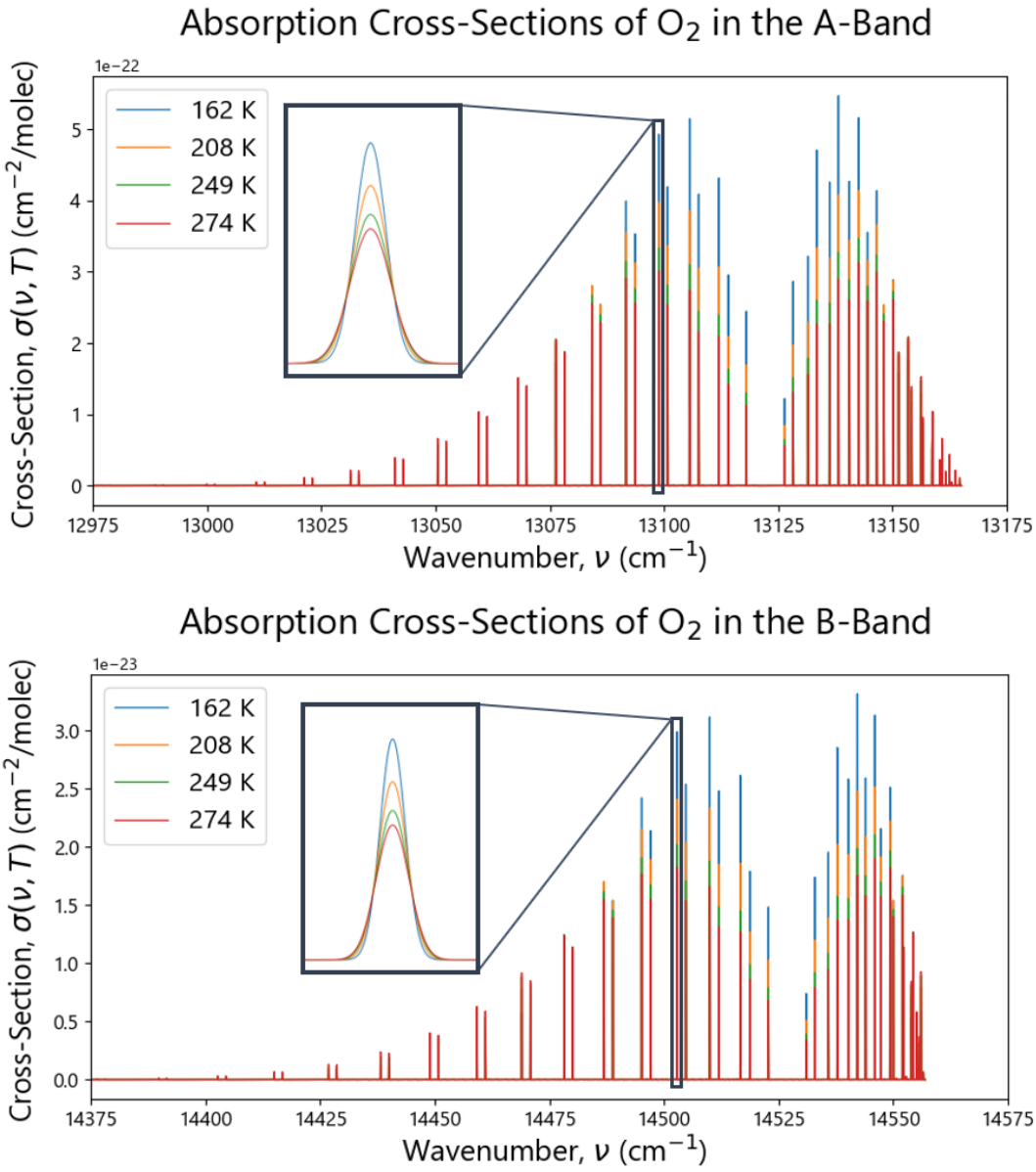

Figure 4.4: Absorption cross-sections of O_2 in both the A and B-bands at different temperatures. Each transition line is represented by a narrow Gaussian provided by the Doppler line shape.

The combination of Equation 4.16 and 4.17 then yields the more compact version used for this model to determine the atmospheric attenuation of solar flux as a function of wavelength

$$F(\lambda, z) = F(\lambda, z_\infty) \exp[-\tau(\lambda, z)] \tag{4.18}$$

where $F(\lambda, z)$ is the attenuated solar flux at altitude z, $F(\lambda, z_\infty)$ is the incident solar flux at the top of the atmosphere, and $\tau(\lambda, z)$ is the optical depth from any altitude z to the top of the atmosphere z_∞.

According to Brasseur and Solomon (2005), the optical depth of the atmosphere can be modelled as being only due to absorption by atmospheric species

$$\tau_{\text{atm}}(\lambda, z, \chi) = \sec\chi \int_z^{z_\infty} \sum_x [x]\sigma_x(\lambda, z)\, dz' \ , \tag{4.19}$$

where χ is the solar zenith angle, x is the molecular species of interest, $[x]$ (cm^{-3}) is the number density of species x, and $\sigma_x(\lambda, z)$ (cm^2/molec) is the absorption cross-section of species x from Equation 4.15 with altitude dependence. The optical depth of the atmosphere is directly proportional to the sum of all the absorber molecule densities weighted by their absorption cross-sections integrated along a vertical path from any point in the atmosphere to the top. Combining Equations 4.18 and 4.19 yields the complete attenuated solar flux dependent on the incident solar flux, solar zenith angle, and absorber density and cross-section:

$$F(\lambda, z) = F(\lambda, z_\infty) \exp\left(-\sec\chi \int_z^{z_\infty} \sum_x [x]\sigma_x(\lambda, z)\, dz' \right) \tag{4.20}$$

Further discussion on the source of incident solar flux data and absorption cross-sections in the spectral regions of interest is available in Section 5.4.

4.3.3 Reaction Rates and Coefficients

The reaction rate coefficients for photon absorption in the A and B-bands (Equations 3.7 and 3.9) are denoted g_{A} and g_{B} respectively and are referred to as g-factors. The g-factors (s^{-1}) are dependent on attenuated solar flux (Equation 4.20) and absorption cross-section (Equation 4.15) (Sheese, 2009):

$$g_{\mathrm{A,B}}(z) = \int_{\nu} F(\nu, z)\sigma(\nu, z)\, d\nu' \tag{4.21}$$

Because the g-factors are integrated over the spectrum of interest, it is of no consequence whether the integrands are in terms of wavenumber or wavelength, provided they are consistent with one another. Further discussion on evaluating the g-factors is given in Section 5.4.

The rate coefficients for photolysis in the Lyman-α line, SRC, and Hartley bands (Equations 3.19, 3.20, and 3.21) are denoted J_{L}, J_{S}, and J_{H} respectively. The photolysis coefficients depend on attenuated solar flux and absorption cross-section, similar to the g-factors above. However, these coefficients also require unitless quantum yields, ϕ, for photodissociation of each molecule in its respective bandwidth (Sheese, 2009). Values acquired for quantum yields are described in Section 5.3.3.

$$J_{\mathrm{L,S,H}}(z) = \int_{\lambda} F(\lambda, z)\, \sigma(\lambda)\, \phi\ \ d\lambda' \tag{4.22}$$

4.4 Einstein Spontaneous Emission Coefficient

There are three Einstein coefficients that correspond to the ways in which atoms can experience energy transitions from a lower energy state to a higher state, E_0 to E_1 (Bernath, 2005):

1) B_{01} ($\mathrm{cm^3/J/s}$) represents the absorption of a photon of wavenumber $\nu_{01} = \nu_j$ from the background radiation density.
2) B_{10} ($\mathrm{cm^3/J/s}$) represents stimulated emission of a photon of wavenumber $\nu_{01} = \nu_j$. Background radiation density is required for stimulation.
3) A_{10} ($\mathrm{s^{-1}}$) represents spontaneous emission of a photon of wavenumber $\nu_{01} = \nu_j$. Background radiation density is not required for spontaneous emission; it can occur in a vacuum.

The process of interest for the study of photon emission from oxygen in the A-band is spontaneous emission with Einstein coefficient A_{10}. Using Boltzmann statistics, the Einstein coefficient for spontaneous emission can be described in terms of the absorption coefficient, B_{01} (Bernath, 2005):

$$A_{10,j} = 8\pi h\nu_j^3 \left(\frac{g_0}{g_1}\right) B_{01} \tag{4.23}$$

where h is the Planck constant, ν_j is the transition wavenumber, and g_0 and g_1 are the degeneracies of each energy level. Note the explicit dependence of A_{10} on the line position ν_j, which requires that A_{10} itself is enumerated through the index j, denoting it $A_{10,j}$.

Following the derivation outlined in Section 4.1, the temperature dependent line strengths in Equation 4.1 can be combined with Equation 4.3 to have the following form:

$$S_j(T) = \frac{h\nu_j}{c}\frac{g_0}{Q(T)}\exp\left(-\frac{hcE_{0j}^{\nu}}{kT}\right)B_{01} \ . \tag{4.24}$$

This can further be rearranged to determine the absorption coefficient B_{01} in terms of line strengths and line position, requiring it also become indexed by j:

$$B_{01,j} = S_j(T)\frac{c}{h\nu_j}\frac{Q(T)}{g_0}\exp\left(\frac{hcE_{0j}^{\nu}}{kT}\right) . \tag{4.25}$$

The spontaneous emission coefficient is then also dependent on line strengths and has the form:

$$A_{10,j} = 8\pi c\nu_j^2 \, S_j(T)\frac{Q(T)}{g_1}\exp\left(\frac{hcE_{0j}^{\nu}}{kT}\right) . \tag{4.26}$$

Note that although the Einstein coefficients in Equations 4.25 and 4.26 seem temperature dependent, they are not. If the temperature relative line strength equation in Equation 4.10 is substituted into either equation, the temperature dependent components cancel, and the Einstein coefficients are only left dependent on the constant standard temperature, $T_s = 296$ K. This substitution is not performed since the temperature relative line strengths in Equation 4.10 are already calculated for determination of the absorption cross-section.

Therefore, it is easier algorithmically to use them in determination of the spontaneous emission coefficient as well.

4.5 Spectral Emission Weighting Function

The volume emission rate (VER), η, of any species can be determined from the number density of the species in the excited state, n_1, and the Einstein coefficient, $A_{10,j}$:

$$\eta_j(T) = n_1(T) A_{10,j} \tag{4.27}$$

While $n_1(T)$ is the temperature dependent number density of molecules per unit volume, it can also be expressed in units of photons/cm^3, because the number of excited molecules is equivalent to the number of potential photons emitted. The spontaneous emission Einstein coefficient $A_{10,j}$ has units of s^{-1}, providing the VER with units of photons/cm^3/s. The excited state number density, $n_1(T)$, can be described by the Boltzmann distribution in Equation 4.3,

$$\eta_j(T) = \mathcal{C}\, \nu_j^2\, S_j(T) \exp\left(\frac{hc}{kT}\left(E_{0j}^{\nu} - E_{1j}^{\nu}\right)\right), \tag{4.28}$$

where $\mathcal{C}$ is a constant coefficient that is the product of 8π, c (the speed of light), and n_{tot} (total number density of molecules in the system). The extra energy variable E_{1j}^{ν} is the higher energy level of the system of the j-th transition between lower (0) and higher (1) states. Note that because both the energy values E_{0j}^{ν} and E_{1j}^{ν} are given in wavenumber units, the difference between them is equal to the transition wavenumber, ν_j, yielding

$$\eta_j(T) = \mathcal{C}\, \nu_j^2\, S_j(T) \exp\left(\frac{-hc\nu_j}{kT}\right). \tag{4.29}$$

Similar to the process used to obtain absorption cross-section (Equation 4.15), the discretely indexed VER values $\eta_j(T)$ must be Doppler broadened to more accurately represent the transitions occurring in the atmosphere (Petty, 2006). Applying the Doppler line shape from Equation 4.14 to the discrete VER in Equation 4.28 and summing over

transition index j yields the theoretical spectral VER of O_2, η'_{spec}. This result is dependent on any given temperature and wavenumber,

$$\eta'_{\text{spec}}(\nu, T) = \sum_j \eta_j(T) D_j(\nu, T) \ . \tag{4.30}$$

Note the prime notation in Equation 4.30 is used to designate this as the theoretical spectral VER, derived from spectroscopic first principles and using HITRAN data. The unprimed spectral VER, η_{spec} (Equation 4.33), is the final result of the A-band emission model and is calculated from the combination of the spectroscopy derived $\eta'_{\text{spec}}(\nu, T)$ and the spectrally averaged VER profile, $\eta_{\text{pro}}(z)$ (Equation 4.32), obtained from the original atmospheric state through the O_2^A density photochemical model (Chapter 3). Section 4.6 contains further details on the calculation of the final spectral VER, η_{spec}.

Equation 4.30 gives absolute VER in units of photons/cm^3/s/cm^{-1}. In order to acquire an emission spectrum that only contains wavenumber dependence, the theoretical spectral VER must be normalized (Equation 4.13). The normalization produces a spectral emission weighting function with units of 1/cm^{-1},

$$W_{\text{emi}}(\nu, T) = \frac{\eta'_{\text{spec}}(\nu, T)}{\int \eta'_{\text{spec}}(\nu, T)\, d\nu'} \ . \tag{4.31}$$

Because of the eventual normalization of the theoretical spectral VER, η'_{spec}, the coefficient $\mathcal{C}$ in the definition of Equation 4.29 may be neglected from the derivation. As mentioned in Section 4.3.1 with regards to the absorption cross-section, the weighting function dependence on temperature provides an indirect dependence on altitude. At this stage in the model derivation, altitude dependence is made explicit and the weighting function demonstrated in Figure 4.5 is shown for four different altitudes instead of temperatures.

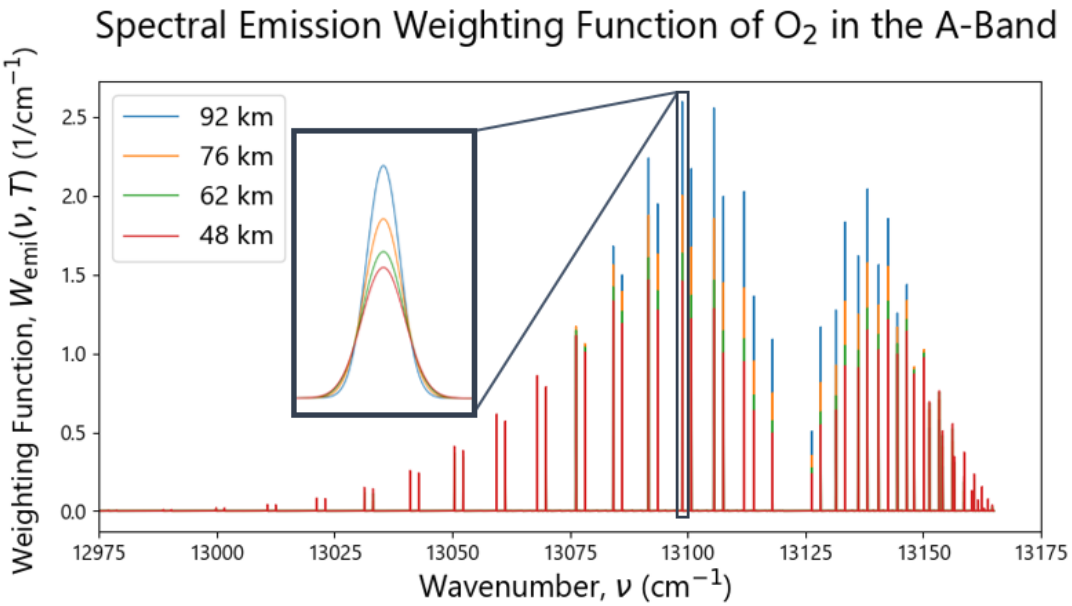

Figure 4.5: The spectral emission weighting function from normalized theoretical spectral VER in the A-band, shown at four different altitudes, corresponding to atmospheric temperatures. Each transition line is represented by a narrow Gaussian as in Figure 4.4, due to the application of the Doppler line shape for atmospheric broadening (Equation 4.30).

4.6 Spectral Volume Emission Rate in the A-Band

The photochemical model outlined in Chapter 3 provides results in the form of density profiles of the excited O_2^A molecule (Equation 3.53, Figure 3.6). This profile is technically represented by the variable $n_1(T)$ in Equation 4.27, which is the number density of molecules in an excited state. Using a spectrally averaged single value for the Einstein spontaneous emission coefficient for the A-band, $A_{1\Sigma}$, and the Franck-Condon factor F_C, the VER profile has units of photons/s/cm^3 and is described by Bucholtz et al. (1986) as

$$\eta_{pro}(z) = F_C A_{1\Sigma}[O_2^A] \ , \tag{4.32}$$

The Franck-Condon factor F_C for the A-band has the value of 0.93 (Nicholls, 1965) and the Einstein coefficient $A_{1\Sigma}$ is 0.085 s^{-1} (Burch and Gryvnak, 1969). Figure 4.6 shows the VER profiles of O_2 in the A-band due to its four contributory processes (collisional excitation from O(^{1}D) shown as two profiles, one from O_2 photolysis and one from O_3 photolysis), as well as the total VER profile in black. Notice the shape of these profiles is

identical to that of the density profiles in Figure 3.6 with magnitude scaled by the reaction rate $F_C A_{1\Sigma}$ in Equation 4.32.

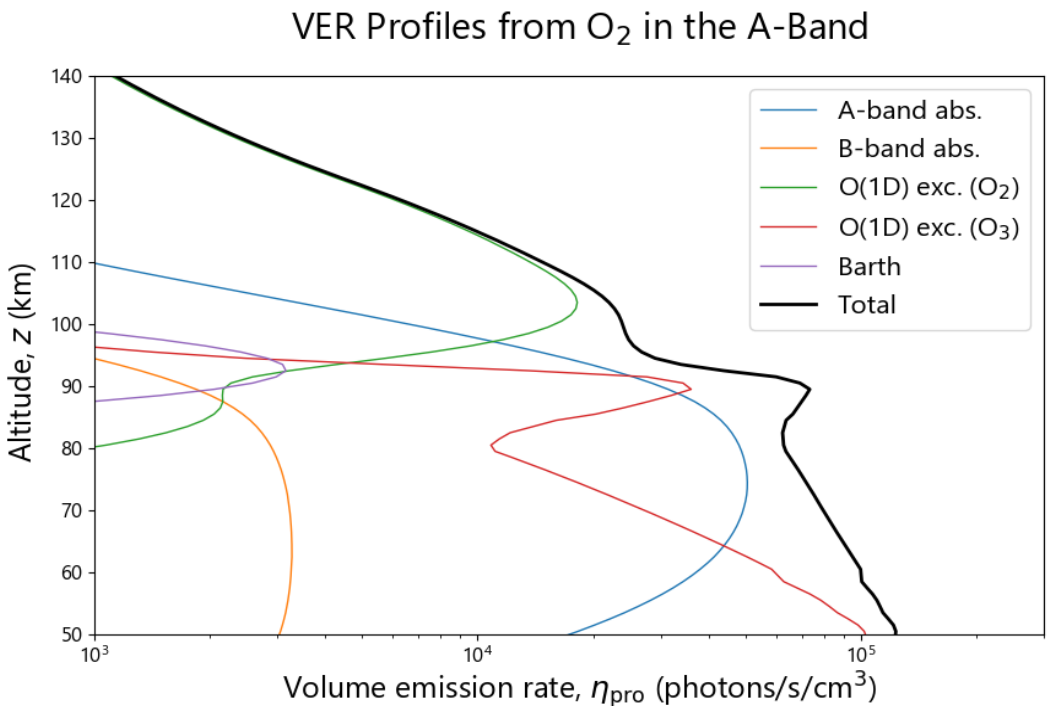

Figure 4.6: VER of O_2 in the A-band as altitude profiles. Each coloured profile represents the VER supplied by each of the four chemical processes that produce excited O_2^A (with production due to collisions with O(^{1}D) divided between its photolysis sources, O_2 and O_3). The black profile displays the sum of all processes, $\eta_{pro}(z)$ (Equation 4.32).

The VER profile in Equation 4.32, $\eta_{pro}(z)$, has no spectral dependence, and only depends on altitude from the density profile. The spectral dependence comes from the spectral emission weighting function, $W_{emi}(\nu, z)$, derived from first principles, shown in Equation 4.31 and Figure 4.5. Therefore, the final spectral VER, η_{spec}, can be determined at any altitude by applying the weighting function,

$$\eta_{spec}(\nu, z) = W_{emi}(\nu, z)\, \eta_{pro}(z) \quad . \tag{4.33}$$

Figure 4.7 shows the final spectral VER for the O_2 molecule across the A-band for various temperatures, corresponding to altitudes. Again, notice the shape is similar to that

demonstrated by the absorption cross-sections (Figure 4.4) and the spectral emission weighting function (Figure 4.5), with each line defined as a narrow Gaussian from the Doppler line shapes applying atmospheric broadening.

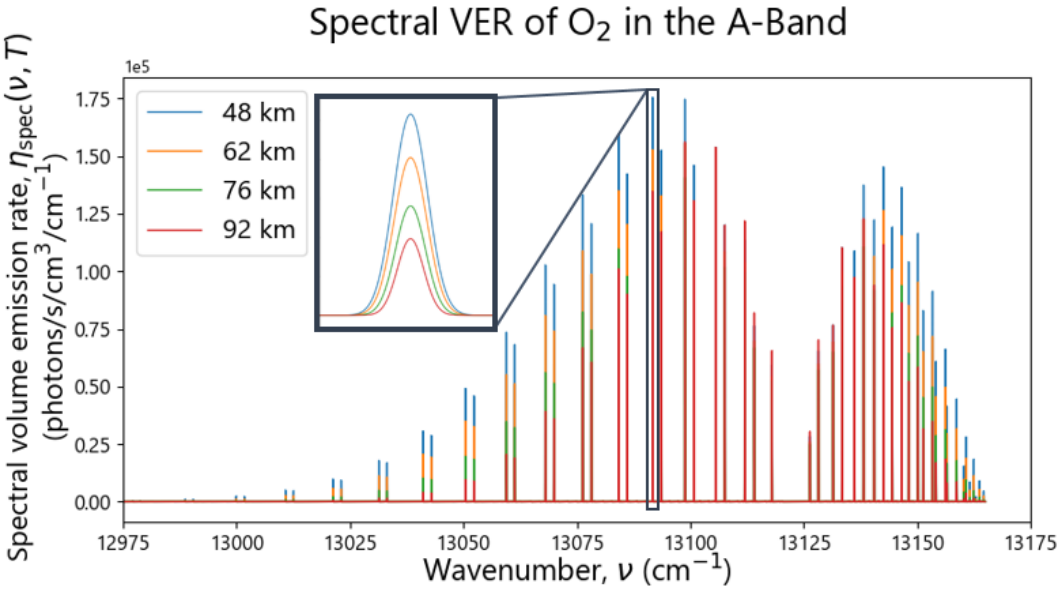

Figure 4.7: The spectral VER of O_2 in the A-band, derived from the spectral emission weighting function of spectroscopic first principles and the VER profiles from the O_2^A density photochemical model. One spectrum is shown for each of four different altitudes, corresponding to atmospheric temperatures. Each transition line still exhibits the narrow Gaussian given by applying Doppler line shape for atmospheric broadening (Equation 4.30).

4.7 Photochemical Emission Source Function

The study of light propagation through the atmosphere is governed by the radiative transfer equation. Light that is merely attenuated due to atmospheric absorption can be modeled from the Beer-Lambert law as discussed in Section 4.3.2 with Equations 4.16 and 4.17. For a more complete model of radiative transfer that includes photon emission sources to atmospheric constituents as well as absorbers, another term must be added. The integral form of this equation in an Earth-centred coordinate system is:

$$I(\vec{r}_0, \hat{\Omega}) = \int_{s_1}^{0} J(s, \hat{\Omega}) \exp(-\tau(s,0))\ ds + \tilde{I}(s_1, \hat{\Omega}) \exp(-\tau(s_1,0)) \tag{4.34}$$

where $I(\vec{r}_0, \hat{\Omega})$ is the radiance, observed from location $\vec{r}_0$ with propagation direction $\hat{\Omega}$ along the straight-line path defined by both and denoted s (more details on specific geometry and units in Section 5.2.1). The source term $J(s, \hat{\Omega})$ also depends on this path and direction, and is multiplied by the attenuation term, $\exp(-\tau(s,0))$. The product of the two is integrated along the path from the end of the path at $s = s_1$ (negative value) to the observer location at $s = 0$. The last variable, $\tilde{I}(s_1, \hat{\Omega})$, is the radiance seen at the end of the path s_1, also attenuated by the same exponential term, $\exp(-\tau(s_1,0))$. Therefore, the radiance seen by an observer along a straight path from some far point $s = s_1$ to observer location $s = 0$ is the sum of all the sources of radiation integrated along that path plus any radiance occurring at the end of the path, both attenuated by the atmosphere along the path (Bourassa et al., 2007).

The attenuation term is an exponential that depends on optical depth, τ, with extinction coefficient k,

$$\tau(s,0) \equiv \int_{s}^{0} k(s)\ ds' \ . \tag{4.35}$$

The extinction coefficient $k(s)$ consists of absorption properties of various species and is the means by which molecular absorption is included in the model.

In general, the source function $J(s, \hat{\Omega})$ depends on position s and propagation direction $\hat{\Omega}$. Position has three dimensions and the look vector adds two more dimensions in the way of angular distribution, giving the source function five dimensions in total. The source function for study of the atmosphere above 40 km must include both scattering processes and photochemical emissions.

$$J(s, \hat{\Omega}) = J_{\text{scat}}(s, \hat{\Omega}) + J_{\text{emi}}(s, \hat{\Omega}) \tag{4.36}$$

The scattering source function is calculated within the radiative transfer model and has the following form:

$$J_{\text{scat}}(s,\hat{\Omega}) = k_{\text{scat}}(s) \int_{4\pi} I(s,\hat{\Omega}')\bar{p}(s,\Theta)\, d\hat{\Omega}' \tag{4.36}$$

The coefficient $k_{\text{scat}}(s)$ is the extinction solely due to scattering processes, $\bar{p}(s,\Theta)$ is the scattering phase function, and Θ is the angle between the incoming direction $\hat{\Omega}'$ and outgoing direction $\hat{\Omega}$. The integral is performed over the unit sphere with a solid angle value of 4π (Zawada et al., 2015).

The values used in the emission source function, $J_{\text{emi}}(s,\hat{\Omega})$, come from the combined O_2 A-band photochemical emission model described in Chapters 3 and 4. A VER spectrum from O_2 across the A-band is stored at each altitude of interest (above 40 km), from the final result $\eta_{\text{spec}}(\nu,z)$ in Equation 4.33. The source function, $J_{\text{emi}}(s,\hat{\Omega})$, is an emission per solid angle, and therefore must be in units of photons/s/cm^3/cm^{-1}/ster. Because the O_2 molecule is assumed to emit in all directions equally, the spectral VER η_{spec} can be divided by the solid angle of a complete sphere to produce the wavenumber and altitude dependent two-dimensional array of photochemical emission source function values,

$$J_{\text{emi}}(\nu,z) = \frac{\eta_{\text{spec}}(\nu,z)}{4\pi}\ . \tag{4.38}$$

The radiative transfer equation in Equation 4.34 can now be used to study photochemical emissions in the mesosphere and lower thermosphere in the existence of scattering from the ground or from other atmospheric particles. A full discussion of inputs required, array resolutions, and other necessary parameters is handled in the following Chapter 5.

4.8 Chapter Summary

Spectroscopy and radiative transfer theory are required to model the photon emission from the O_2 molecule in the A-band. The O_2 A-band emission model receives inputs of temperature profiles and spectroscopic line strengths at a standard temperature for O_2 in

the A and B-bands (Section 4.1). The line strength spectra are made temperature dependent through use of Equation 4.10 (Figure 4.2) and converted into Gaussian peaks due to atmospheric Doppler broadening (Section 4.2). Together the temperature dependent line strengths and the Doppler line shape are used throughout the model for absorption cross-sections and spectral emission functions.

Reaction rates are required for all chemical reactions involved in the O_2^A density photochemical model (Chapter 3) and are listed in Table 3.3. Some reaction rates are constant, and most others depend on temperature, but still some have relationships with attenuated solar flux in the atmosphere and the absorption cross-sections of relevant atmospheric constituents. Section 4.3 describes calculation of reaction rates for photon absorption in the A and B-bands (g factors, wavenumber dependent) and for photolysis of O_2 and O_3 in the Lyman-α line, Schumann Runge continuum, and Hartley bands (J coefficients, wavelength dependent). The reaction rates calculated from Equations 4.21 and 4.22 are fed into the photochemical model described in Chapter 3, at which point the density profile of the excited O_2^A is determined (Figure 3.6).

Spectral emission equations are derived from first principles using the Einstein coefficients for absorption and spontaneous emission (Section 4.4). The spectral emission coefficient for spontaneous emission in the A-band (Equation 4.26) depends on temperature dependent line strengths and is combined with number density to provide a spectral volume emission rate (VER) for discrete wavenumbers (Equation 4.29). This is in turn Doppler broadened and normalized to yield the spectral emission weighting function presented in Section 4.5 (Equation 4.31, Figure 4.5). Spectrally averaged VER profiles are obtained from the photochemical model's O_2^A density profiles (Equation 4.32, Figure 4.6), but only consist of a single value for each altitude (Section 4.6). Each of these values must be multiplied by the spectral emission weighting function to provide spectral dependence of relative intensity of photon emission from O_2 across the A-band. The product of the VER profiles with the weighting function applied at each altitude provides spectrally resolved VER data throughout the atmosphere (Equation 4.33, Figure 4.7). Section 4.7 finally derives the photochemical emission source function from the spectral VER

(Equation 4.38), which is presented in the proper format for integration into the original SASKTRAN radiative transfer model. The emission source function is the final output produced by the O_2 A-band emission model, which makes use of the $\mathsf{O}_2^{\mathsf{A}}$ density photochemical model (Chapter 3) and feeds its result to the integrated SASKTRAN +A-band emission model. Further discussion of the software implementation of the theory presented in Chapters 3 and 4 is discussed in Chapter 5, including parameter set-up and software integration into the SASKTRAN +A-band model.

Chapter 5

Implementation of the Integrated SASKTRAN +A-Band Emission Model

Practical implementation of the photochemical, spectroscopic, and radiative transfer theory described in previous Chapters 3 and 4 is required to incorporate O_2 A-band emissions into the original SASKTRAN radiative transfer model (background on SASKTRAN provided in Section 2.3.2). The original SASKTRAN was designed to support analysis of radiance measurements made in the atmospheric limb from the OSIRIS instrument (Section 2.3.1). SASKTRAN uses the standard radiative transfer equation discussed in Chapter 4 to simulate light propagation through an atmosphere with sources and absorption. Until this point, SASKTRAN has only considered multiple scattering as contributions to the source function, $J(s, \hat{\Omega})$, along with atmospheric absorption providing attenuation along the line of sight in terms of the optical depth, τ. The complete O_2 A-band photochemical emission model is developed to provide the original SASKTRAN model with an additional source term due to photochemical emission in its radiative transfer equation. Three concentric layers of model are presented: the first is the original SASKTRAN radiative transfer model, the second is the O_2 A-band emission model derived from spectroscopic and radiative transfer theory (Chapter 4), and the third is the O_2^A density photochemical model concerning all relevant atmospheric chemistry (Chapter 3). The complete multi-layer model provides an update to the original SASKTRAN and is referred to as the integrated SASKTRAN +A-band emission model.

This chapter provides details on software implementation required to combine the three layers of model. A flow chart (Figure 5.1) is provided first as diagrammatic description of implementation and integration, with each section explained further throughout the

chapter. An overview is given for each section, with further technical information provided in Appendix A. Explanation occurs in the order in which the model is applied, giving a step-by-step approach to the software method and referring to theory outlined in previous chapters. Data sources are only discussed when inputs are designed to be static and not user-defined. Specific values or data sources chosen for model verification are stated in Chapter 6.

5.1 The SASKTRAN +A-Band Emission Model Diagram

The fully integrated SASKTRAN +A-band emission model contains three submodels. Submodel A is similar to the original SASKTRAN radiative transfer model, capable of considering atmospheric absorption and scattering properties, but updated to be capable of considering a new emission source term, J_{emi}. Submodel B is the O_2 A-band emission model, whose process and theory are described in Chapter 4. Submodel C is the $\mathsf{O}_2^{\mathsf{A}}$ density photochemical model, discussed in Chapter 3. Submodel A is the outermost shell, while both submodels B and C are contained within each other successively. Submodels B and C together were coded in Python for this work and implemented with external help into the existing SASKTRAN framework. The SASKTRAN radiative transfer model (A) must set up the geometry and atmosphere of the system, then pass the relevant parameters to the O_2 A-band emission model (B). The spectroscopic information is then calculated, and some radiative transfer theory is performed in the way of solar flux attenuation. The final submodel C, the photochemical model, is called to return the density profiles of the excited $\mathsf{O}_2^{\mathsf{A}}$ molecule, which is then used to produce the result of the emission model (B), the photochemical emission source function. This finally is directly passed into the SASKTRAN (A) radiative transfer engine to simulate radiances observed through an atmosphere with atmospheric absorption, scattering, and emission characteristics. Figure 5.1 demonstrates the algorithm in a flow-chart.

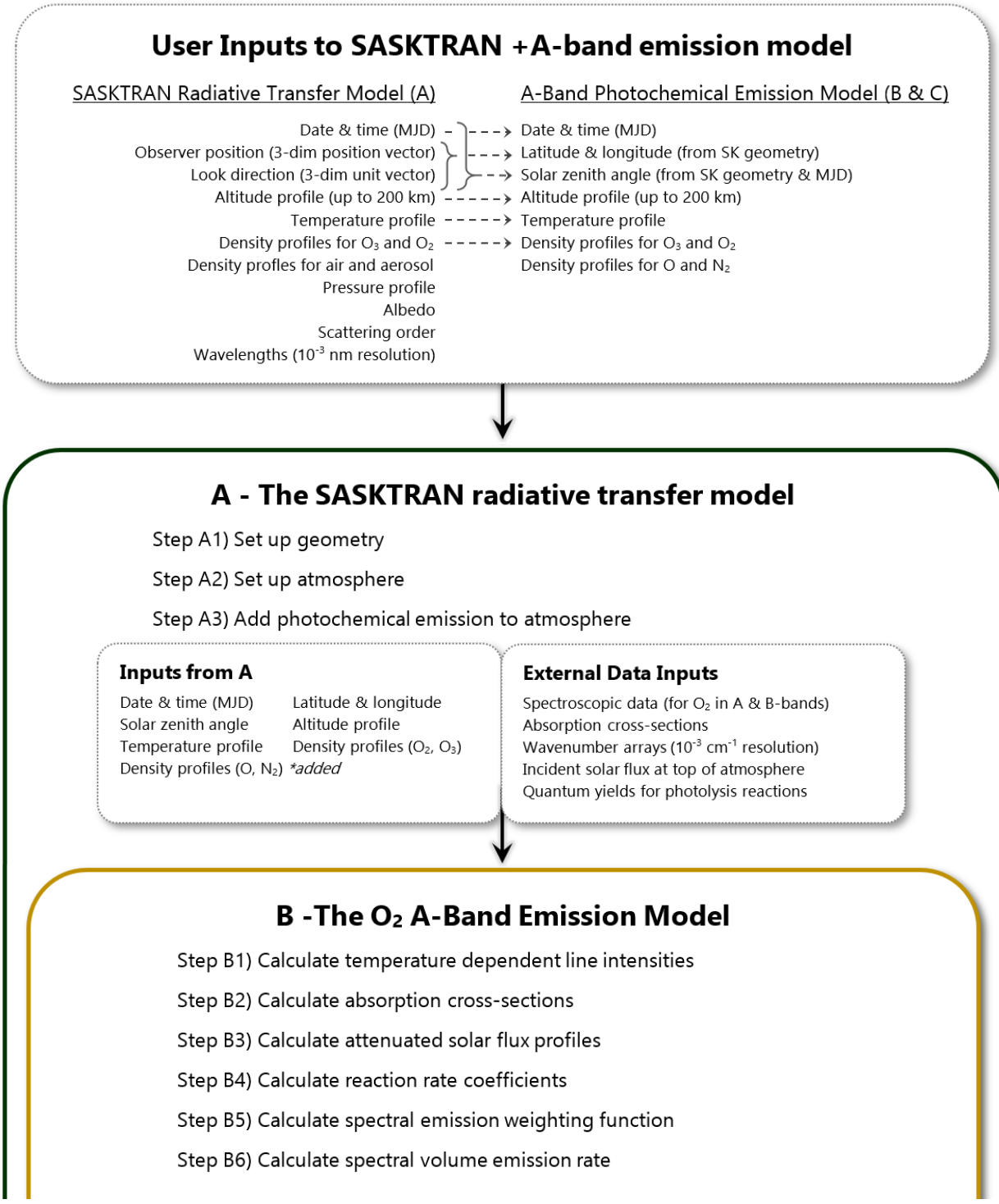
User Inputs to SASKTRAN +A-band emission model
SASKTRAN Radiative Transfer Model (A)
A-Band Photochemical Emission Model (B & C)
Date & time (MJD)
Observer position (3-dim position vector)
Look direction (3-dim unit vector)
Altitude profile (up to 200 km)
Temperature profile
Density profiles for O3 and O2
Density profles for air and aerosol
Pressure profile
Albedo
Scattering order
Wavelengths (10-3 nm resolution)
Date & time (MJD)
Latitude & longitude (from SK geometry)
Solar zenith angle (from SK geometry & MJD)
Altitude profile (up to 200 km)
Temperature profile
Density profiles for O3 and O2
Density profiles for O and N2
A - The SASKTRAN radiative transfer model
Step A1) Set up geometry
Step A2) Set up atmosphere
Step A3) Add photochemical emission to atmosphere
Inputs from A
Date & time (MJD)
Solar zenith angle
Temperature profile
Density profiles (O, N2) *added
Latitude & longitude
Altitude profile
Density profiles (O2, O3)
External Data Inputs
Spectroscopic data (for O2 in A & B-bands)
Absorption cross-sections
Wavenumber arrays (10-3 cm-1 resolution)
Incident solar flux at top of atmosphere
Quantum yields for photolysis reactions
B -The O2 A-Band Emission Model
Step B1) Calculate temperature dependent line intensities
Step B2) Calculate absorption cross-sections
Step B3) Calculate attenuated solar flux profiles
Step B4) Calculate reaction rate coefficients
Step B5) Calculate spectral emission weighting function
Step B6) Calculate spectral volume emission rate

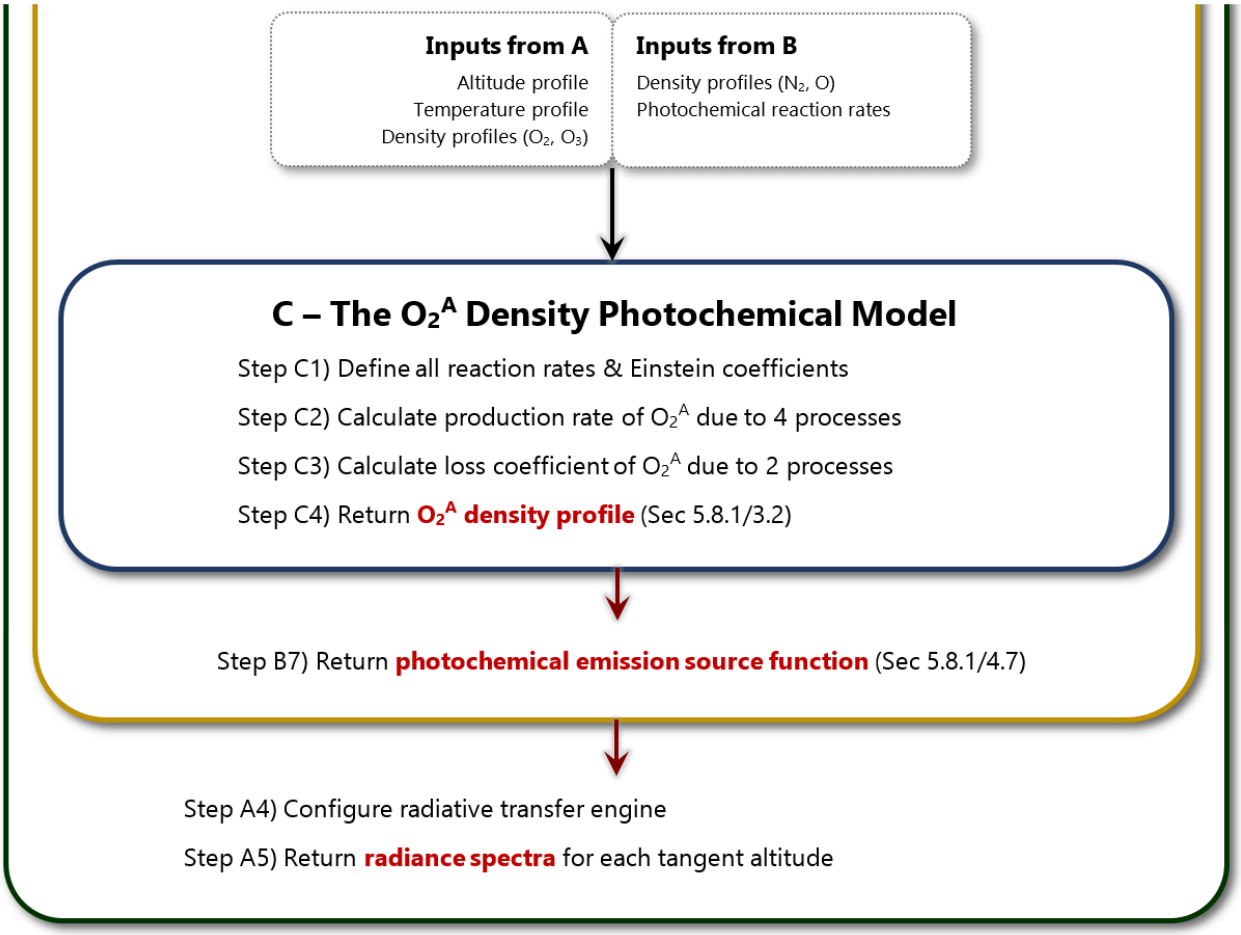

Figure 5.1: Flow-chart representing the fully integrated SASKTRAN +A-band emission model, with three layered submodels. Required inputs and resultant outputs are labeled at each layer.

5.2 User Inputs to the SASKTRAN +A-Band Emission Model

The first section of Figure 5.1 shows two separate lists of inputs to the integrated model. One list is specific to the SASKTRAN radiative transfer model (A), and the other list pertains to the combined A-band photochemical emission model (B & C). Some inputs are required by both models, which is indicated by dashed arrows from one list to the other. Some inputs are only required for one model and not the other. Although some inputs are not required until submodel B or C, it is desirable to have all necessary parameters defined at the beginning of the model run, as is shown in the diagram. Relevant data is then passed from submodel to submodel within the run as needed.

5.2.1 Geometry

The desired date and time of the simulation is entered into the model in modified Julian date (MJD) format. Measurements through the limb require an observer position in space and a look direction through the atmosphere. The SASKTRAN model uses an Earth centred coordinate system defined by the polar axis and the prime meridian. The *z*-axis is directed from the centre of the Earth to the North Pole, the *x*-axis points toward the prime meridian along the equator, and the *y*-axis is set according to a standard right-handed system (Bourassa et al., 2007). The surface of the Earth is approximated as an oblate spheroid. Observer position is defined as a three-dimensional position vector in this coordinate system, denoted $\vec{r}_0$. Look direction is a corresponding unit vector providing a direction from the observer as an origin, denoted $\widehat{\Omega}$. Together, the observer position vector $\vec{r}_0$ and the look direction vector $\widehat{\Omega}$ create a line of sight (LOS), which is used by SASKTRAN to produce its necessary geometry. Multiple lines of sight in a localized geographic area can be entered into SASKTRAN in one calculation to simulate a vertical scan through the atmospheric limb at various altitudes.

The A-band photochemical emission model also requires latitude and longitude along with solar zenith angle. These parameters can be derived from the base set-up provided by SASKTRAN from the original inputs of MJD, observer position, and look direction. Details on these derivations are provided in Section 5.3.1

5.2.2 Atmospheric Parameters

An atmosphere can be constructed in the SASKTRAN model as an object which is then passed through to the subsequent models as needed. Construction of the SASKTRAN atmosphere is discussed in Section 5.3.2 in further detail with an overview presented here.

A background altitude profile is determined by the user from the ground up with uniform spacing. All subsequent atmospheric profiles must correspond to this altitude profile, z. For the purposes of the photochemical emission model, the altitude profile and all corresponding atmospheric parameters must reach at least 200 km to provide appropriate attenuation of the incident solar flux. SASKTRAN requires background atmosphere information in the form of temperature (K), pressure (Pa), and air density

(cm^{-3}). Additional atmospheric constituents are added to create the complete atmosphere object required: density profiles of ozone (O_3), molecular oxygen (O_2), and aerosols. The photochemical emission model also requires density profiles for nitrogen (N_2) and atomic oxygen (O), which are entered in at the SASKTRAN level and passed through as needed. All atmospheric profiles are functions of the altitude profile z and all densities are in units of cm^{-3}.

The albedo of Earth is also needed to create a complete atmosphere for SASKTRAN's radiative transfer modelling. This parameter is necessary to properly simulate scattered light from Earth's surface. Albedo is added as a single value between 0 and 1, and does not require separate values for each line of sight.

All data for atmospheric parameters should correspond to approximately the same MJD and geographic location determined from the geometry derived in Section 5.1.1. An average value for latitude, longitude and MJD is determined from the multiple lines of sight (details in Section 5.3.1).

5.2.3 Calculation Parameters

To adjust the calculations required in the radiative transfer model, two parameters must be defined. The scattering order determines the amount of times photons are made to reflect off scattering points in the atmosphere. This translates to the amount of iterations through the scattering source function in the integral radiative transfer equation. A scattering order of 5 is determined sufficient for these simulations.

The wavelength range and resolution, λ, is entered as an array of wavelength values. The radiative transfer model is run entirely through to produce a radiance value for each line of sight for each wavelength point. For full radiance simulation across the A-band, a wavelength range of 758 nm to 770 nm is required with a minimum resolution of 10^{-3} nm.

5.3 SASKTRAN (A) and Emission Model (B) Set-Up

There are three general tasks which must be completed before the O_2 A-band emission model (B) can be run. The first task is to set up the SASKTRAN model (A) with its

geometry, atmospheric parameters, and configuration to include photochemical emission. Second, these inputs from submodel A are converted for use in the emission model B. Lastly, a large amount of external data is input for spectroscopic calculations in the emission model. Sources of external data must be consistent with time and place of input data initialized in submodel A and passed to B.

5.3.1 SASKTRAN Set-Up

The set-up procedure for submodel A is contained in Steps A1, A2, and A3 from Figure 5.1. SASKTRAN geometry is created in terms of MJD, observer position, and look direction. From these parameters, a line of sight (LOS) object is produced (ARG, 2018). The model then determines a tangent point for each line of sight which is defined by the point at which the line of sight is tangent to the spherical shells representing layers of the atmosphere (Figure 5.2). Each tangent point consists of latitude, longitude, and altitude. A collection of lines of sight, and therefore tangent points, is chosen in such a way as to emulate the flight of the Odin satellite upon which the OSIRIS instrument is taking measurements. With this collection of tangent points, an effective vertical scan of the atmosphere can be performed, providing radiance simulations with an altitude profile. A single reference point, $\vec{R}$, consisting of latitude, longitude, altitude, and MJD, is determined as an average of all the lines of sight provided for the vertical scan. More details on how to configure the SASKTRAN atmosphere are provided in Appendix A.1.

5.3.2 Emission Model Inputs from SASKTRAN

The emission model has the same basic requirements of geometry and atmosphere, although in some different forms from the SASKTRAN model. To maintain consistency throughout the integrated model, the geometry and atmosphere created by the SASKTRAN model from user inputs is used to initialize the geometry and atmosphere of the emission model. The exceptions are the two atmospheric density profiles not used by the SASKTRAN model (N_2 and O), which are added manually for the emission model.

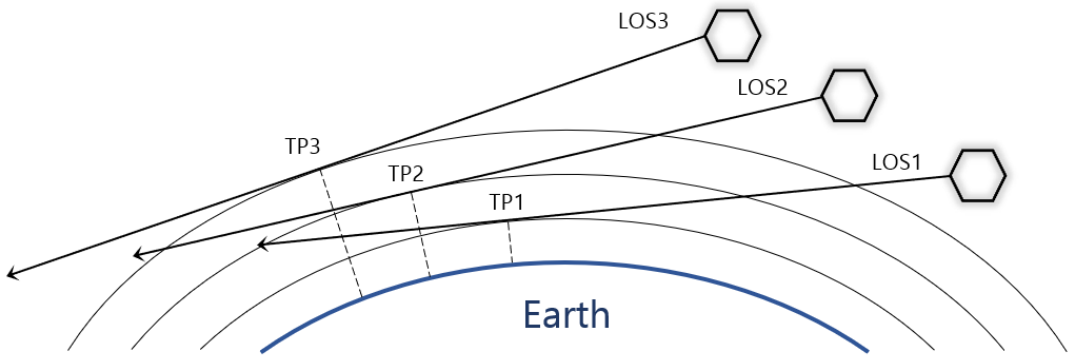

Figure 5.2: SASKTRAN limb viewing geometry, demonstrating lines of sight (LOSs) and tangent points (TPs) for each spherical shell of the atmosphere. Each LOS comes from the observer's position and look direction, and each TP is determined from the point at which its respective LOS is tangent to the atmosphere.

Position information in the form of latitude, longitude, and time is retrieved from the SASKTRAN-calculated reference point, $\vec{R}$. The altitude profile, z, comes from the user-defined array used with all atmospheric profiles in the SASKTRAN set-up. Solar zenith angle is required for the calculations of attenuated solar flux in the emission model (see Section 4.3.2) and is obtained using the SASKTRAN sun position (derivation shown in Appendix A.2).

5.3.3 Emission Model External Inputs

There are other data inputs required for the emission model alone that have no relevance to the SASKTRAN radiative transfer model and do not need to be adjusted by the user each time. These inputs have been chosen for the purposes of this use of the model, but may be changed in the future as more recent databases become available.

There are five spectral regions of interest for all calculations required in the emission model. These regions are related to relevant photochemical process outlined in Chapter 3 that contribute to the production of excited A-band O_2, O_2^A. Photon absorption by O_2 occurs in both the A and B-bands (Equations 3.7 and 3.9). Photolysis of O_2 occurs in the Lyman-α line and the Schumann-Runge continuum (SRC) (Equations 3.19 and 3.20), while

photolysis of O_3 occurs in the Hartley bands (Equation 3.21). Table 5.1 lists these five spectral regions and their respective wavenumber and wavelength ranges.

Table 5.1: Spectral regions of interest for O_2 A-band emission model.

Spectral Region (Absorber)	**Chemical Reaction** (Equation number)	**Wavenumber Range** (cm^{-1})	**Wavelength Range** (nm)
A-band (O_2)	Photon absorption Equation (3.8)	13 165 – 12 844	760 – 779
B-band (O_2)	Photon absorption Equation (3.9)	14 557 – 14 301	687 – 699
Lyman-α line (O_2)	Photolysis of O_2 Equation (3.19)	82 237	121.6
Schumann-Runge continuum (O_2)	Photolysis of O_2 Equation (3.20)	76 923 – 57 143	130 – 175
Hartley bands (O_3)	Photolysis of O_3 Equation (3.21)	50 505 – 32 362	198 – 309

There are four groups of data required in the spectral ranges stated above. Spectroscopic data is required from the HITRAN database for the A and B-bands. Temperature independent absorption cross-sections are required of O_2 in the Lyman-α line and SRC, and of O_3 in the Hartley bands. Incident solar flux data is required for calculation of attenuated solar flux, which is obtained from NASA's SORCE project. Quantum yields are required to complete the photolysis coefficient calculations (Section 4.3), and are determined from various sources. More details on format, data sources, and references are provided in Appendix A.3.

5.4 Emission Model (B) Implementation

The theory and derivations for the emission model are provided in Chapter 4. Details presented in this section are for software implementation of the theory in order to produce the photochemical emission source function, $J_{\mathrm{emi}}(\lambda, z)$, for use in the SASKTRAN radiative transfer model. This is the second successive submodel in the integrated SASKTRAN +A-

band emission model, and contains the photochemical model within it for calculation of O_2^A density profiles.

From the three required spectroscopic parameters of transition wavenumber, line strength at standard temperature, and lower state energy value (Appendix A.3.1), all necessary spectroscopic values can be calculated. The equation for calculating temperature relative line strengths (Step B1) is derived in Section 4.1 as

$$S_j(T) = S_j(T_s)\frac{T_s}{T}\exp\left(\frac{hc}{k}E_{0j}^{\nu}\left(\frac{T-T_s}{TT_s}\right)\right). \tag{5.1}$$

High-resolution absorption cross-sections are then determined for both the A and B-bands of O_2 (Step B2) by applying Doppler broadening to the temperature dependent line strengths (Section 4.3.1):

$$\sigma(\nu,T) = \sum_j S_j(T)D_j(\nu,T)\ , \tag{5.2}$$

where

$$D_j(\nu,T) = \frac{1}{\alpha_j(T)\sqrt{\pi}}\exp\left[-\left(\frac{\nu-\nu_j}{\alpha_j(T)}\right)^2\right];\quad \alpha_j(T) = \frac{\nu_j}{c}\left(\frac{2kT}{m}\right)^{1/2} \tag{5.3}$$

Note that the subscript j denotes a discrete dependence on transition wavenumber, ν_j, while the uniform high-resolution wavenumber array is denoted ν (10^{-3} cm^{-1} resolution). The line strengths $S_j(T)$ contain one array per temperature of line strengths versus transition wavenumber. Doppler line shape, $D_j(\nu,T)$, depends on both transition wavenumber, ν_j, and the high-resolution wavenumber array, ν (Equation 5.3). Figure 4.3 demonstrates that for each temperature, there are j number of wavenumber ν dependent arrays, each with a Gaussian centred on their respective transition wavenumbers, ν_j.

Incident solar flux data is acquired from NASA's SORCE project in the Lyman-α line, the SRC, the Hartley bands, and the A and B-bands (Section 5.3.3, Appendix A.3.3). Because SORCE provides measurements of incident solar flux in units of $W/m^2/nm$, a unit conversion is required to obtain the desired flux with units of photons/s/cm^2/nm.

Attenuated solar flux (Step B3) is then found using incident flux and absorption cross-sections in Equation 5.2 for each of the five spectral areas of interest listed in Table 5.1. Equation 5.4 demonstrates the general formula:

$$F(\lambda, z) = F(\lambda, z_\infty) \exp\left(-\sec\chi \int_z^{z_\infty} \sum_x [x]\sigma_x(\lambda, z)\, dz' \right) \tag{5.4}$$

Depending on the source of the absorption cross-section, attenuated flux may be wavenumber or wavelength dependent, and may therefore require additional unit conversion. Details of these calculations as well as all relevant unit conversions are covered in Appendix A.4.1.

Section 4.3 provides the theory behind the g-factors of photon absorption in the A and B-bands and the J coefficients for photolysis of O_2 and O_3 in the Lyman-α line, SRC, and Hartley bands:

$$g_{\mathrm{A,B}}(z) = \int_\nu F(\nu, z)\sigma(\nu, z)\, d\nu' \tag{5.5}$$

$$J_{\mathrm{L,S,H}}(z) = \int_\lambda F(\lambda, z)\, \sigma(\lambda)\, \phi\ \ d\lambda' \tag{5.6}$$

Calculating photochemical reaction rates (Step B4) depends on attenuated solar flux and absorption cross-section, and so are wavenumber or wavelength dependent with respect to the cross-section source. The spectral dependence is also consistent with attenuated solar flux. More details are available in Appendix A.4.2.

The spectral emission weighting function, $W_{\mathrm{emi}}(\nu, z)$, (Step B5) is derived in Section 4.5 from the spectrally dependent spontaneous emission Einstein coefficient, $A_{10,j}$. It is a normalized version of the theoretical spectral VER, $\eta'_{\mathrm{spec}}(\nu, T)$, obtained from the Doppler broadening of the discretized VER based on transition wavenumber, $\eta_j(T)$:

$$W_{\mathrm{emi}}(\nu, T) = \frac{\eta'_{\mathrm{spec}}(\nu, T)}{\int \eta'_{\mathrm{spec}}(\nu, T)\, d\nu'} \tag{5.7}$$

where

$$\eta'_{\text{spec}}(\nu, T) = \sum_j \eta_j(T) D_j(\nu, T) \tag{5.8}$$

and

$$\eta_j(T) = \mathcal{C}\, \nu_j^2\, S_j(T) \exp\left(\frac{-hc\nu_j}{kT}\right) \tag{5.9}$$

The calculation of the weighting function is similar in practice to calculating absorption cross-sections of O_2 in the A and B-bands (Section 5.6.2), in that it consists of the Doppler line shape being applied to each discrete VER line. As a result, the same high-resolution wavenumber array, ν, must be used for appropriate realization of the Doppler shape, and requires a resolution of 10^{-3} cm^{-1}. Emission is only considered in the A-band, so the wavenumber array for B-band is not necessary here.

Calculation of the spectral VER, $\eta_{\text{spec}}(\nu, z)$, (Step B6) is discussed in Section 4.6 and requires a VER profile, $\eta_{\text{pro}}(z)$. It is merely the result of applying the spectrally dependent weighting function in Equation 5.7 to each altitude point in the VER profile:

$$\eta_{\text{spec}}(\nu, z) = W_{\text{emi}}(\nu, z)\, \eta_{\text{pro}}(z) \tag{5.10}$$

where

$$\eta_{\text{pro}}(z) = F_C A_{1\Sigma} \left[O_2^A\right] \tag{5.11}$$

The VER profile depends on the density profile of O_2 excited to the A-band, O_2^A. It is at this stage that the O_2^A density photochemical model (submodel C) is run. From the density profile $\left[O_2^A\right]$, the spectral VER above may be found, and subsequently the photochemical emission source function, $J_{\text{emi}}(\lambda, z)$, for ultimate submission to the SASKTRAN model atmosphere.

5.5 Photochemical Model (C)

The theory and derivations for the photochemical model are provided in Chapter 3. Details presented in this section are for software implementation of the theory in order to produce

the density profile of O_2^A for use in the emission model (submodel B). This is the third and final successive submodel in the integrated SASKTRAN +A-band emission model.

5.5.1 Photochemical Model Inputs

Inputs to the photochemical model are summarized in Section 3.6. The altitude profile, temperature profile, and density profiles for O_3 and O_2 are passed from the SASKTRAN model (submodel A), through the emission model (submodel B) into the photochemical model (submodel C). The density profiles not needed in the SASKTRAN atmosphere (N_2 and O) are added at the beginning of the emission model and then passed into the photochemical model as well. The photochemical reaction rates discussed in Section 5.4 are calculated in the Step B4 of the emission model and then also passed into the photochemical model, to complete the necessary data input.

5.5.2 Photochemical Model Implementation

All reaction rates necessary for the chemical reactions contained in the photochemical model are defined at this stage (Step C1), with the exception of the photon absorption (g_A and g_B) and photolysis (J_L, J_S, and J_H) reaction rates calculated in the emission model. Table 3.3 contains values and references for all reaction rates, some of which are constant, and some of which depend on temperature.

The total production rate of O_2^A is calculated as outlined in Section 3.4 (Step C2), with production processes due to photon absorption in the A-band, photon absorption in the B-band and subsequent quenching, collisional excitation due to $O(^1D)$, and the two-step Barth process. The loss coefficient of O_2^A is determined as in Section 3.5 (Step C3), and is due to spontaneous emission in the A-band, as well as electronic quenching. A density profile of produced O_2^A is determined from each process for scientific purposes, but only the total density profile is required for calculation in the emission model (Step C4).

5.6 Completion of the SASKTRAN +A-Band Emission Model

The final stage of the integrated SASKTRAN +A-band emission model is to receive the outputs of each successive submodel and produce the ultimate result of simulated radiance

spectra at each tangent altitude in the set-up geometry. This section describes implementation of obtaining the final result of the three combined models.

5.6.1 Outputs from Photochemical Model and Emission Model

The innermost submodel, the photochemical model, returns a single profile of O_2^A density corresponding to the originally user-defined uniform altitude profile, z, reaching up to 200 km (Step C4 in Figure 5.1). This profile is returned to the middle submodel, the emission model, which can use the array along with the spectral emission weighting function $W_{\text{emi}}(\nu, z)$ to produce a VER spectrum across the A-band in 10^{-3} cm^{-1} resolution at each altitude point, $\eta_{\text{spec}}(\nu, z)$ (Step B7).

Finally, calculation of the photochemical emission source function, $J_{\text{emi}}(\lambda, z)$, can be performed (Section 4.7). The source function is an emission per solid angle, and the O_2 molecule is assumed to emit in all directions equally, so the spectral VER can be divided by the solid angle of a complete sphere (4π steradians):

$$J_{\text{emi}}(\nu, z) = \frac{\eta_{\text{spec}}(\nu, z)}{4\pi} \tag{5.12}$$

Note that the emission source function at this point is still wavenumber dependent, and has units of photons/s/cm^3/cm^{-1}/ster. It is necessary to convert the source function to wavelength dependence for use in the SASKTRAN radiative transfer model. The conversion is completed using unit differentials, as shown in Appendix A.4.1, providing the wavelength dependent emission source function, $J_{\text{emi}}(\lambda, z)$, shown at four different altitudes in Figure 5.3.

5.6.2 SASKTRAN Radiative Transfer Calculation

The photochemical emission source function in Equation 5.12 is passed as a table of values to the outermost submodel, the SASKTRAN radiative transfer model. The SASKTRAN engine must be configured for proper iteration of the forward radiative transfer equation (Step A4). An option is set to instruct the engine to include emissions in the model atmosphere. The scattering order and wavelength range for SASKTRAN are set here, the

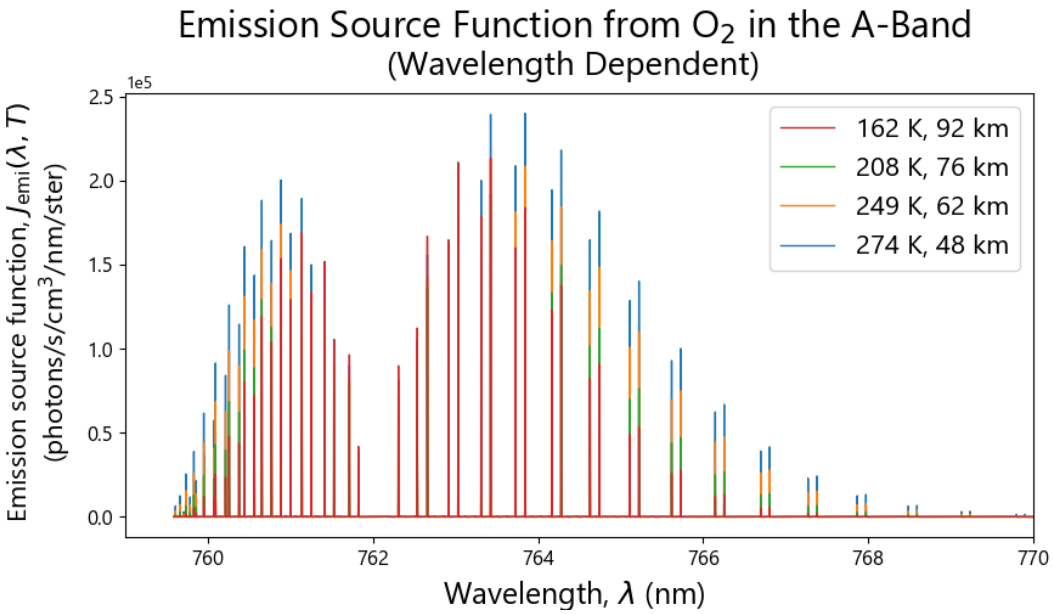

Figure 5.3: Four spectra at different altitudes and corresponding temperatures for the final photochemical emission source function, $J_{\text{emi}}(\lambda, z)$, produced by the full O_2 A-band photochemical emission model.

values for which are stated in Section 5.2.3. The forward model is then run with one radiance value produced per wavelength and tangent altitude (Step A5), iterating through the radiative transfer equation discussed in Section 4.7 and shown again here:

$$I(\vec{r}_0, \hat{\Omega}) = \int_{s_1}^{0} J(s, \hat{\Omega}) \exp\left(-\tau(s, 0)\right)\, ds + \tilde{I}(s_1, \hat{\Omega}) \exp\left(-\tau(s_1, 0)\right) \tag{5.13}$$

where the source term now includes both scattering and photochemical emission processes:

$$J(s, \hat{\Omega}) = J_{\text{scat}}(s, \hat{\Omega}) + J_{\text{emi}}(s, \hat{\Omega}) \tag{5.14}$$

The final result consists of one full radiance spectrum across the A-band per tangent altitude. Verification and demonstration of the model along with results of its application are presented in Chapter 6.

5.7 Chapter Summary

To accurately model the radiance spectra due to A-band emission from the O_2 molecule, three separate models are required: a full radiative transfer model of the atmosphere, a spectral emission model for the A-band, and a photochemical model providing the density of excited O_2. The three models are combined as Submodels A, B, and C to create the integrated SASKTRAN +A-band emission model (Section 5.1). Figure 5.1 provides a diagrammatic description of the implementation of these three submodels. The O_2^A density photochemical model (Submodel C) and the O_2 A-band emission model (Submodel B) are designed to produce a photochemical emission source function which can be added to the radiative transfer equation in the SASKTRAN model (Submodel A). The new model is capable of simulating light propagation in a model atmosphere which includes scattering, absorption, and photochemical emission properties.

The general format of user inputs to the full model are described in Section 5.2. Section 5.3 contains set-up instructions for the outermost Submodels A and B. Implementation of Submodel B, the O_2 A-band emission model (Section 5.4), involves calculations of photochemical reaction rates for Submodel C and the spectral weighting emission function. Submodel C, the O_2^A density photochemical model (Section 5.5), receives some original inputs of atmospheric state from Submodel A as well as the calculated photochemical reaction rates from Submodel B. The density profile of O_2^A is then calculated and passed back to Submodel B, which in turn calculates the photochemical emission source function to pass to Submodel A (Section 5.6). The end result of the integrated SASKTRAN +A-band emission model is a simulated radiance spectrum provided across the A-band for each of the tangent altitudes. More technical details on sections throughout are provided in Appendix A.

The geometry parameters used as inputs to the integrated SASKTRAN +A-band emission model are meant to emulate the real position of the OSIRIS instrument on the Odin satellite. Therefore, the radiance spectra produced by the model should be comparable to those radiance spectra measured by OSIRIS at the same tangent altitudes. This provides a method of verification of the integrated SASKTRAN +A-band model.

Specific values and sources for the atmospheric parameters are chosen to represent the atmosphere at OSIRIS's time and position. These profiles and the radiance spectra results are presented for verification in Chapter 6, along with other preliminary demonstrations of the use of this model for analysis of MATS measurements in the future.

Chapter 6

Model Verification and Results

The fully integrated SASKATRAN +A-band emission model contains the updated original SASKTRAN radiative transfer model which includes an additional source term due to photochemical emission from the O_2 molecule in the A-band. The integrated model consists of three submodels whose theory and implementation are discussed in the previous three chapters. Verification of the final integrated SASKTRAN +A-band model is provided by comparing modelled radiance spectra with actual limb measurements from the OSIRIS instrument. Geometry inputs are designed to match the position of OSIRIS at the time of the measurements, and atmospheric input data is found for the same time and location. The radiance simulations provided by the integrated SASKTRAN +A-band emission model are also compared to spectra simulated by the original SASKTRAN model to demonstrate the necessity of including photochemical emission in the A-band spectrum above 40 km altitude.

The verified model is further used with the established inputs for demonstration purposes in support of the MATS mission. A full demonstration of the functionality of the integrated SASKTRAN +A-band emission model is provided by simulating radiance spectra throughout the MLT beginning with the simplest modeling case and increasing complexity with each run. This confirms the necessity of using a radiative transfer model capable of modelling multiple scatter from the ground and atmosphere, absorption processes from atmospheric constituents, and photochemical emission properties in order to produce the most accurate results possible for MLT radiance simulations. These results are made further relevant to the MATS mission by adding a polar mesospheric cloud (PMC) into the model atmosphere and producing the expected radiance spectra to be

observed by the MATS satellite. MATS filters are applied to the simulated spectra to obtain modelled instrument readings, whose sensitivity is tested with respect to changes in temperature and cloud properties. With these MATS demonstrations, the full use of the integrated SASKTRAN +A-band model is shown and validated as a necessary step forward in studying the mesosphere and lower thermosphere.

6.1 User Inputs

As discussed in Chapter 5 and listed clearly in Figure 5.1, there are several inputs to the integrated SASKTRAN +A-band emission model that must be user-defined (Section 5.2). Because this work is focused on the preliminary development and verification of this model, the results presented are demonstrative in nature and the inputs are chosen to match the time and location of the OSIRIS measurements used for comparison in Section 6.2. The OSIRIS measurements chosen for comparison belong to vertical scan 06432012, which contains 24 separate measurements in the limb-viewing geometry. Measurements from this scan have been used in verification of the original SASKTRAN model (Bourassa et al., 2007) so it is known that good agreement between the model and the measurements already exists.

Some inputs to the integrated model are not changed throughout all the simulations provided in this thesis but may be changed in the future if so desired. Other inputs are varied individually to balance between calculation time and precision, or to demonstrate the sensitivity of the model in various contexts. User inputs belong to three categories: geometry, atmospheric parameters, and calculation parameters. Each of the three categories and sources of their respective inputs is discussed below, with a representation of chosen inputs for model verification listed in Table 6.1. Sections 6.1.1, 6.1.2, and 6.1.3 discuss the contents of Table 6.1 in further detail.

Table 6.1: User inputs to the integrated SASKTRAN +A-band emission model, corresponding to an OSIRIS scan containing 24 radiance measurements. Average values for the 24 MJD, observer position, and look direction parameters are given.

GEOMETRY INPUTS

USER-DEFINED		SASKTRAN DERIVED	
OSIRIS Scan #	06432012	**Tangent Altitudes**	9 – 69 km, 3 km intervals
MJD (avg)	52393.38	**Reference Point**	82°N, 41°E, 24/04/2002
Observer Position (avg)	(-1.25, 2.56, 6.36) $\times 10^6$	**Solar Zenith Angle**	67.8°
Look Direction (avg)	(0.692, -0.722, -0.00965)		

ATMOSPHERE PARAMETERS (USER-DEFINED)

Altitude Profile	0.5 – 199.5 km, 1 km intervals
Temperature Profile	From MSIS-E-90 Model (K)
Density Profiles - Air, O_2, N_2, O	From MSIS-E-90 Model (cm^{-3})
Pressure Profile	From SASKTRAN/OSIRIS retrievals (Pa)
Density Profiles - Aerosol, O_3	From SASKTRAN/OSIRIS retrievals (cm^{-3})
Albedo	0.828 → From SASKTRAN/OSIRIS retrievals

CALCULATION PARAMETERS (USER-DEFINED)

Scattering Order	5 (sufficient for most atmospheres)
Wavelength Array	758 – 770 nm, 10^{-3} nm intervals

6.1.1 Geometry

One vertical scan taken by the OSIRIS instrument on the Odin satellite is completed in less than 2 minutes. There is a separate timestamp, observer position vector, and look direction unit vector associated with each of the 24 measurements performed in the scan. In Table 6.1, an average value is given for each input for demonstration purposes, where timestamp is in MJD format, observer position is in Earth-centred geodetic coordinates, and look direction is a unit vector with the observer taken as origin. The set of 24 measurements form 24 lines of sight as discussed in Section 5.3.1, each with their own tangent point. While each tangent point consists of a latitude, longitude, and altitude, the

altitudes are of most interest for results and referred to as tangent altitudes. The OSIRIS scan used in this verification contains 24 tangent altitudes which range from 9 to 69 km with approximate intervals of 3 km.

Section 5.3.1 also describes the reference point as an average value for the set of measurements given in terms of latitude, longitude, altitude, and MJD. The reference point is calculated by SASKTRAN and is of use when collecting atmospheric data for the appropriate time and place. The reference point derived from this set of measurements has a latitude of 82°N, a longitude of 41°E, and occurs on April 24, 2002. The sun position is calculated by SASKTRAN as a single value for the whole scan and is found in geocentric coordinates for use in the O_2 A-band emission model for attenuated solar flux profiles. The solar zenith angle derived from this user input geometry is 67.8°.

6.1.2 Atmospheric Parameters

Section 5.2.2 describes a background altitude profile that is user-defined and is used as a reference for all subsequent atmospheric profiles. All atmospheric density profiles must reach at least 200 km altitude for accurate solar flux attenuation through the top of the atmosphere, so the altitude array defined here ranges from 0.5 km to 199.5 km in 1 km intervals, providing 200 atmospheric points. All atmospheric data is found at the location and time defined by the reference point in Section 6.1.1, on the same intervals as the altitude profile. Atmospheric profiles of temperature, air density, and densities of O_2, O, and N_2 were obtained from the MSIS-E-90 Atmosphere Model, available online at ccmc.gsfc.nasa.gov/modelweb/models/msis_vitmo.php. Atmospheric pressure and aerosol density profiles are from retrievals using SASKTRAN in conjunction with OSIRIS measurements (ARG, 2019) up to 100 km and then extrapolated log-linearly to 200 km. O_3 density from the ground to 75 km altitude was obtained from OSIRIS retrievals (ARG, 2019) with the MLT ozone peak around 80 km added manually to emulate (Kaufman et al., 2003), and also extrapolated to 200 km.

The background atmospheric state in SASKTRAN is created by the temperature, pressure, and air density (Figure 6.1). Additional atmospheric constituents with density profiles for O_2, O_3, and aerosol are added as climatologies to the SASKTRAN model

atmosphere to provide absorption and scattering properties. Density profiles for O_2 and O_3 are passed into the O_2 A-band photochemical emission model along with density profiles of N_2 and O. All additional atmospheric species density profiles are shown in Figure 6.2. The Earth's albedo at the location and time of the reference point was found through the same atmospheric retrievals using SASKTRAN and OSIRIS measurements, and has the value of 0.828.

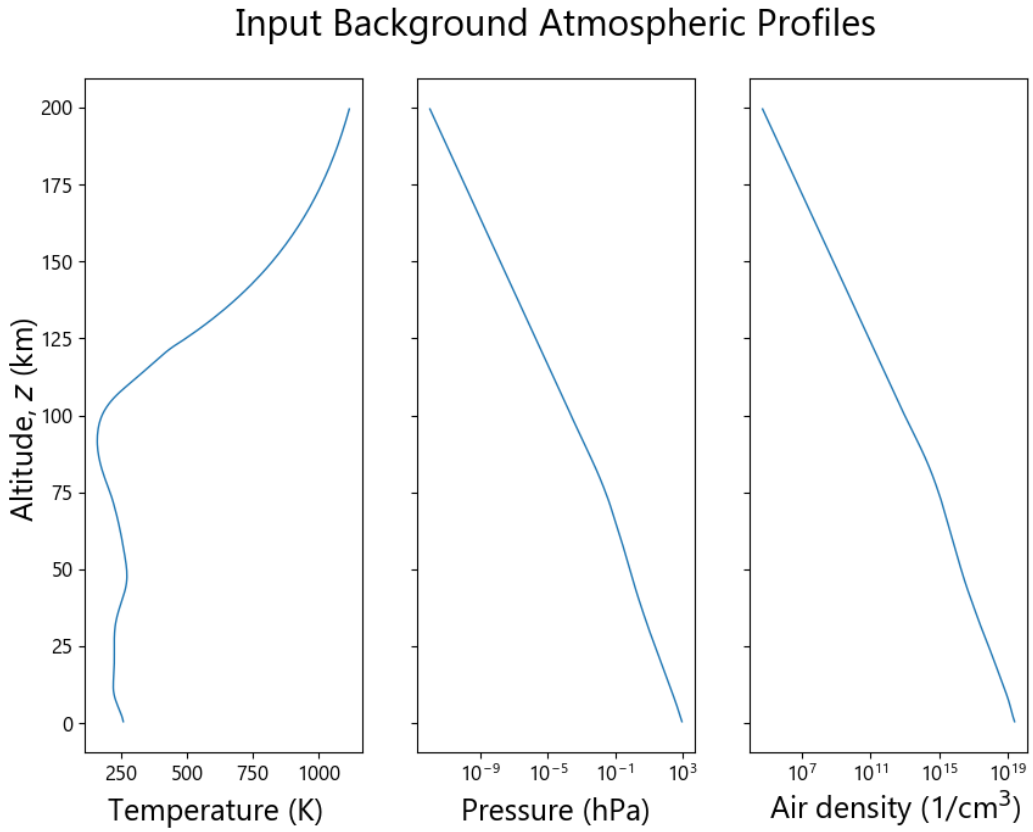

Figure 6.1: Atmospheric profiles used to create the background atmospheric state in the SASKTRAN model.

6.1.3 Calculation Parameters

Section 5.2.3 describes parameters that are necessary in tuning the calculation of the forward model performed by the SASKTRAN radiative transfer model. Only two parameters are considered for the purposes of demonstrating O_2 A-band emissions in the

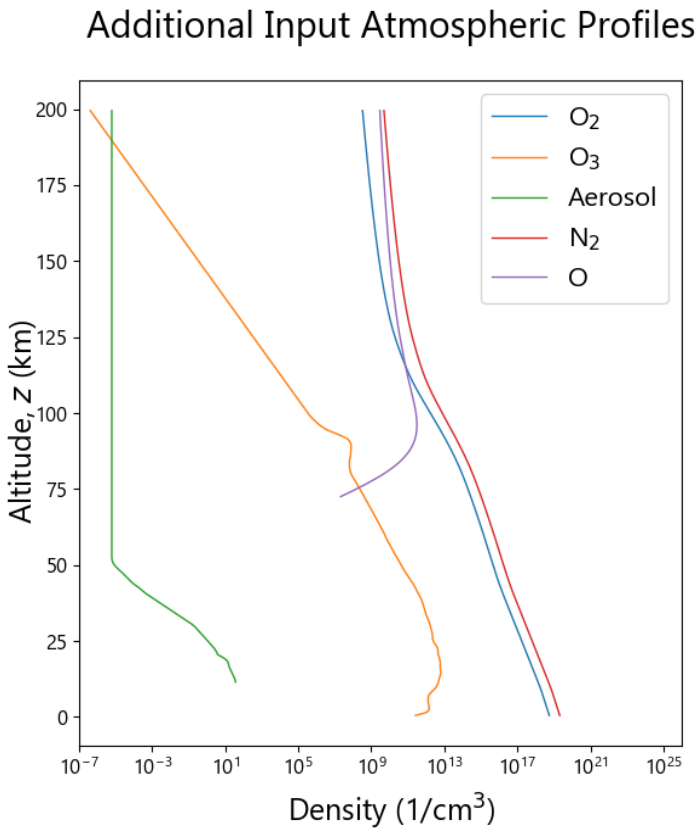

Figure 6.2: Additional atmospheric constituents' density profiles used in the SASKTRAN model to simulate absorption and scattering processes, and used in the O_2 A-band emission model to simulate photochemical emission.

MLT: the scattering order of the radiative transfer model and the wavelengths at which the forward model is run. A scattering order of 5 is sufficient for modeling in this context and reduces program run time. The wavelengths necessary for viewing emissions in the A-band range from 758 nm to 770 nm and the array must have a minimum resolution of 10^{-3} nm to resolve all individual absorption/emission lines.

6.2 Verification of the SASKTRAN +A-Band Emission Model

Verification of the integrated SASKTRAN +A-band emission model is achieved by simulating radiance spectra in the atmospheric limb and comparing with measurements from the OSIRIS instrument. Inputs pertaining to the geometry of the observations are obtained from OSIRIS data for the scan in question (Section 6.1.1). Atmospheric data up

to 200 km altitude is taken either from retrieval methods using SASKTRAN simulations or from the MSIS-E-90 model and are all found at the same location and time as the OSIRIS scan (Section 6.1.2).

6.2.1 OSIRIS Measurements

One vertical OSIRIS scan contains 24 radiance measurements at tangent altitudes from 9 to 69 km at approximately 3 km intervals. Figure 6.3 shows the full OSIRIS radiance observations across the entire spectrum measured by the instrument for five different tangent altitudes. Measurements are taken from 280 nm to 810 nm with 1 nm resolution (Roth et al., 2007). The spectra are magnified over the A-band (from 758 nm to 770 nm) in Figure 6.4. The choice of the five different tangent altitudes is to show the progression from absorption-dominant observations in the UTLS to the emission-dominant A-band in the MLT. Emission becomes a significant contributor above 40 km altitude, where the A-band radiance exhibits almost a flat line with the balance between emission and absorption (Figure 6.4, 41 km). At 54 km and 69 km, the photochemical emission in the A-band fully dominates any absorption processes and the two-lobed spectral shape from Figure 2.8 becomes apparent.

6.2.2 Simulations from the Original SASKTRAN Model

To produce comparable simulations, the original SASKTRAN radiative transfer model is run across the A-band from 758 nm to 770 nm at a resolution of 10^{-3} nm. The original SASKTRAN only exhibits phenomena of atmospheric absorption and photon scattering and does not incorporate photochemical emission into the radiative transfer source function. Figure 6.5 shows the simulated radiance spectra at full resolution at the same five chosen tangent altitudes. It is clear that absorption alone is occurring at the transition wavenumbers, as is expected at lower altitudes, but the emission should be seen contributing at 41 km and dominating at 54 km and 69 km. However, without the integration of the O_2 A-band emission model, only the absorption lines are displayed.

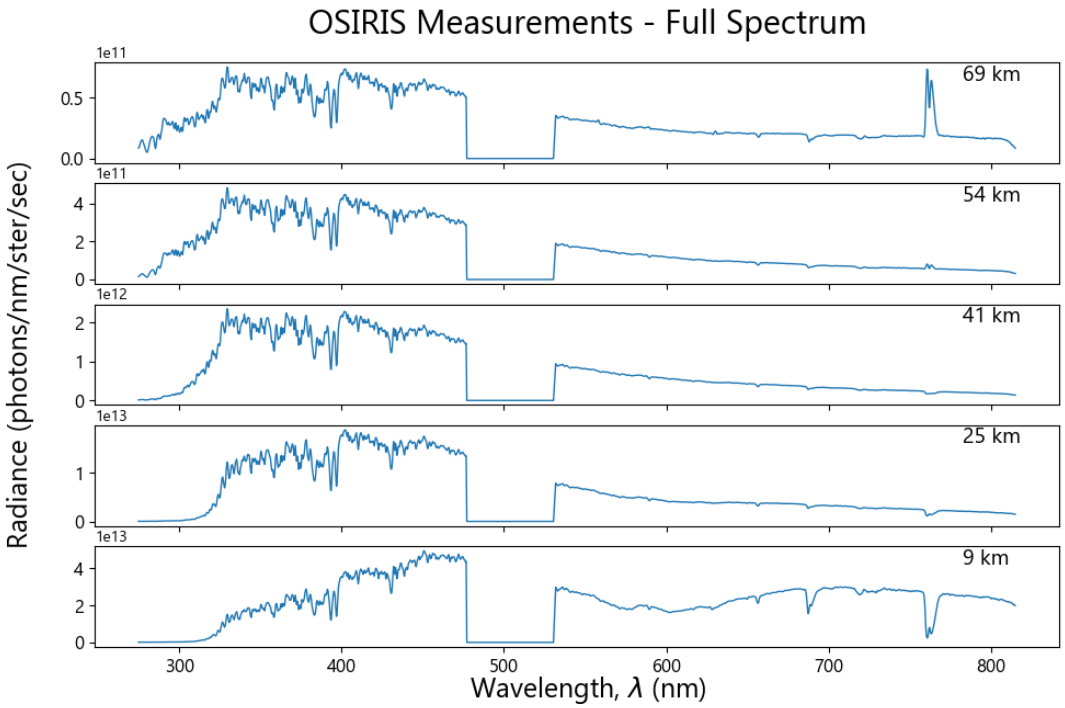

Figure 6.3: OSIRIS radiance measurements over the full instrument spectrum at five different tangent altitudes.

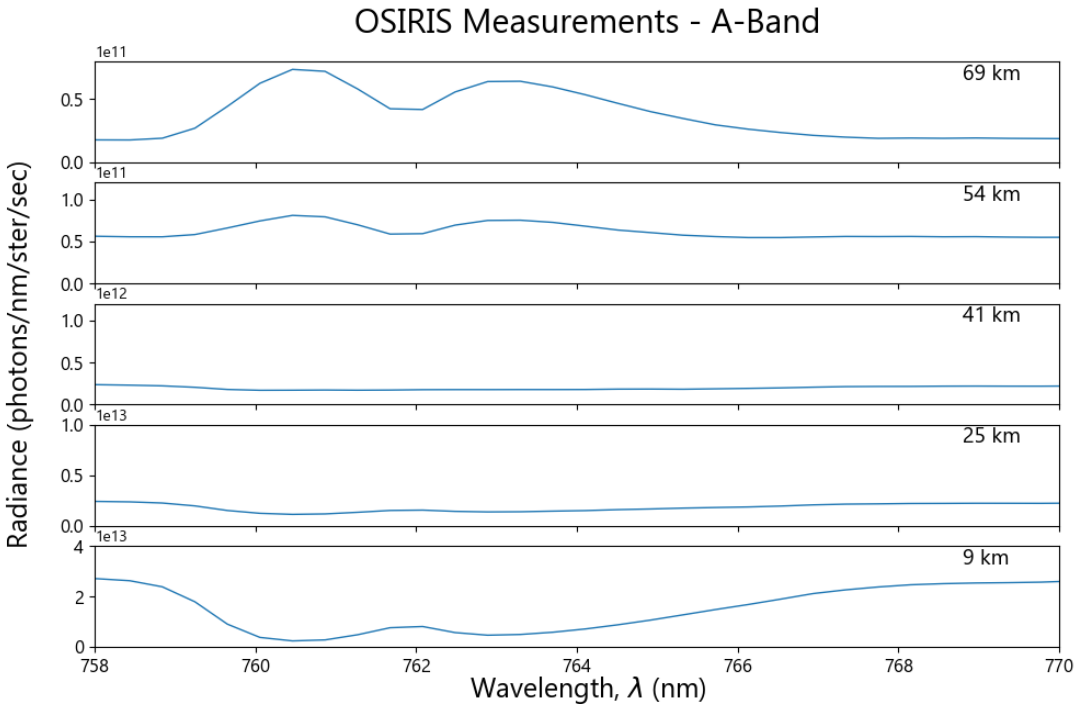

Figure 6.4: OSIRIS radiance measurements magnified in the A-band at five different tangent altitudes. Notice the progression from O_2 absorption in the A-band at lower altitudes to photochemical emission viewed above 50 km.

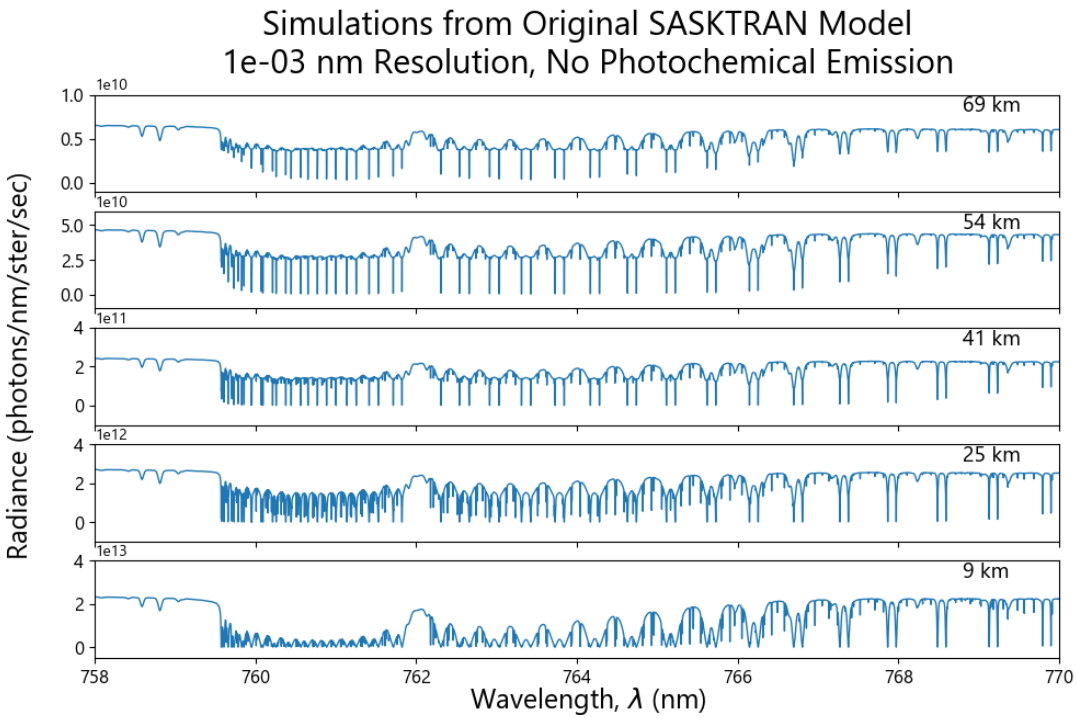

Figure 6.5: The original SASKTRAN radiative transfer model is used to simulate radiance in the A-band with 10^{-3} nm wavelength resolution at five different tangent altitudes. The original model does not include photochemical emission from O_2, and so all that is seen are absorption lines at all altitudes presented.

While photochemical emission is ignored in these simulations, the absorption processes may be more closely observed. Figure 6.6 demonstrates a magnification of Figure 6.5 within the 763 nm wavelength. Notice the different shapes of absorption at the same transition wavelengths/wavenumbers as discussed in Section 4.1 and depends on quantum rules of energy transition for the O_2 molecule. Line intensities represent the probability of a transition occurring at each wavelength and have no width due to the energies required being discrete. However, atmospheric broadening gives width to the transition lines in different ways depending on their circumstance (Section 4.2). The only kind of line broadening that is considered above 40 km altitude in the MLT is Doppler broadening, which occurs due to the relative velocities at which molecules are traveling in the atmosphere. Doppler broadening results in narrow Gaussians occurring at each transition

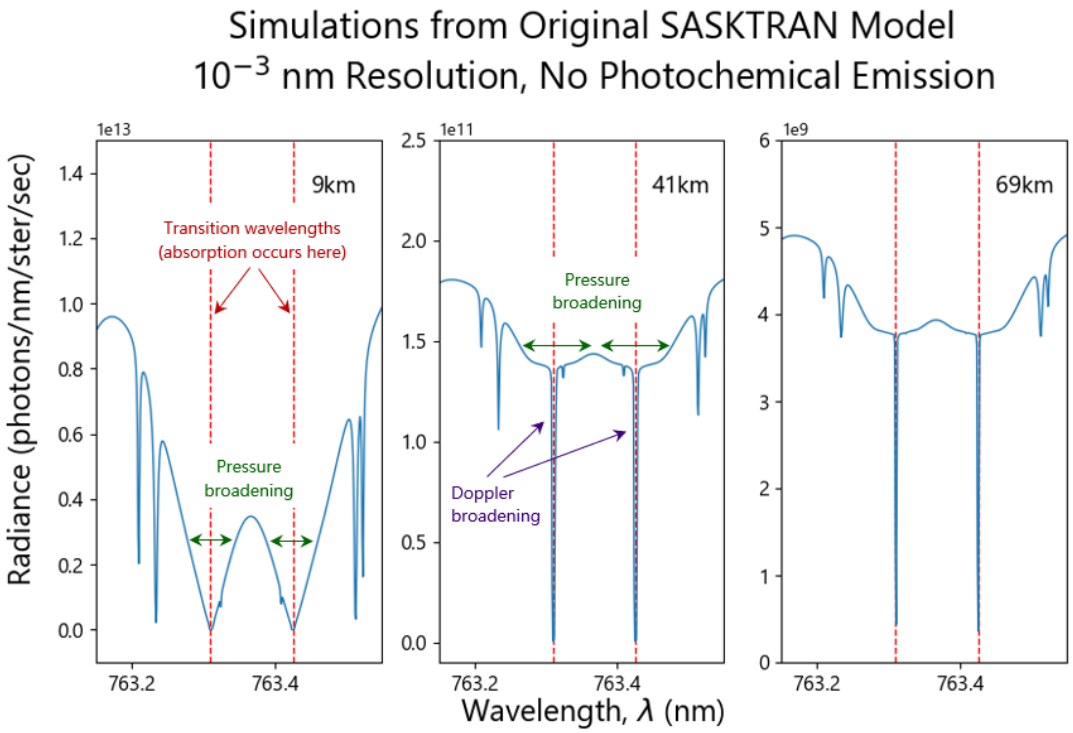

Figure 6.6: Simulated radiance spectra from the original SASKTRAN radiative transfer model with no photochemical emission, magnified from Figure 6.5. Absorption due to Doppler broadening (purple) is observed from the relatively narrow absorption lines occurring at the transition wavelengths (red), while the absorption due to pressure broadening (green) from lower altitudes is recognizable as the wider troughs of lesser magnitude occurring at the same wavelengths.

wavelength, having some width and a smooth, curved shape, but still appearing as seemingly discrete lines on a scale such as depicted in Figure 6.5.

The wider absorption characteristic seen in Figure 6.6 (demonstrated by the green arrows) is due to pressure broadening at lower altitudes. Pressure broadening occurs when collisions between molecules impart enough energy to disrupt natural transitions between states and provides a much wider range of allowable transitions on top of the original transition wavelength. It is expected to see the pressure broadening dominate at the lower altitudes in Figure 6.6, and still contribute significantly until 40 km altitude, but it is still visible at higher altitudes where it has been considered negligible (Petty, 2006). The reason it is still apparent at these high altitudes is due to the ability of the SASKTRAN model

to simulate light reflecting from Earth's surface. Radiation that has reached the surface and reflected up to be viewed at higher altitudes has traveled through the lower atmosphere and experienced pressure broadening, creating this signature at higher altitudes. In the full demonstration of SASKTRAN functionality in Section 6.3, it can be seen that the pressure broadening at higher altitudes does not exist when albedo is considered zero in running the model. Further discussion is available in that section.

For direct comparison with the OSIRIS measurements across the A-band in Figure 6.4, the full resolution SASKTRAN simulations in Figure 6.5 must be convolved to have an effective resolution of 1 nm. Figure 6.7 demonstrates the result of a convolution that reduces the effective resolution of the SASKTRAN radiance in Figure 6.5 from 10^{-3} nm down to 1 nm. Notice the overall two-lobed spectral shape becomes apparent, if only in the lower altitudes due to strong absorption features. It is necessary to perform the SASKTRAN simulation at the higher resolution of 10^{-3} nm to obtain all spectral information from each thin transition line, and then apply a convolution to 1 nm, rather than running the original simulation at 1 nm resolution. Section 6.2.4 contains all comparisons of SASKTRAN simulations with the original OSIRIS measurements.

6.2.3 Simulations from the SASKTRAN +A-Band Emission Model

The integrated SASKTRAN +A-band emission model is run across the A-band from 758 nm to 770 nm at a resolution of 10^{-3} nm for direct comparison with the original SASKTRAN radiative transfer model. The full resolution results are shown alone in Figure 6.8 and compared with the original SASKTRAN results in Section 6.2.4. Figure 6.9 shows the same magnification of the 763 nm wavelength as shown in Figure 6.6. The Doppler broadening of absorption lines is still apparent at lower altitudes, while the emission peaks become apparent as low as 29 km. However, due to the relative thinness of the emission lines, they are still not a significant contribution to the total radiance until above 41 km. The emission lines occur within the absorption lines and do not exhibit any pressure broadening, since the radiative signal from photochemical emission does not reflect from

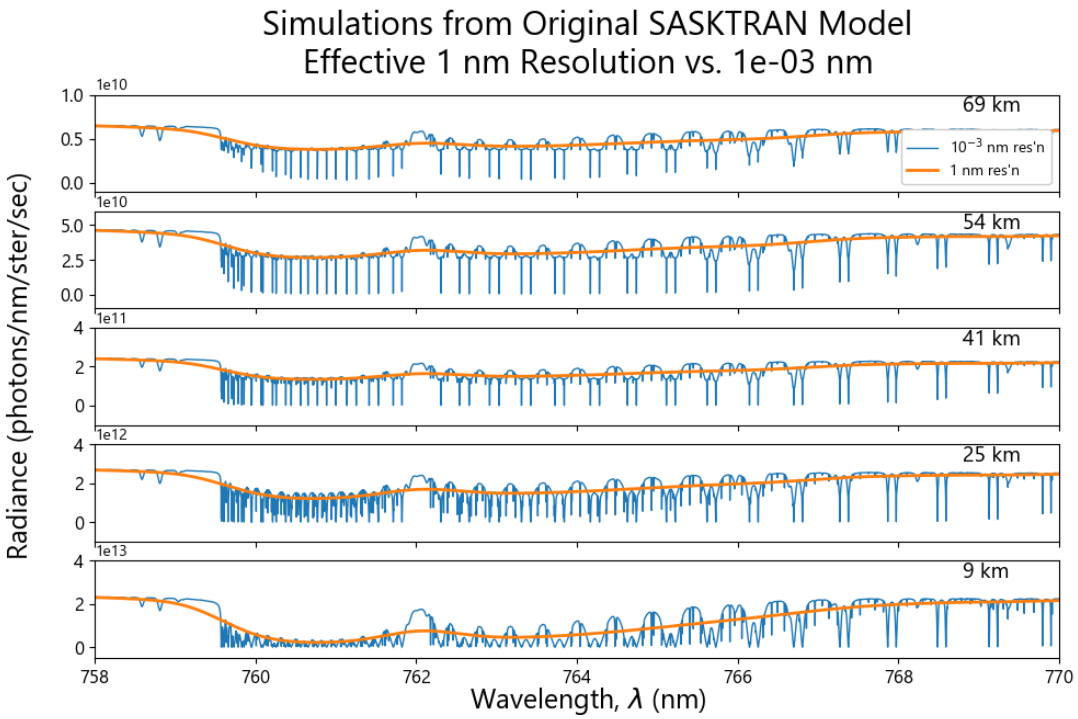

Figure 6.7: A convolution applied to the full resolution radiance produced by the original SASKTRAN radiative transfer model in Figure 6.5 provides simulated spectra with effective resolution of 1 nm. This can be used to compare with OSIRIS measurements occurring at 1 nm intervals.

the Earth to travel through the lower atmosphere. The radiance spectra at 69 km is dominated by the emission signal and looks very similar to the spectral VER shown for four different altitudes in Figure 4.7.

A convolution is again performed on the full resolution simulated radiances from Figure 6.8 to produce spectra with an effective resolution of 1 nm for direct comparison with the OSIRIS measurements (Section 6.2.4). Figure 6.10 demonstrates the result of this convolution. Notice in comparison with Figure 6.7 that the spectral shape at high altitudes now demonstrates some positive relative radiance due to emission, rather than just the absorption A-band spectrum. The effective 1 nm signal must be shown on a different vertical axis scale at the higher altitudes as it is more than a full order of magnitude smaller than the peaks of the emission lines. This is due to the width of the emission lines being so small that the area under each Doppler-broadened Gaussian is only a fraction of

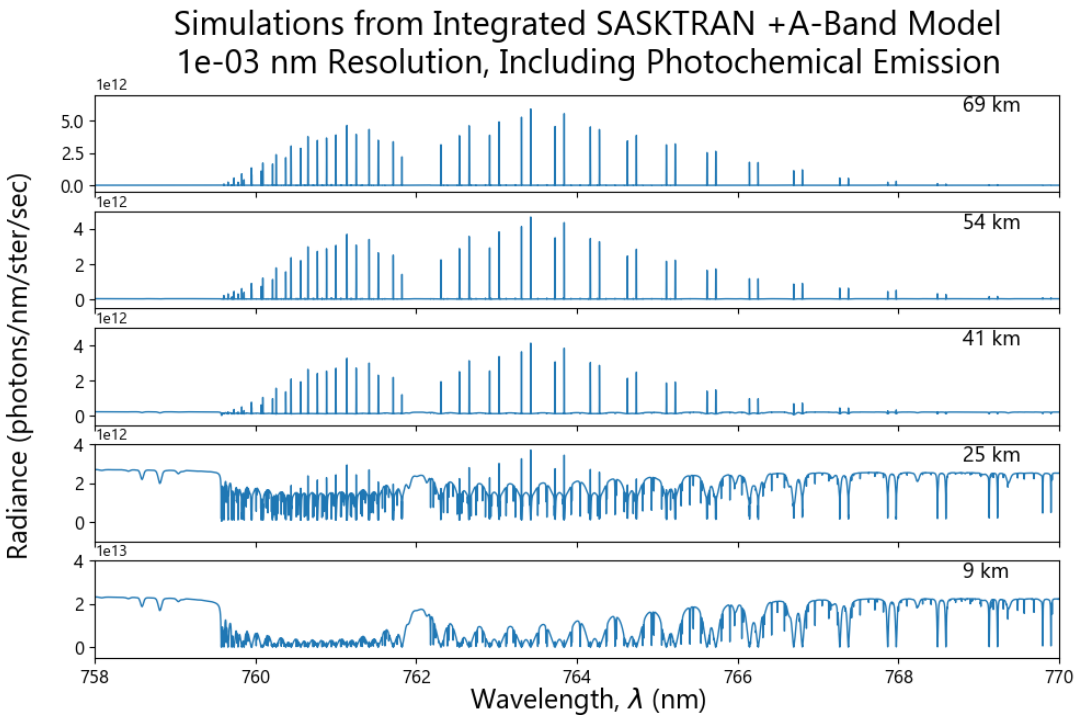

Figure 6.8: The integrated SASKTRAN +A-band emission model is used to simulate radiance in the A-band with 10^{-3} nm wavelength resolution at five different tangent altitudes. The integrated model includes photochemical emission from O_2 in the A-band, and so emission lines are seen within the absorption lines as altitude increases.

the height. At lower altitudes, the pressure-broadened absorption lines are much wider, so the 1 nm scale signal at 9 km is on the same order of magnitude as the depth of the lines.

6.2.4 Comparisons and Verification

This thesis describes the process by which the original SASKTRAN radiative transfer model was upgraded to produce the integrated SASKTRAN +A-band emission model. The original model was capable of simulating atmospheric attenuation due to absorption as well as multiple-scattering processes both within the atmosphere and from the ground due to Earth's albedo. The upgraded model is still able to handle both absorption and scattering, but can also model photochemical emission due to the O_2 molecule in the A-band. For appropriate resolution of the absorption and emission lines of O_2 in the A-band, both versions of the SASKTRAN model are run over a wavelength range from 758 nm to

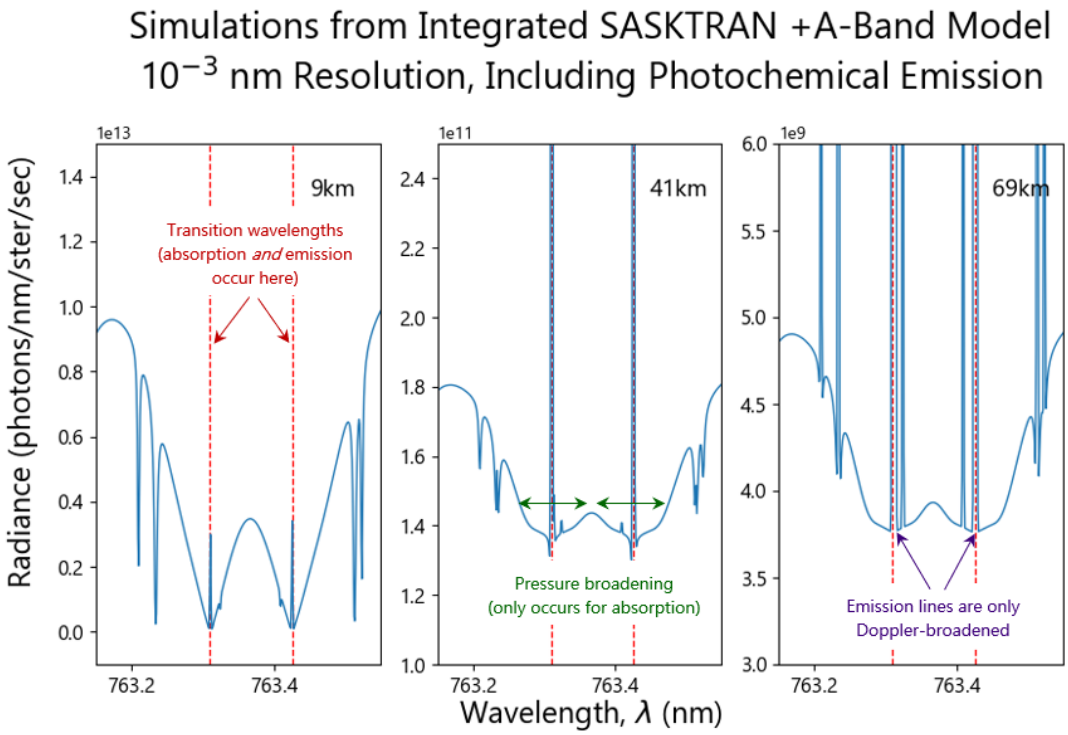

Figure 6.9: Simulated radiance spectra from the integrated SASKTRAN +A-band emission model, magnified from Figure 6.8. Absorption subject to Doppler broadening (purple) and pressure broadening (green) is still observed, and emission lines are visible originating from within the absorption lines (red) at low altitudes. Emission lines are unaffected by pressure broadening because emission is negligible at low altitudes and therefore does not travel through a thicker atmosphere.

770 nm with 10^{-3} nm resolution. Figure 6.11 contains two plots which demonstrate the difference between the two models at full resolution, scaled to better display the absorption lines and emission phenomena respectively.

In order to verify the results of the upgraded model, the simulations are compared with instrument measurements from OSIRIS in the atmospheric limb. Radiance measurements from OSIRIS have a 1 nm wavelength resolution (Figure 6.4), and so a convolution is performed on the full-resolution simulations in Figure 6.11 to produce an effective resolution of 1 nm that still contains all information acquired at the higher resolution of 10^{-3} nm. Figure 6.12 shows the result of the convolutions overlaid on the full-resolution spectra, scaled to the convolution results.

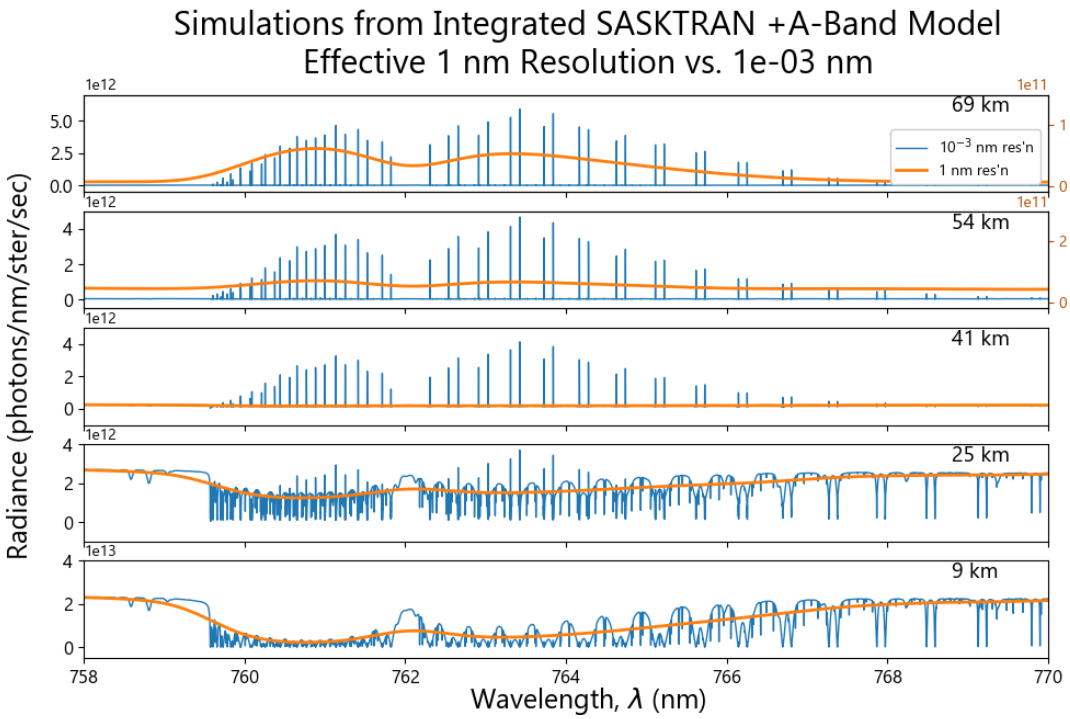

Figure 6.10: A convolution applied to the full resolution radiance produced by the integrated SASKTRAN +A-band emission model in Figure 6.8 provides simulated spectra with effective resolution of 1 nm. This can be used to compare with OSIRIS measurements occurring at 1 nm intervals.

The observed radiance spectra from the OSIRIS instrument are overlaid with the simulated spectra with effective resolution of 1 nm. Figure 6.13 shows the full-resolution and 1-nm simulations plotted together from Figure 6.12 with the OSIRIS measurements added for comparison. Notice that both models agree nicely with OSIRIS measurements until approximately 40 km altitude. Above this point, the measurements demonstrate contribution from O_2 photochemical emission. The simulations from the original SASKTRAN model do not reflect these contributions, while the updated SASKTRAN +A-band emission model still match the observations from OSIRIS. In the 54 km and 69 km altitude plots, it is clear that the original SASKTRAN model simulations are not reproducing any emission characteristics, while the SASKTRAN +A-band model produces simulated spectra that more accurately follow the trend of the OSIRIS observations.

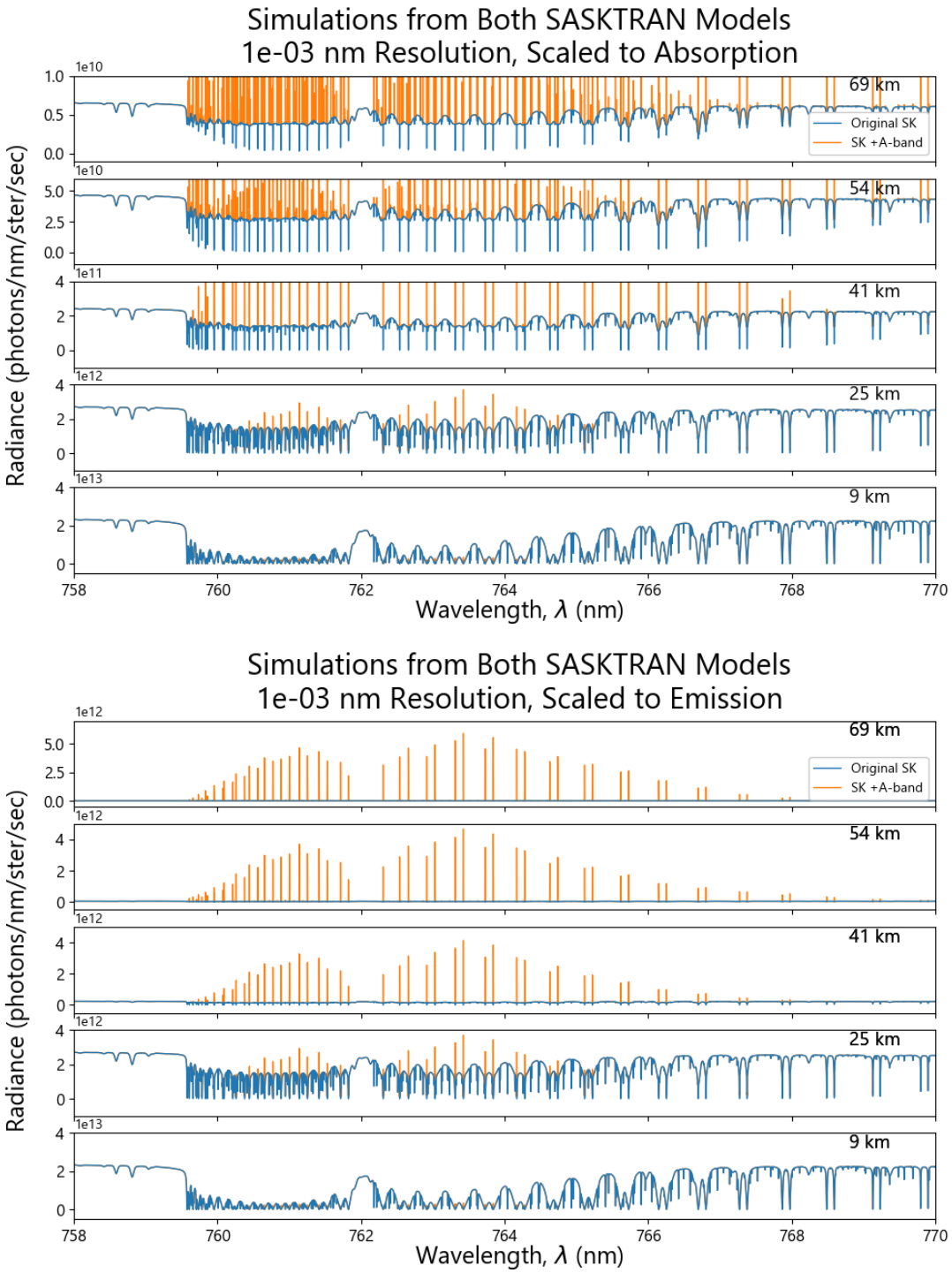

Figure 6.11: Full-resolution simulated radiance spectra across the A-band from both the original SASKTRAN radiative transfer model (only absorption and scattering) and the integrated SASKTRAN +A-band emission model (including emission), scaled to demonstrate absorption phenomena (top) and emission phenomena (bottom).

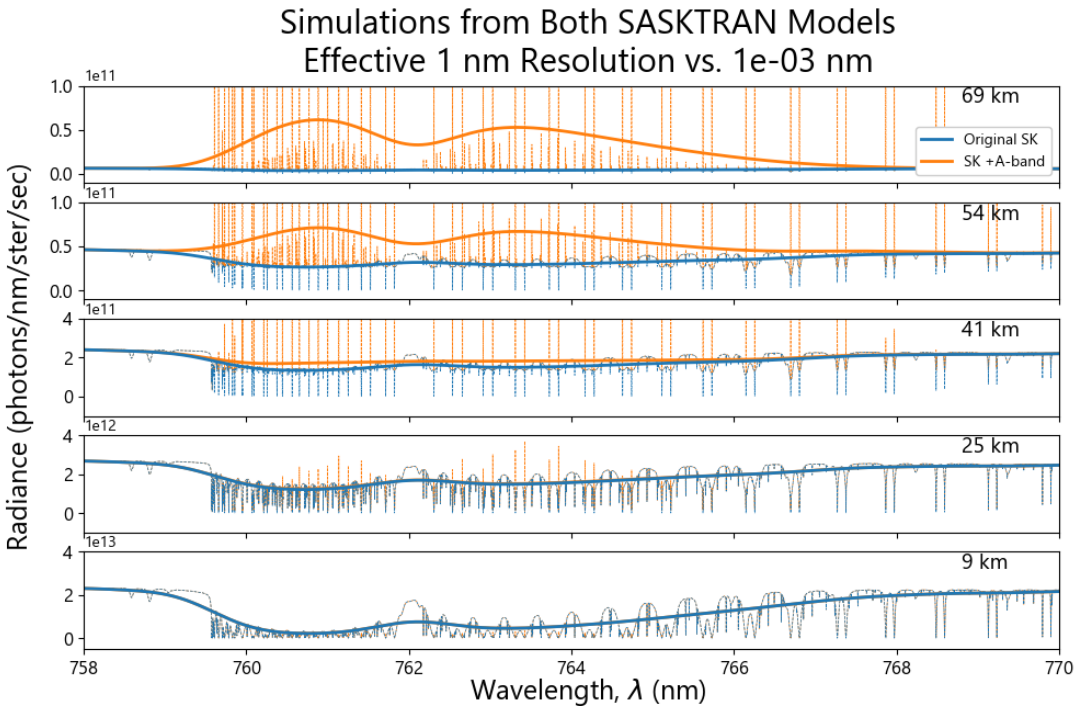

Figure 6.12: A convolution performed on the full-resolution simulated radiance spectra provided from both SASKTRAN models (original with only absorption/scattering and integrated +A-band emission) produces a spectrum with effective resolution of 1 nm.

While Figure 6.13 clearly demonstrates the improvements made by integrated the O_2 A-band photochemical emission model into the original SASKTRAN framework, there is still significant discrepancy between observations and simulated spectra at altitudes above 50 km. When referring to the edges of the spectra, around 758 nm and 770 nm wavelengths, a vertical offset can be seen between the instrument measurements and the simulations. At higher altitudes, the signal to noise ratio of the OSIRIS instrument decreases as the stray light that infiltrates the spectrograph becomes more significant in proportion to the desired signal. In addition, a slight wavelength bias of –0.25 nm is visible in the OSIRIS measurements due to miscalibration, which must be corrected. If the measurement is corrected for the vertical and horizontal offsets, the results are even more agreeable than in Figure 6.13. Figure 6.14 shows the final verification of the integrated SASKTRAN +A-band emission model with simulation correction for stray light affecting the observed radiance signal from OSIRIS at high altitudes.

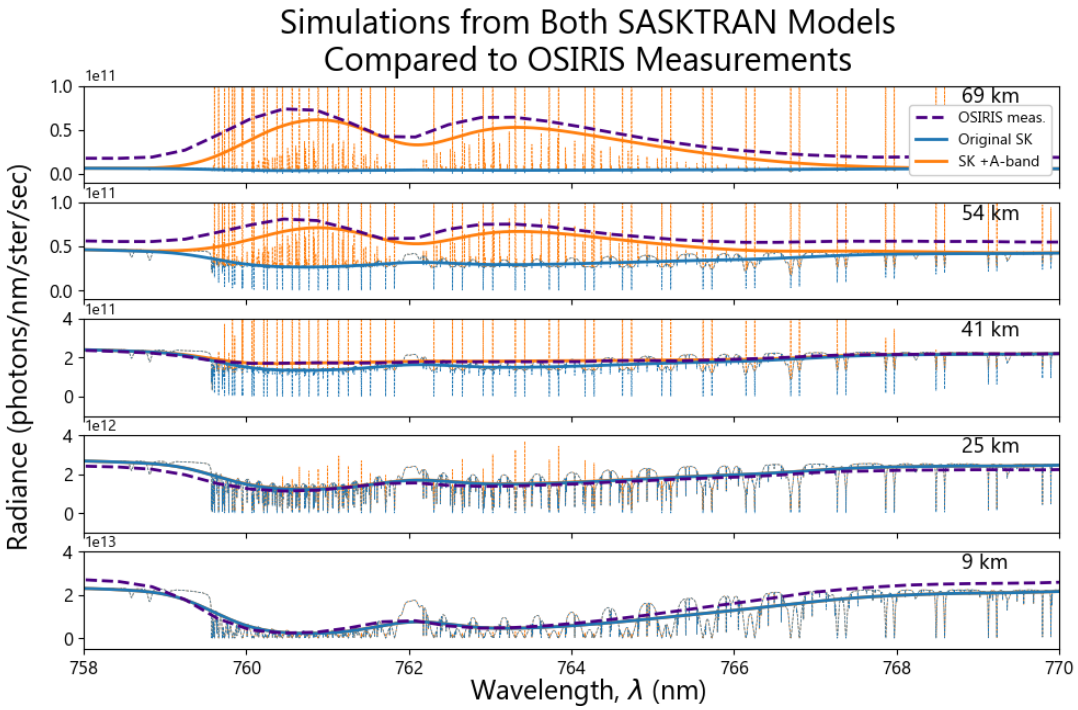

Figure 6.13: OSIRIS measurements compared with the 1 nm-resolution and full-resolution radiance spectra simulated by both the original SASKTRAN radiative transfer model (without emission) and the integrated SASKTRAN +A-band emission model.

6.3 Using the SASKTRAN +A-Band Model for MATS

The implementation of an emission model into the existing SASKTRAN framework was done largely in support of the MATS project (background in Section 2.3.3), whose purpose is to take radiance measurements in the NIR and UV spectra in the MLT region with limb-viewing and nadir geometry where polar mesospheric clouds (PMCs) exist (background in Section 2.1.2). PMCs occur in both hemispheres near the summer solstice at high latitudes at approximately 82 km altitude (Alpers et al., 2000). Work presented in this section demonstrates the ability of the integrated SASKTRAN +A-band emission model to simulate mesospheric radiance spectra which indicate the existence of PMCs. This ability indicates the possibility of using the integrated SASKTRAN model in the inverse to accept radiance measurements from the MATS instrument and ultimately

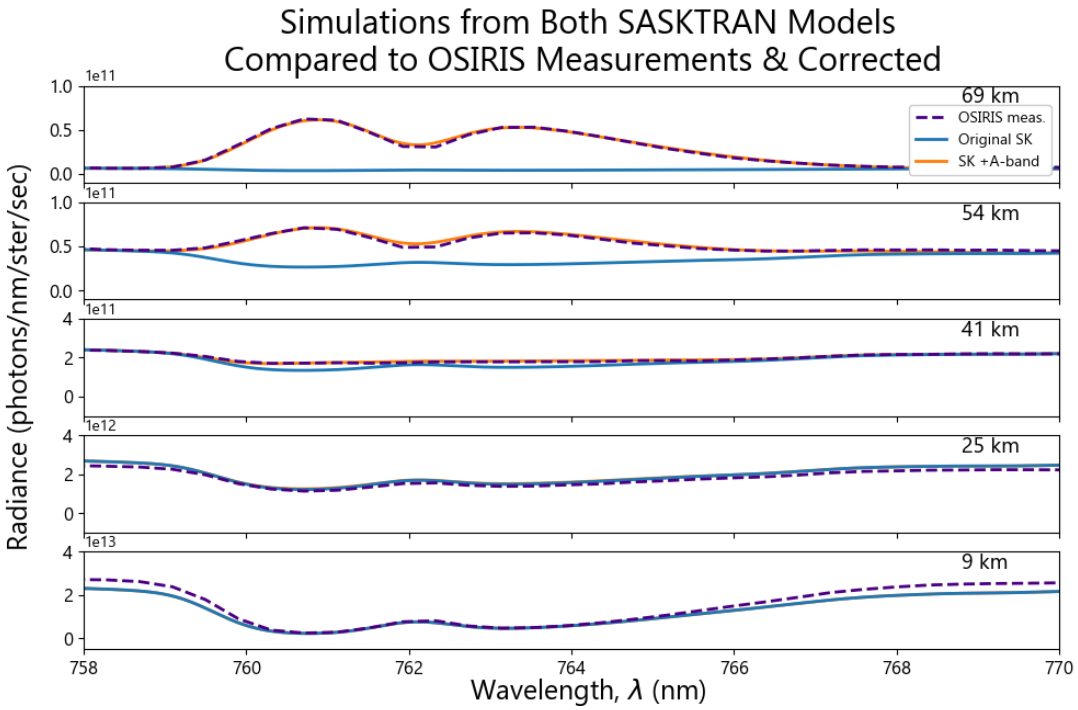

Figure 6.14: OSIRIS measurements corrected for vertical offset due to stray light and horizontal offset due to wavelength bias. The corrected measurements are compared with the effective 1 nm-resolution radiance spectra simulated by both the original SASKTRAN radiative transfer model (without emission) and the integrated SASKTRAN +A-band emission model.

determine temperature in the MLT. Figure 6.15 shows input atmospheric profiles and the location of the PMC to be simulated (between 81 km and 83 km).

The spectral filters on the MATS instrument are designed in such a way as to measure the magnitude ratio between the core and the entirety of the A-band emission spectrum shape. Section 2.2 describes the effect of temperature on spectral line intensity in the core region of a particle's spectral signature. At lower temperatures, more emissions are seen from the core region than at higher temperatures (Figure 2.11). For the most efficient observation of this phenomena, four filters are constructed. Filter 1 covers the total radiance over the whole A-band. Filter 2 covers only the radiance within the core of the A-band spectrum, whose integrated magnitude is subject to change from temperature variation. Filters 3 and 4 measure the background radiance on either side of the band as

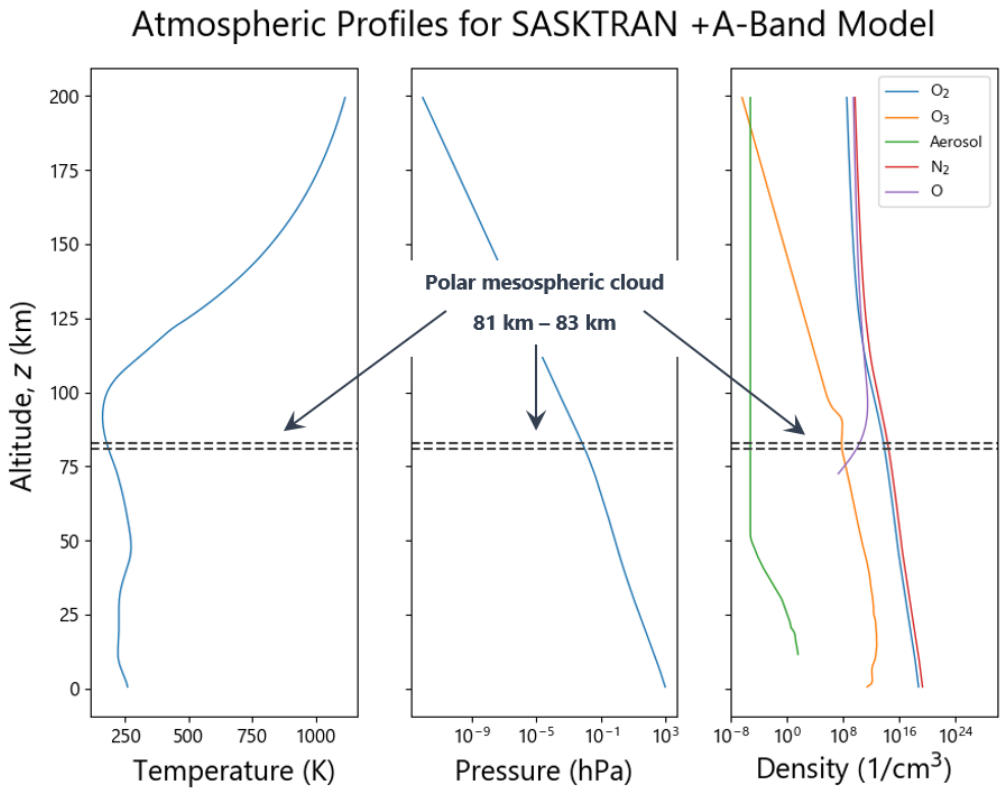

Figure 6.15: Location of PMC to be simulated in the integrated SASKTRAN +A-band emission model with respect to atmospheric profile inputs.

a control. Figure 6.16 illustrates an example of these four filters as they apply to the wavelength-dependent emission source function from O_2 in the A-band (Figure 5.3).

The purpose of this work is so that the MATS satellite may take radiance measurements in the filtered regions as shown in Figure 6.16 and determine mesospheric temperature from shape of the A-band emission spectrum (Figure 2.11 demonstrates the change in spectrum shape with a change in temperature). The goal is to take measurements within a PMC, which is modelled as a collection of aerosol particles at altitudes near 80 km. The existence of aerosols requires the scattering in a model atmosphere, and the high altitude necessitates simulation of emission features, therefore requiring the full capability of the integrated SASKTRAN +A-band emission model. This section provides a demonstration of the SASKTRAN +A-band model with respect to the MATS project. The following plots present the spectral radiance simulated by SASKTRAN across 1 nm within the A-band

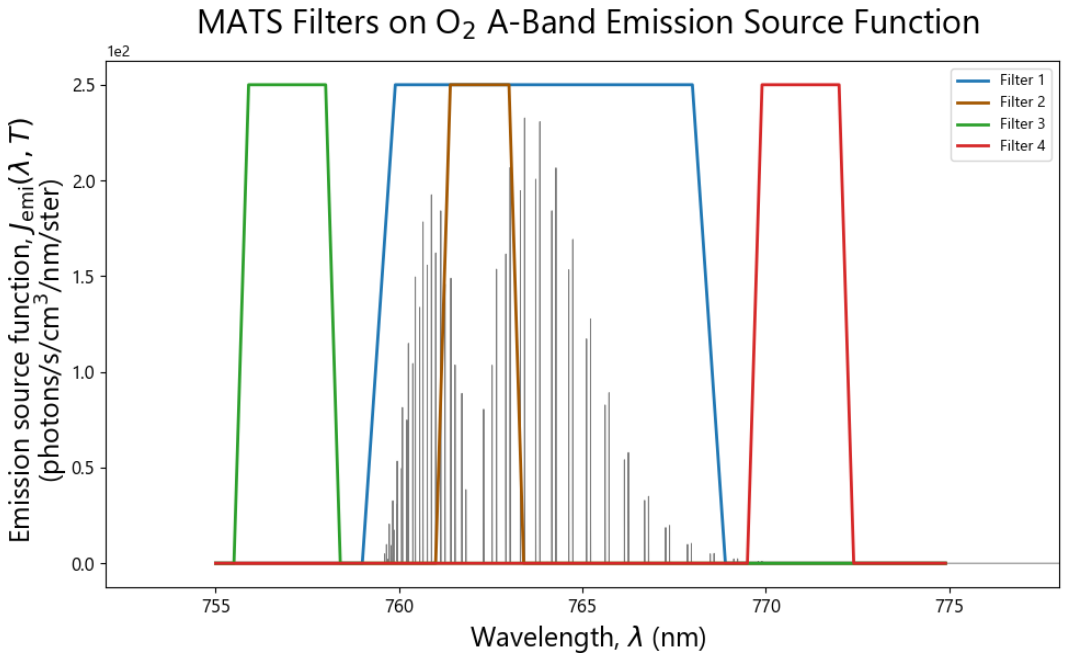

Figure 6.16: MATS spectral filters demonstrated with respect to emission source function, $J_{\text{emi}}(\lambda, T)$, from excited O_2 in the A-band.

(from 763 nm to 764 nm) with the minimum required resolution of 10^{-3} nm. Radiance spectra are calculated for tangent altitudes from 20 to 90 km in increments of 10 km, except with increasingly smaller increments surrounding the 80 km altitude in order to provide more detail around the location of the simulated PMC. These simulations are presented in two sections. Section 6.3.1 shows SASKTRAN's range in functionality and its ability to produce radiance that indicate the presence of a PMC. Section 6.3.2 provides simulated results from applying the spectral filters from Figure 6.16 to the radiance results presented in Section 6.3.1.

6.3.1 Simulated Radiance Spectra with Model PMC

Figure 6.17 shows a series of radiances with the most basic features of the original SASKTRAN model. There is no cloud entered in the model, and no emission features included. Molecular absorption is accounted for in the propagation through the atmosphere and is evident in the absorption lines, which show as sharp troughs throughout the spectra. The number of scattering orders is set to 1 to demonstrate the results of a "single scatter" radiative transfer model, only considering photons scattering once in the line of sight and

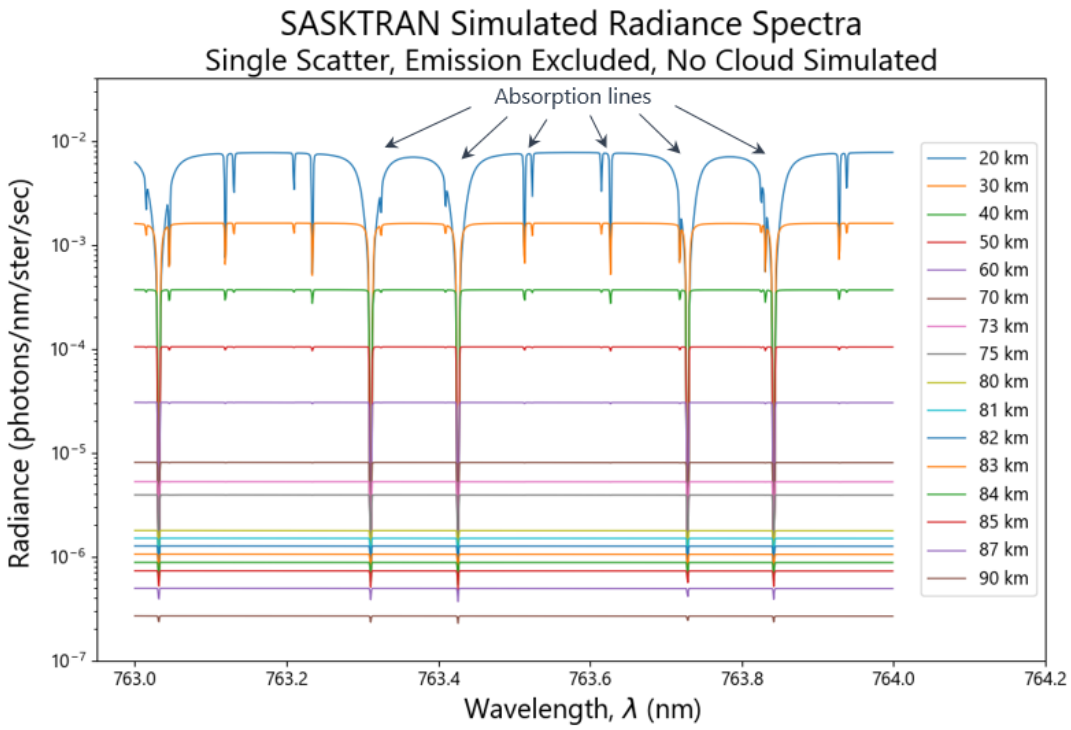

Figure 6.17: SASKTRAN simulated radiance spectra – Single-scatter radiative transfer model, photochemical emission excluded, no cloud simulated.

into the instrument. Earth's albedo is not required when employing a single scatter simulation.

Figure 6.18 shows the same series of radiance spectra with the number of scattering orders increased to 5 representing the number of times the radiative transfer equation is iterated through the atmosphere. Typically, for lower altitude simulations, the scattering order is set to 50 to represent greater optical thickness, but for the MATS area of interest in the MLT, 5 is sufficient. At this stage, Earth's albedo is required, but is set to 0 for demonstration purposes. Notice the regions in between the absorption lines at altitudes above 50 km have a slight upward curve as compared to the single scatter simulation in Figure 6.17. This background radiance is increased due to the larger number of photons scattering around in the atmosphere before entering the line of sight to be viewed by the observer. However, the effect is still slight, especially near the mesopause (above 80 km) where the air density is low, and less scattering occurs.

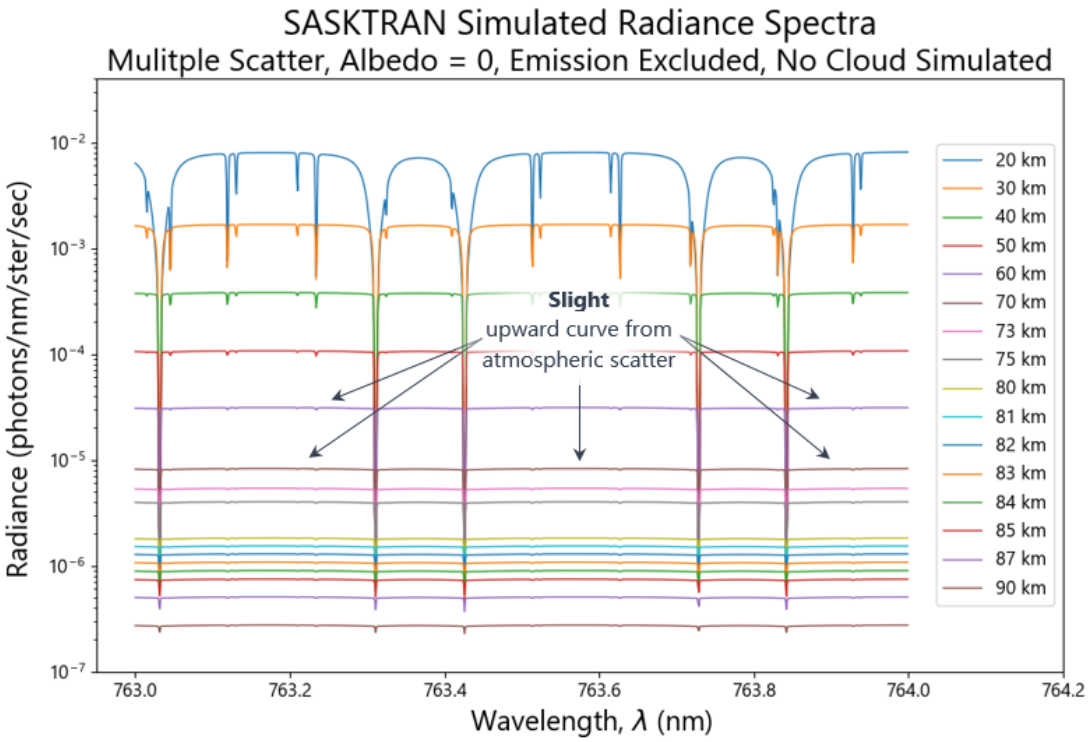

Figure 6.18: SASKTRAN simulated radiance spectra – Multiple-scatter radiative transfer model with a scattering order of 5, albedo set to 0, photochemical emission excluded, no cloud simulated.

To illustrate the importance of an albedo contribution, Figure 6.19 contains all the same properties as Figure 6.18, only with Earth's albedo set to its maximum value of 1. As a pronounced, even at high altitudes near the mesopause. This phenomenon is referred to as upwelling, from the fact that photons are seen welling up from the Earth's surface through the atmosphere to the observer.

At this stage, emission characteristics are added to the simulation, with all other parameters remaining the same. In Figure 6.20, the photochemical emission source function is included from use of the integrated SASKTRAN +A-band emission model and propagated through the multiple scattering radiative transfer model. The phenomenon is unnoticeable at the lower altitudes because absorption processes dominate at higher atmospheric densities, and emission does not become significant until above 40 km (Bucholtz et al., 1986) (Section 6.2.3 contains multiple plots demonstrating this effect).

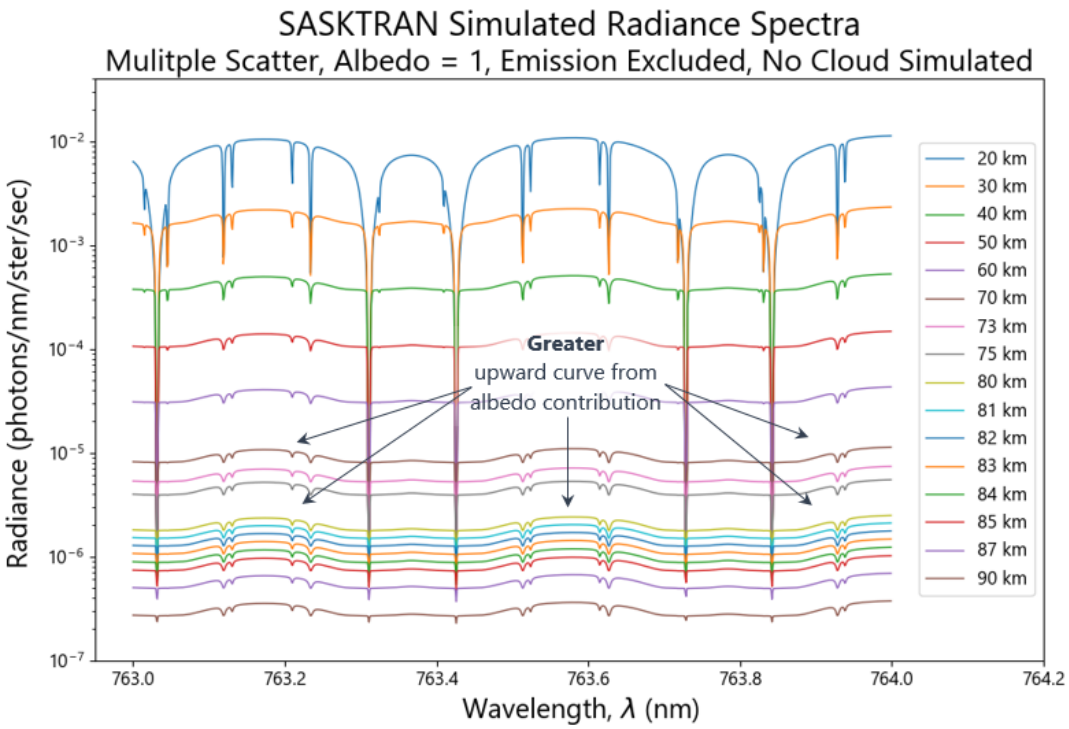

Figure 6.19: SASKTRAN simulated radiance spectra – Multiple-scatter radiative transfer model with a scattering order of 5, albedo set to 1, photochemical emission excluded, no cloud simulated.

The change becomes apparent in Figure 6.20 around 40 km altitude, significant at 50 km altitude, and dominant at 60 km and above. The PMC occurs around 82 km, at which altitude photochemical emission in the A-band cannot be neglected for accurate modeling of the radiance seen in the atmospheric limb.

Finally, Figure 6.21 illustrates the full expression of the integrated SASKTRAN +A-band emission model for the purposes of studying PMCs as is intended by the MATS mission. A PMC is added into the model atmosphere as a volume of ice particles from 81 to 83 km altitude. The radiance spectra observed from tangent altitudes near the PMC location have significant changes from Figure 6.20. In fact, the radiance measurements from 81 and 82 km are greater in magnitude than those of the lower altitudes from 73 to 80 km. This clearly demonstrates a layer of the atmosphere with increased optical thickness which contains aerosols that are reflecting stronger radiance into the line of sight. Above

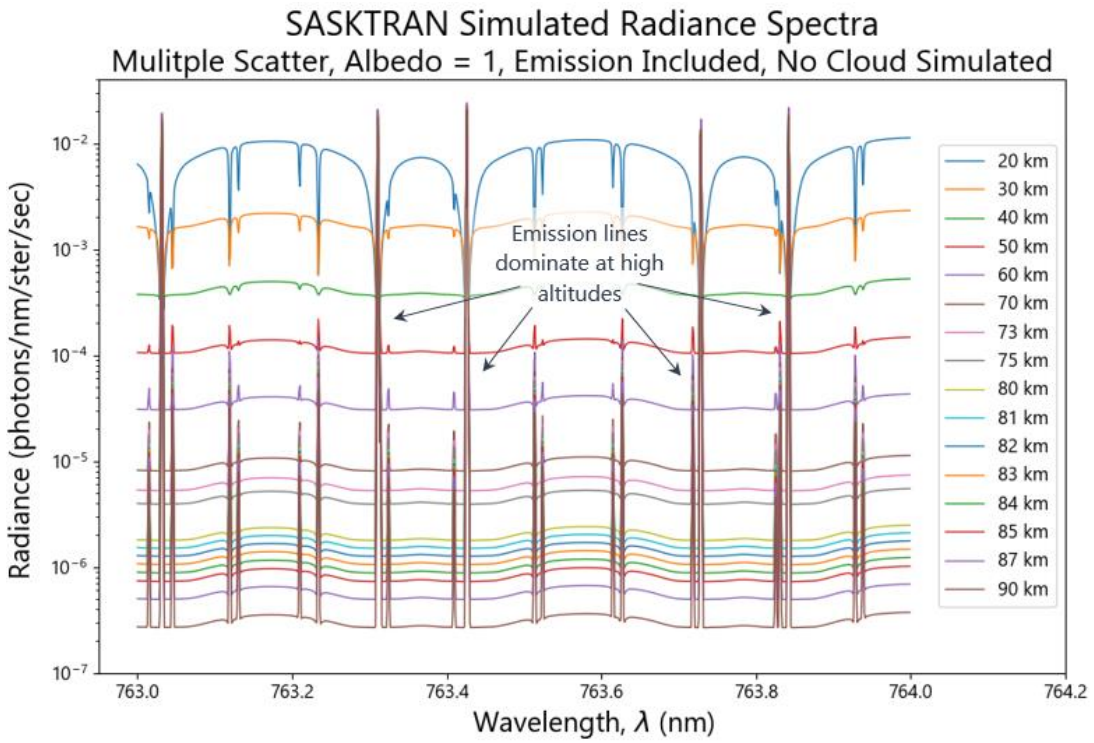

Figure 6.20: SASKTRAN simulated radiance spectra – Multiple-scatter radiative transfer model with a scattering order of 5, albedo set to 1, photochemical emission included from O_2 A-band photochemical emission model, no cloud simulated.

the cloud, the spectra observed from 84 km to 90 km remain mostly unchanged from the previous case. Therefore, Figure 6.21 fully illustrates the efficacy of the integrated SASKTRAN +A-band emission model in modelling a scattering atmosphere with both absorption and emission properties at high altitudes where PMCs produce noticeable radiance signatures.

6.3.2 MATS Measurement Simulations

The purpose of the MATS mission is to take advantage of the A-band emission spectrum's sensitivity to temperature, as discussed in Section 2.2. The effect of temperature on emission spectrum shape is difficult to detect with the naked eye, and therefore is easiest to determine via ratios rather than absolute values. Figure 6.22 shows a simulated radiance spectrum using three different temperature profiles as inputs to the integrated

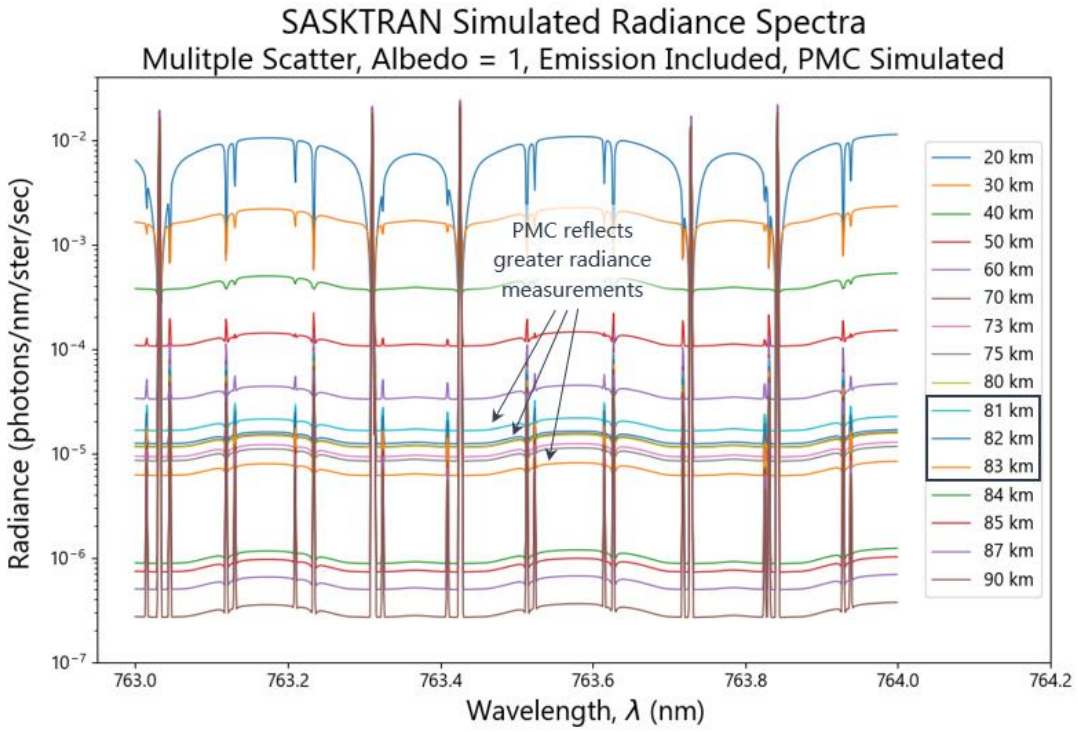

Figure 6.21: SASKTRAN simulated radiance spectra – Multiple-scatter radiative transfer model with a scattering order of 5, albedo set to 1, photochemical emission included from O_2 A-band photochemical emission model, PMC simulated between 81 km and 83 km as a collection of water ice particles.

SASKTRAN +A-band emission model, with all other inputs remaining the same as listed in Section 6.1. Each spectrum is plotted at 90 km, which is near the peak of the A-band emission profile from O_2 (Figure 3.6, Figure 4.6). The original temperature profile, T, is that shown in Figure 6.15. The entire profile is either decreased by 10 K ($T - 10\,\mathrm{K}$) or increased by 10 K ($T + 10\,\mathrm{K}$) at every altitude point to demonstrate the effects of temperature change on the emission spectrum. Figure 6.22 shows seemingly little change in the A-band emission spectrum from a significant 10 K change in temperature.

When performing a convolution to an effective spectrum resolution of 1 nm, it becomes easier to see the shape of the emission band. It is the shape and not magnitude which is most sensitive to temperature changes. Figure 6.23 shows the A-band radiance spectrum plotted at three tangent altitudes and for three different temperature inputs to

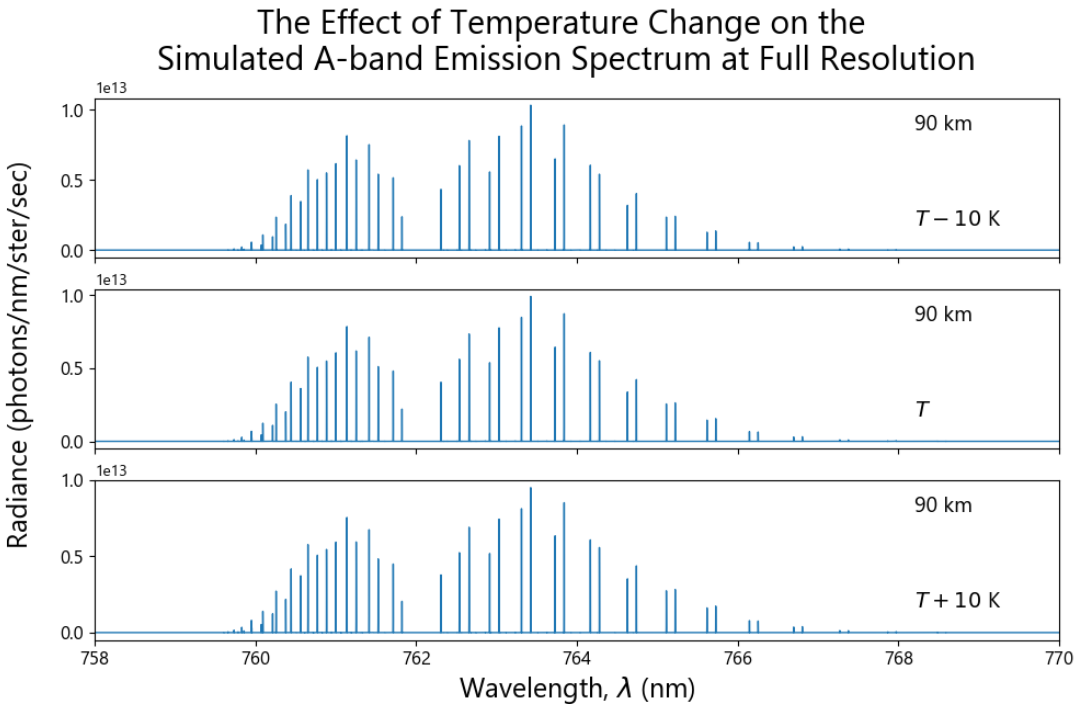

Figure 6.22: Simulated A-band emission radiance at 90 km altitude, near the peak of the A-band VER profile (Figure 4.6). The effect of a 10 K temperature change is difficult to see from full resolution emission spectrum.

demonstrate this effect more clearly. The results in Figure 6.23 are simulated without the modelled presence of the PMC, to demonstrate the effect a homogeneous MLT region will exhibit with temperature fluctuations. The effect on spectral shape is small but noticeable, especially at the highest altitude where peak A-band emission occurs. Notice the decreased temperature profile has lower values on the wings of the band, but higher values in the core, while the opposite effect occurs from the increased temperature profile. This is to be expected from the A-band emission spectrum as it responds to lower temperatures with populating the lower energy levels and experiencing energy transitions of lesser magnitude. The difference in core magnitude is not as noticeable at lower altitudes, but the wings demonstrate a similar effect with the temperature change.

The simulations in Figure 6.23 are produced again, this time in the existence of a PMC modelled as a cloud of ice particles between 81 km and 83 km (Figure 6.24). The high altitude spectra are unaffected by the addition, but the signals at 82 km within the PMC

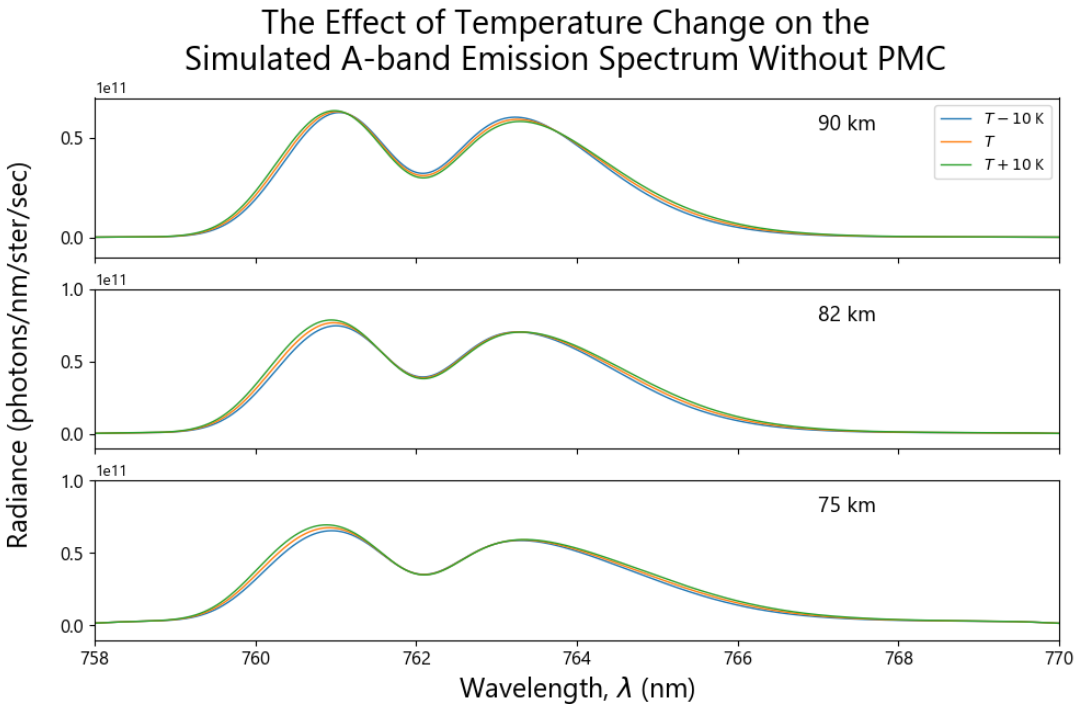

Figure 6.23: Simulated A-band emission radiance in atmosphere with no PMC at effective 1 nm resolution to demonstrate the effect of temperature change on spectral shape. Lower temperatures produce higher core values and lower wing values. Higher temperatures provide the opposite effect.

exhibit larger magnitude overall and a slightly different shape from the background radiance on either end of the A-band. The spectra at 75 km display similar behaviour as in the 82 km spectra, but with a less pronounced effect. The effect of temperature change at each altitude is still the same as when modelled without a PMC in Figure 6.23.

The MATS filters illustrated in Figure 6.16 may now be applied to the radiance spectra produced at each altitude for each temperature input. Figure 6.25 demonstrates the use of these filters on the full resolution spectra corresponding to those shown in Figure 2.4. Recall that Filter 1 measures radiance integrated across the entire A-band, and Filter 2 measures radiance from the core. The background Filters 3 and 4 are meant to measure background radiance outside the A-band spectrum and are not fully included in these simulations. These filters will be used on the MATS instrument to measure background radiance in the atmosphere in order to remove its contribution to the desired A-band

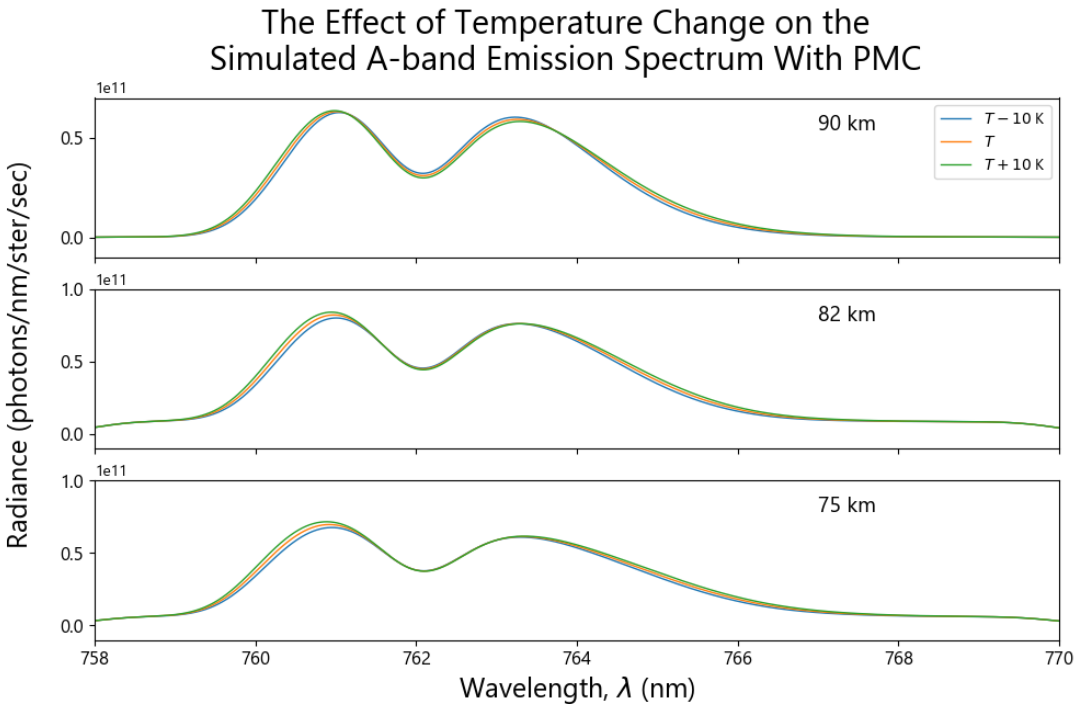

Figure 6.24: Simulated A-band emission radiance at effective 1 nm resolution with modelled PMC between 81 km and 83 km altitude. Background radiance is greater at 82 km and 75 km due to more scattered light, but temperature effect remains the same as in Figure 6.23.

emission. However, with use of the full resolution SASKTRAN +A-band model, a different method is used for background radiance removal and is discussed further below.

Background radiance removal is achieved by establishing a baseline using linear fit on the edges of the spectrum. Figures 6.26 and 6.27 illustrate the placement of this baseline for one temperature at each altitude. Figure 6.26 shows the radiance spectra with no PMC, for which the baseline appears to match the background radiance in shape. Figure 6.27 shows the simulated spectra including a modelled PMC, for which the background radiance shape changes and the baseline has been chosen in the middle of the apparent curve.

Once the background radiance is removed by subtracting the baseline from Figures 6.26 and 6.27 from the band, the spectra can be filtered as indicated in Figure 6.25 to produce radiance profiles integrated across the whole band (Filter 1) and across just the core region (Filter 2). Figure 6.28 shows these radiance profiles produced both without and with a

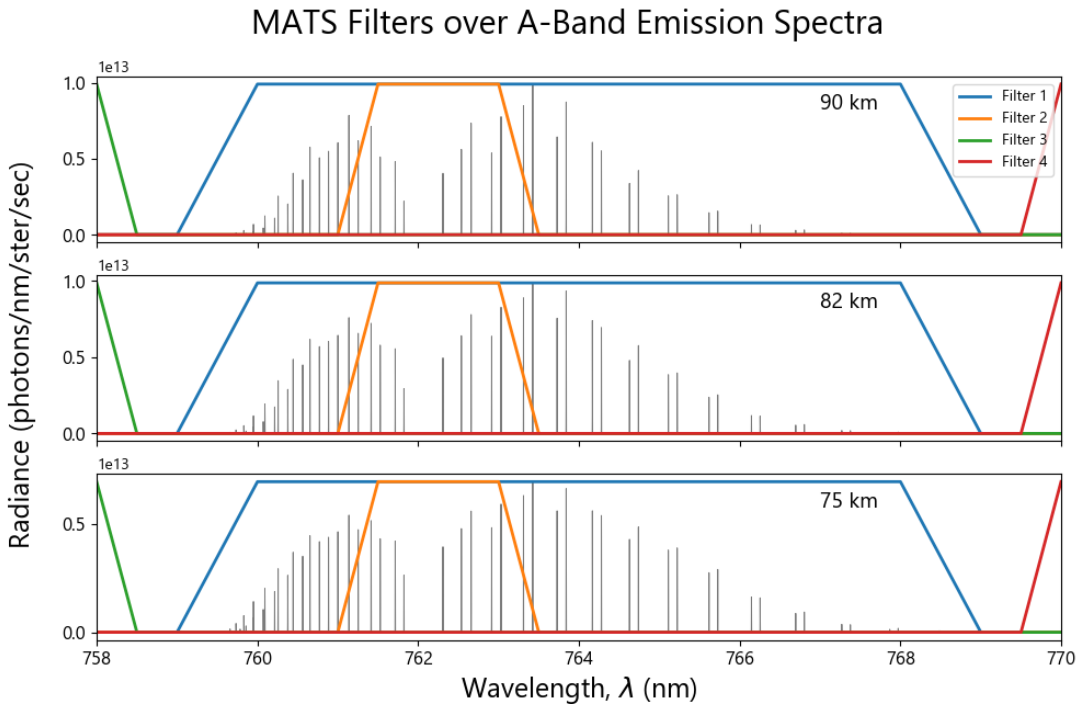

Figure 6.25: MATS filters overlaid on simulated A-band radiance spectra. Filter 1 measures radiance over the whole A-band, and Filter 2 measures radiance just in the core of the spectrum. Background Filters 3 and 4 are show for completeness but their results are not used for background radiance removal in this analysis.

PMC modelled in the atmosphere, where the dashed lines show the altitude range within which the PMC is modelled. At the lowest altitudes, between 40 km and 50 km, the core region measures greater than the full band because there is still significant absorption in the A-band. Above 50 km, the emission dominates, and the filtered band radiance is greater. Both profiles show a peak between 85 km and 90 km, which is the peak of the A-band VER profiles (Figure 4.6). A small difference is seen in the profiles with the PMC modelled due to the imperfect background light removal. With more in depth analysis, there will be no PMC effect shown. These profiles are only shown with the original temperature profile input for demonstration purposes, so there is no effect of temperature change demonstrated.

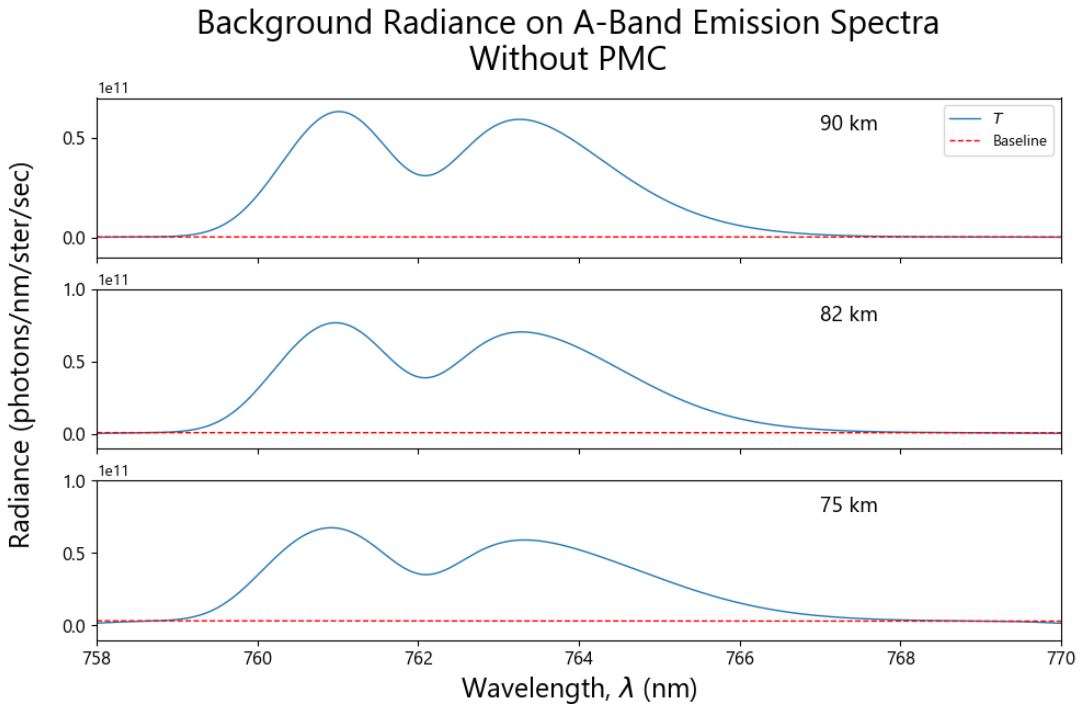

Figure 6.26: Baseline established for background radiance removal of emission spectrum. Without a PMC in the atmosphere, the background radiance is essentially linear and mostly matches the shape of the baseline.

The core-to-band is defined as the ratio between measurements from Filter 2 and Filter 1 at each altitude. As is expected from Figures 6.23 and 6.24, the core-to-band ratio is higher at lower temperatures and lower at higher temperatures. Figure 6.29 plots the ratio as a profile above 60 km to exclude signals where absorption still dominates. The core-to-band ratios still exhibit a similar effect as is shown in Figure 6.28 near the modelled PMC. Figure 6.28 suggests more detailed background removal techniques are required for proper results, further confirming the necessity of SASKTRAN's ability to accurately model scattering in the MLT.

From the core-to-band ratios in Figure 6.29, it is demonstrated that the temperature in the MLT region of the atmosphere can be found by measuring two separate bandwidths in the A-band emission spectrum as a function of altitude. The ratio of these measurements

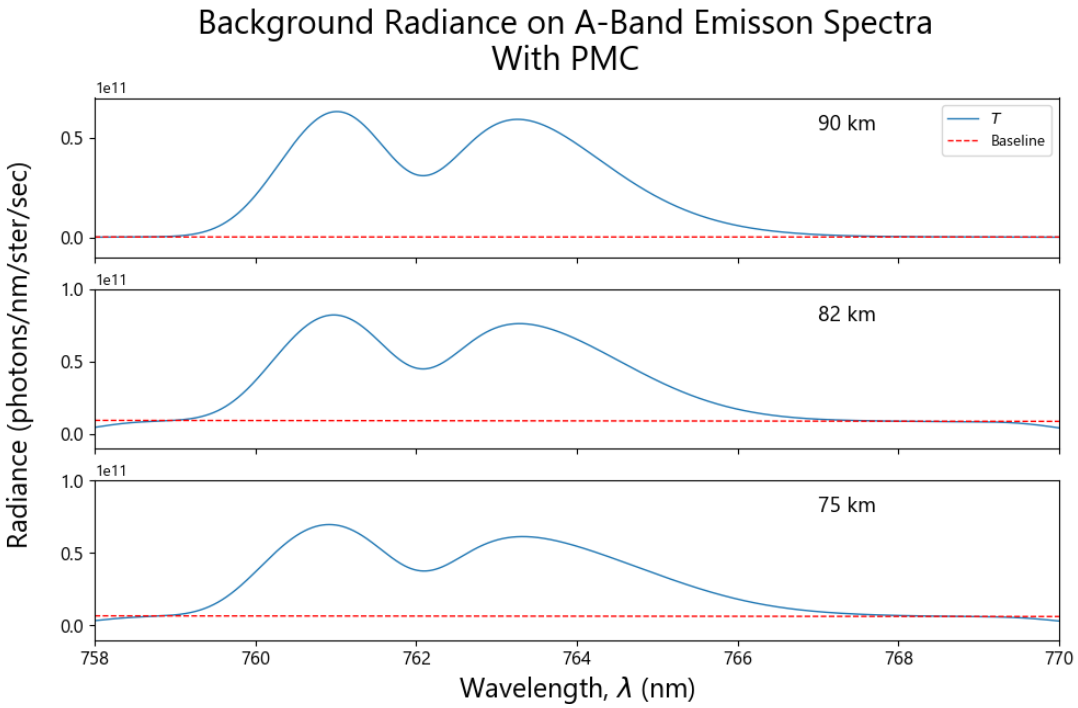

Figure 6.27: Baseline established for background radiance removal of emission spectrum. With a modelled PMC between 81 km and 83 km, the background radiance has an upward curve and the baseline is adjusted accordingly.

at each altitude provides enough information to inverse the forward model presented in this thesis and determine the original temperature at that altitude through retrieval processes. The ability of the integrated SASKTRAN +A-band emission model to create an atmosphere with absorption, scattering, and photon emission properties is therefore integral to the accurate retrieval of mesospheric temperatures in relation to the O_2 A-band emission spectrum.

6.4 Chapter Summary

The newly designed integrated SASKTRAN +A-band emission model is capable of modelling light propagation through an atmosphere including phenomena of molecular absorption, multiple scattering, and photochemical emission. Because the original SASKTRAN model was constructed in support of the OSIRIS mission (Section 2.3), verification of the SASKTRAN +A-band model can be performed by comparing simulated

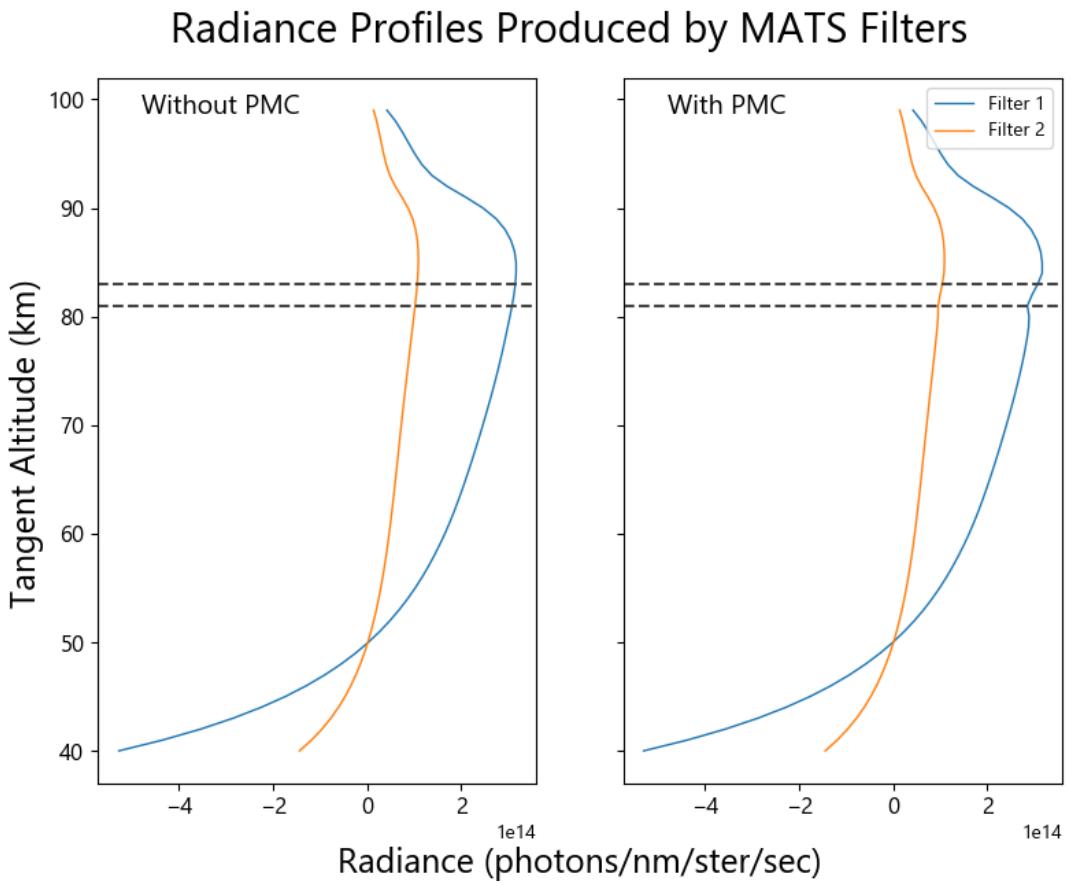

Figure 6.28: Radiance profiles from O_2 A-band emission in the MLT region. Each profile is a result of filtering the full spectral bands simulated by the integrated SASKTRAN +A-band emission model. Filter 1 integrates across the entire A-band, and Filter 2 integrates the core region. The dashed lines show the placement of the modelled PMC in the plot on the right.

radiance spectra with actual OSIRIS measurements in the atmospheric limb. A specific OSIRIS scan was chosen for comparison because it has been previously used for verification and contains altitudes high enough to illustrate the A-band emission feature. Section 6.1 discusses the specific user inputs to the SASKTRAN +A-band model designed to match the viewing geometry and atmospheric state experienced by OSIRIS during this scan. Calculation parameters are chosen to optimize for model accuracy and efficiency. All inputs and their sources are listed in Table 6.1.

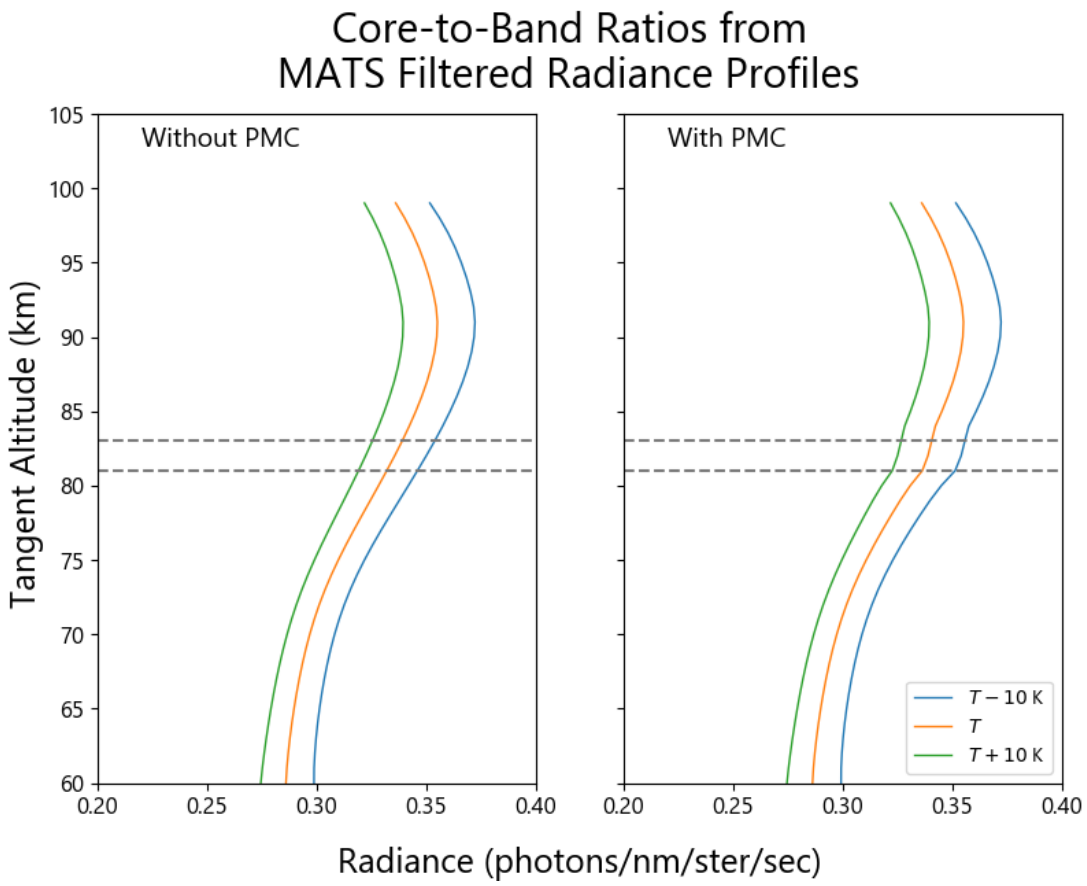

Figure 6.29: Core-to-band ratios for three different temperature profile inputs, modelled in the MLT both without and with a PMC between 81 km and 83 km.

OSIRIS measurements are shown in Figures 6.3 and 6.4, where the A-band emission feature begins to contribute above 40 km altitude and is dominant above 50 km. All SASKTRAN simulations are run at the full resolution of 10^{-3} nm but the signals are convolved to an effective 1 nm resolution for comparison with the OSIRIS measurements. Simulations from the original SASKTRAN model at full resolution show the absorption lines and scattering features seen at lower altitudes, but do not exhibit any emission features above 40 km (Figure 6.7). The same simulations from the SASKTRAN +A-band model provide clear emission features above 40 km (Figure 6.10). Figure 6.14 shows the final comparison between the original SASKTRAN model, the integrated SASKTRAN +A-band model, and the OSIRIS measurements, once corrected for a –0.25 nm wavelength bias and a vertical offset due to stray light in the instrument system. There is clear agreement between all three signals at the 9 km and 25 km altitudes, but above 40 km,

the simulated radiance spectra from the original SASKTRAN model begins to diverge with too much absorption contribution. Meanwhile, the SASKTRAN +A-band model produces simulations that follow the OSIRIS measurement closely enough to provide verification of the accuracy of the new model.

The MATS mission intends to take radiance measurements near and within PMCs in the MLT. Section 6.3.1 demonstrates step-by-step the functionality of the integrated SASKTRAN +A-band emission model in simulating radiance spectra at the desired altitudes with all the expected phenomena in relation to the MATS project. The full expression of the model is displayed with Figure 6.21, including absorption, multiple scatter from the atmosphere and ground, photochemical emission, and a modelled PMC. Section 6.3.2 provides simulated instrument measurements by exploring the effect of temperature variation on the A-band spectral shape. A core-to-band ratio is calculated from integrating over the filters shown in Figure 6.25. The core-to-band ratio is inversely proportional to temperature (Section 2.2). Figure 6.29 shows core-to-band ratio profiles for three different temperature profiles, demonstrating a very visible effect of A-band spectral shape with respect to temperature. With these preliminary demonstrations, the SASKTRAN +A-band emission model is shown to have considerable value in processing measurements taken of the O_2 A-band emission feature in the MLT region.

Chapter 7

Conclusion and Future Work

Remote sensing of the atmosphere has long been used to provide insight to its phenomena and how the dynamic processes affect Earth's climate. The two lowest layers of the atmosphere are the troposphere and stratosphere, which contain Earth's weather and ozone layer. The boundary region between these two layers, the UTLS, is the subject of much study because of its significant contribution to global climate. The region above the stratosphere is the mesosphere and lower thermosphere (MLT) and is less understood than the lower layers. The higher altitudes (above 50 km) are more difficult to observe, and the atmosphere is more stable due to low pressure and generally thought less likely to contribute to climatic trends over short periods of time. However, recent research has shown that certain phenomena like PMCs and gravity waves in this region are strong indicators of atmospheric processes originating at lower altitudes. Atmospheric air glow occurs in the MLT where molecules have enough time between collisions to experience spontaneous emission and is an easily measurable feature. Because the air glow depends on atmospheric parameters like species density and temperature, measurements of photochemical emission in the MLT can be used to study other mesospheric phenomena and develop more global atmospheric models which transcend typical static boundary layers.

The OSIRIS instrument (background in Section 2.3.1) was launched in 2001 and takes measurements of scattered sunlight in the atmospheric limb. Measurements taken above 50 km demonstrate some of the strong emission features in the atmospheric air glow (Figure 2.13). The original SASKTRAN radiative transfer model (background in Section

2.3.2) is an atmospheric framework that runs the forward radiative transfer model to simulate radiance spectra for comparison with OSIRIS measurements. The typical focus of study with the SASKTRAN model has been the UTLS, so it is capable of accurately modelling an atmosphere with molecular absorption and multiple scattering features, but not photochemical emission. The MATS mission (background in Section 2.3.3) aims to perform measurements in the UV and NIR to study PMC structure for research on gravity waves in the MLT. There are simple radiative transfer models that can simulate photochemical emission for research in the mesosphere, but do not include absorption or multiple scattering to the scale implemented in SASKTRAN. The study of aerosol particles in a region of the atmosphere where photochemical emissions are dominant requires a forward model capable of simulating molecular absorption, multiple scattering, and photochemical emission in a continuous vertical profile. This thesis presents the integrated SASKTRAN +A-band emission model, wherein photochemical emission has been added as an additional source term to the radiative transfer equation used by the original SASKTRAN model in preparation for use with the MATS project and to support broader applications in the future.

One of the brightest emission features in the MLT is the O_2 A-band emission (Section 3.1), occurring around 762 nm in the NIR. The shape of the emission spectrum is dependent on temperature, making this a valuable feature for MATS to measure in the MLT. The feature occurs from the O_2 molecule becoming excited to the A-band level, creating the excited O_2^A molecule, and spontaneously emitting in the A-band frequency. The volume emission rate (VER) is directly proportional to the density of O_2^A throughout the atmosphere. In order for temperature to be inferred from A-band radiance measurements, a forward model is derived that can accurately simulate the observed spectra from initial atmospheric state. The combined O_2 A-band photochemical emission model is described in Chapters 3 and 4 and can produce a spectral photochemical source function as a function of altitude for propagation through the radiative transfer equation

used in the original SASTRAN radiative transfer model. Integration and implementation of all models is discussed in Chapter 5.

Chapter 3 provides the full photochemical model required to determine the density profile of O_2^A given an initial atmospheric state. Using steady state analysis, O_2^A density is modeled as a ratio between its productions and losses (Section 3.2). There are four separate production mechanisms (Section 3.3) and two loss mechanisms (Section 3.4). Section 3.5 provides a model summary, which requires inputs of density profiles for ground state O_2, O_3, N_2, and O, as well as temperature profiles. The result is a spectrally averaged density profile of O_2^A (Figure 3.6). All reaction rates and coefficients are listed and referenced in Table 3.3.

Chapter 4 describes the spectroscopy and radiative transfer theory necessary to derive the photochemical emission source function from the O_2^A density profile. Spectroscopic line strengths are broadened according to the characteristics of their environment (Sections 4.1 and 4.2), from which absorption cross-sections (Section 4.3.1) and emission functions (Section 4.5) are determined. Attenuated solar flux is calculated due to the Beer-Lambert law and used to produce the altitude-dependent photochemical reaction rates required in the photochemical model (Section 4.3). A spectrally averaged VER (Figure 4.6) is found using the O_2^A density profile from the photochemical model, from which wavenumber dependent VER spectra are derived by applying the normalized emission weighting function (Section 4.6, Figure 4.7). The final result of the emission model is a radiative source function due to photochemical emission which contains an emission spectrum for each altitude (Section 4.7).

Chapter 5 presents the software implementation of each of the two preceding models, and the method of integration with the original SASKTRAN radiative transfer model to create the integrated SASKTRAN +A-band emission model. Figure 5.1 provides a diagrammatic description of the implementation of the three submodels, with inputs and results clearly labeled. Sources for static data inputs are stated here where applicable, such

as wavenumber resolution, spectroscopic data, and quantum yields. Details on initialization and operation of the SASKTRAN model are handled here as well (Section 5.2, Section 5.6.2) to provide comprehensive instruction on running the complete SASKTRAN +A-band model.

Chapter 6 provides verification of the model and applications with respect to the MATS project. Because the original SASKTRAN model was designed in support of the OSIRIS mission, verification of the SASKTRAN +A-band model is performed by comparing simulated radiance spectra with actual OSIRIS measurements in the atmospheric limb. The OSIRIS scan chosen for comparison has been used in previous studies for verification and contains altitudes high enough to illustrate the A-band emission feature. User-defined inputs are discussed in Section 6.1 and listed in Table 6.1. The required inputs include time, observer position and orientation, background altitude profile, atmospheric data (temperature, pressure, density for air, O_2, N_2, O, aerosol, and O_3), albedo, scattering order, and calculated wavelengths. Time and position inputs are designed to match that of the OSIRIS instrument during the scan used and correspond to April 24, 2002 at 82°N and 41°E. Atmospheric data is obtained from the MSIS-E-90 model or from SASKTRAN/OSIRIS retrievals (Figures 6.1 and 6.2). All profiles must have data up to 200 km or above for accurate modelling of attenuated solar flux through the top of the atmosphere.

Figure 6.13 shows the high-resolution simulations from both the original SASKTRAN model and the SASKTRAN +A-band model. The outputs are also shown on a 1 nm scale to give an impression of the shape of the spectra. Above 40 km, the +A-band model exhibits some emission contribution, while the original model is still only displaying absorption. The effect is most apparent at the highest altitude of 69 km, where the A-band emission spectrum is clearly simulated by the integrated model and no emission at all is shown by the original model. Figure 6.14 compares these results to OSIRIS measurements from the relevant scan. After some instrument corrections, the SASKTRAN

+A-band model spectra match the emission feature seen by OSIRIS at high altitudes, verifying the validity of the updated model.

Section 6.3 demonstrates the full functionality of the SASKTRAN +A-band model with respect to the MATS mission. In Section 6.3.1, full resolution radiance spectra are simulated for 2 nm within the A-band with different features of the SASKTRAN model illustrated. Figure 6.17 shows results that would be seen from a simple radiative transfer model with no clouds in the atmosphere and no photochemical emission. Only absorption lines are prevalent. Figure 6.18 shows the effects of enabling multiple scatter with a scattering order of 5, but with no effects from albedo, while Figure 6.19 increases albedo. Photochemical emission is added to the model in Figure 6.20, demonstrating the full expression of the SASKTRAN +A-band model. Finally, a PMC is added to the model atmosphere as a collection of ice particles around 82 km (Figure 6.21). With this series of figures, it is clear that the radiance spectra simulated through the atmospheric limb changes radically with added layers of functionality. This demonstrates that none of the modelled processes are negligible when studying PMCs in the MLT, thus confirming the necessity of the integrated SASKTRAN +A-band emission model presented in this thesis.

The A-band work as it relates to the MATS mission depends on the variability of the emission spectrum with respect to temperature. This relationship is introduced in Section 2.2 and revisited in Section 6.3.2. The MATS instrument is designed to filter the A-band emission as shown in Figure 6.16, with Filter 1 covering the whole band, and Filter 2 only measuring the core (Filters 3 and 4 are for background measurement). Figure 6.24 shows the difference in modelled emission spectra from SASKTRAN +A-band at three altitudes and for three different temperature profiles with a PMC included around 82 km. With increased temperature, the core values decrease and the values on the edges of the band increase. The opposite occurs with a decreased temperature. Figure 6.27 presents the filtered results of the A-band that would be observed from MATS Filters 1 and 2 for one input temperature profile. The core-to-band ratio is calculated as a simple indicator of

temperature change and plotted as a profile in Figure 6.29. This result confirms that the MATS design of measuring A-band emission with two simple filters and plotting the ratio will provide valuable temperature information in the MLT. As well, Figure 6.29 further verifies the utility of the SASKTRAN +A-band model as a comprehensive tool in studying complex atmospheric processes in the mesosphere where molecule absorption, multiple scattering, and photochemical emission are all observed.

This thesis serves to provide the relevant theory and methodology required to programmatically implement the full O_2 A-band photochemical emission model (Chapters 3 and 4), as well as instruction on how to integrate its results into the standard radiative transfer equation for use in the original SASKTRAN radiative transfer model (Chapter 5). The focus of this thesis is on proper design, and verification of the model (Section 6.2). Applications shown in Section 6.3 are purely for demonstration purposes and suggest areas for future work. The MATS mission is still in production with a planned launch in the coming few years. The SASKTRAN +A-band model may be used for more in-depth measurement simulations to gauge the true temperature sensitivity of the A-band spectrum and to aid in instrument design. Retrieval methods may also be explored for use with this forward model in order to obtain temperature retrievals from simulated MATS measurements. All future processing work for the MATS mission with respect to the A-band both before and after launch are made possible with the design and integration present in this work.

Although the primary motivation for the design of the SASKTRAN +A-band model is for support of the MATS project, this fully integrated model now contains more comprehensive functionality in modelling the atmosphere at higher altitudes. There are other fields of research which will benefit from the ability to model a more complete atmosphere. Many CO_2 retrievals made from nadir measurements assume negligible A-band emission contributions in their column calculations but do look through the portion of the atmosphere in which emission is dominant. Using the SASKTRAN +A-band model

with nadir geometry allows confirmation of the validity of neglecting A-band emission in the CO_2 retrieval method for many studies. This is just one example of the many ways in which the SASKTRAN +A-band model can be more broadly applied. By including emission characteristics typical of higher altitudes in an existing model capable of accurately simulating a lower altitude atmosphere with absorption and multiple scattering, this work helps to bridge the gap in traditional radiative transfer models and promote greater understanding of atmospheric processes on a global scale.

Appendix

SASKTRAN +A-Band Model Implementation Technical Details

Chapter 5 contains an overview of how to implement the integrated SASKTRAN +A-band emission model programmatically. Further technical details regarding implementation are contained in this appendix.

A.1 SASKTRAN Atmosphere

Each atmospheric constituent in SASKTRAN is represented by two things:

1) A climatology that specifies the amount and distribution of the constituent.
2) An optical property that defines the species' absorption/scattering cross-section.

These two elements are combined together to define each species. Each desired species is created and added to the atmosphere as required. Many precomputed climatologies and optical properties are available, or they can be user-defined. The climatology that contains temperature and pressure profiles, along with the general air density, is referred to as the background atmospheric state. The background state is set up first along with the user-defined altitude array and its profiles are used when calculating cross-sections of the subsequently added species (ARG, 2018).

The relevant scattering and absorption properties in the atmosphere are implemented by adding additional atmospheric constituents on top of the background atmosphere. For the SASKTRAN radiative transfer model portion of the integrated model, only ozone (O_3), molecular oxygen (O_2), and aerosol densities are required. The albedo of the Earth is then

entered as a bidirectional reflectance distribution function (BRDF). A BRDF is defined as the ratio of the radiance scattered from a surface into a given direction to the collimated power incident on a unit area of the surface. Setting the SASKTRAN BRDF object to a single value between 0 and 1 indicates a Lambertian surface, which is an appropriate approximation for Earth's albedo in these simulations (ARG, 2018).

A.2 Solar Zenith Angle from SASKTRAN Sun Position

The SASKTRAN sun position, $\hat{S}$, is calculated as a unit vector in geodetic coordinates originating from the centre of the Earth,

$$\hat{S} = \left(S_x, S_y, S_z\right) , \tag{A.1}$$

where the z-axis points from the centre of the Earth to the North Pole, the x-axis is directed towards the prime meridian at the equator, and the y-axis completes the orthogonal system. The solar zenith angle, χ, can be calculated from the sun position vector and from the local "up" vector, $\hat{z}$, also in geodetic coordinates, as:

$$\chi = \arccos\left(\hat{S} \cdot \hat{z}\right) \tag{A.2}$$

Figure A.1 demonstrates the orientation of the sun position unit vector, and local "up" vector with respect to the observer's location on the Earth.

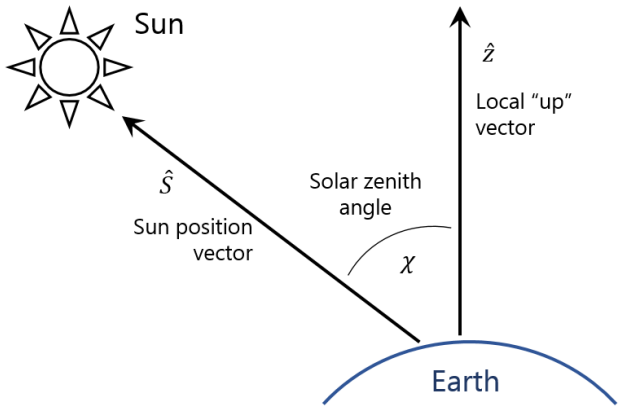

Figure A.1: Solar zenith angle found from SASKTRAN's calculated sun position vector and the local "up" vector, both in geodetic coordinates.

A.3 Emission Model (B) External Inputs

A.3.1 Spectroscopic Data

All spectroscopic data for Submodel B is obtained from the HITRAN (High-resolution TRANsmission) database, a line-by-line compilation of spectroscopic parameters measured at a standard temperature $T_s = 296\ \mathrm{K}$ (Rothman et al., 1996). Table A.1 lists all data values and their corresponding variables that are obtained from the HITRAN database for both the A and B-bands in the ranges listed in Table 5.1. Spectroscopic data from HITRAN is not required for the Lyman-α line, Schumann-Runge continuum (SRC), or the Hartley bands.

Table A.1: Spectroscopic data required from the HITRAN database.

Description	Variable	Units
Transition wavenumber	ν_j	cm^{-1}
Line strength at standard temperature (Line intensity)	$S_j(T_s)$	$cm^{-1}/molec/cm^{-2}$
Lower state energy value	$E''_{0,j}$	cm^{-1}

A.3.2 Absorption Cross-Sections in Lyman-α, SRC, and Hartley Bands

The absorption cross-section value for O_2 in the Lyman-α line at 121.6 nm, $\sigma^{\mathrm{L}}_{\mathrm{O}_2}$, was taken from Reddmann and Uhl (2003). O_2 absorption cross-section values in the SRC, $\sigma^{\mathrm{S}}_{\mathrm{O}_2}(\nu)$, are from Yoshino et al. (2004) for 1 nm intervals from 130 to 175 nm. O_3 absorption cross-sections in the Hartley bands, $\sigma^{\mathrm{H}}_{\mathrm{O}_3}(\nu)$, come from Daumont et al. (1992), Brion et al (1993), and Malicet et al (1995). These cross-sections are not temperature dependent, and therefore altitude invariant.

A.3.3 Incident Solar Flux Data

The attenuated flux, $F(\lambda, z)$, must be calculated in all five of the spectral regions listed in Table 5.1, requiring data for incident solar flux, $F(\lambda, z_\infty)$, to be collected in the same five regions. Following the method outlined in the dissertation by Sheese (2009), this data is

acquired from NASA's Solar Radiation and Climate Experiment (SORCE). Measurements of solar flux incident on Earth's atmosphere are published as a time series on the NASA website, lasp.colorado.edu/sorce/index.htm. Daily average values are acquired from the SOLSTICE (Solar Stellar Irradiance Comparison Experiment) instrument measurements in the far ultraviolet (FUV) region from 115 to 180 nm and the middle ultraviolet (MUV) region from 180 to 310 nm to provide data for the Lyman-α line, the SRC, and the Hartley bands. Measurements from SOLSTICE were taken at 1 nm intervals on the integer value of wavelength. A and B-band values were obtained from measurements taken with the SIM (Spectral Irradiance Monitor) instrument, with a spectral resolution of 2.5 nm. These measurements do not occur at integer values of wavelength, and therefore make it difficult to correlate with other spectral data. As a result, only one daily measurement of solar irradiance is used per band (A-band measurement near 762 nm, B band measurement near 688 nm) and treated as a spectral average (Sheese, 2009).

A.3.4 Quantum Yields

The quantum yield of O_2 photodissociation at the Lyman-α line, ϕ_L, has an average value of 0.48 (Lacoursiere et al., 1999). The spectral average quantum yield of O_2 across the SRC, ϕ_S, is 1.0 (Brasseur and Solomon, 2005). Quantum yield values for O_3 in the Hartley bands, $\phi_H(\lambda)$, are obtained from Nishida et al. (2004) for 1 nm intervals between 198 and 229 nm, from Takahashi et al. (2002) for 1 nm intervals between 230 and 288 nm, and from Talukdar et al. (1998) for 1 nm intervals between 289 and 309 nm.

A.4 Emission Model (B) Implementation

A.4.1 Attenuated Solar Flux

A unit conversion is required between the incident flux data gathered from the SORCE project and the data input into the attenuated flux equation (Equation 5.4). Converting from units of $W/m^2/nm$ to photons/s/cm^2/nm is performed with the formula

$$F_{\text{photons}}(\lambda, \infty) = F_{\text{Watts}}(\lambda, \infty)\left(\frac{\lambda_{\text{nm}}}{hc}\right)10^{-13} \ . \tag{A.3}$$

Incident solar flux in the SRC and Hartley bands in terms of photons/s/cm^2/nm is shown in Figure A.2.

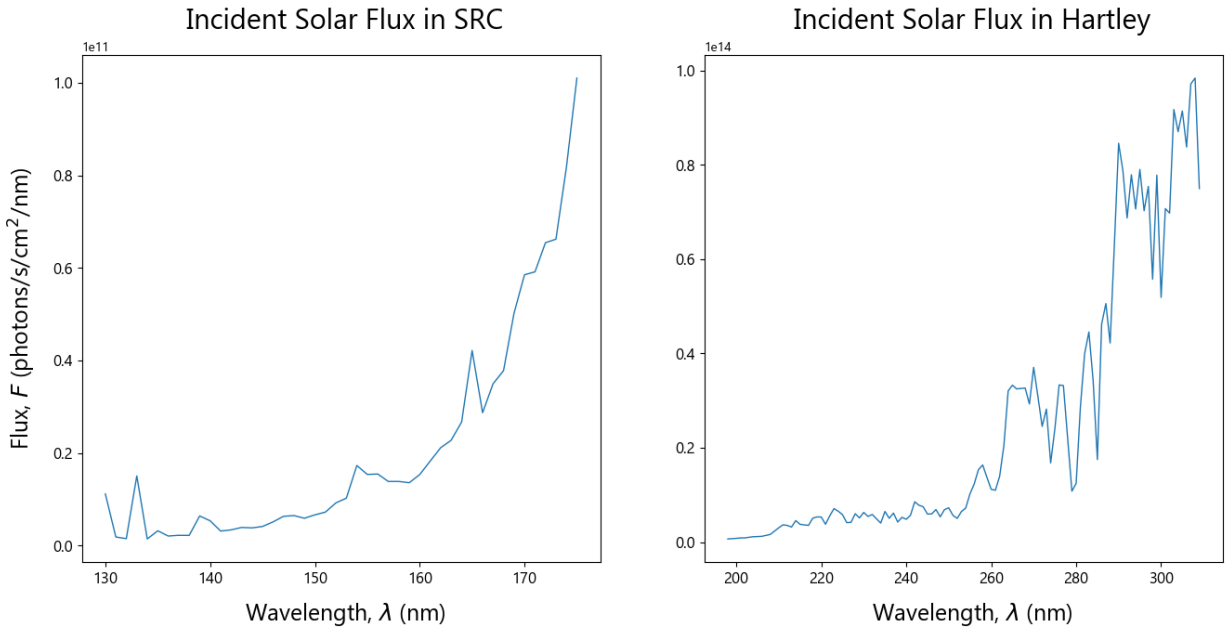

Figure A.2: Incident solar flux values in the SRC and the Hartley bands in terms of photon count from SORCE data.

Absorption cross-section data is required for each of the five spectral regions to calculate attenuation. Note that cross-sections of O_2 in the A and B-bands depend on wavenumber, ν (cm^{-1}), while externally sourced cross-section data for O_2 and O_3 in the Lyman-α line, SRC, and Hartley bands is in terms of wavelength, λ (nm). The five regions can be expressed explicitly in the flux calculations, wherein attenuated solar flux for the A and B-band regions depend on wavenumber, and attenuated flux for Lyman-α, SRC, and Hartley band regions depend on wavelength.

$$F_{\mathrm{A}}(\nu, z) = F_{\mathrm{A}}(z_\infty) \exp\left(-\sec\chi \int_z^{z_\infty} [\mathrm{O}_2] \sigma_{\mathrm{O}_2}^{\mathrm{A}}(\nu, z)\, dz' \right) \tag{A.4}$$

$$F_{\mathrm{B}}(\nu, z) = F_{\mathrm{B}}(z_\infty) \exp\left(-\sec\chi \int_z^{z_\infty} [\mathrm{O}_2] \sigma_{\mathrm{O}_2}^{\mathrm{B}}(\nu, z)\, dz' \right) \tag{A.5}$$

$$F_{\mathrm{L}}(z) = F_{\mathrm{L}}(z_\infty) \exp\left(-\sec\chi \int_z^{z_\infty} [\mathrm{O}_2] \sigma_{\mathrm{O}_2}^{\mathrm{L}}\, dz' \right) \tag{A.6}$$

$$F_{\mathrm{S}}(\lambda, z) = F_{\mathrm{S}}(\lambda, z_\infty) \exp\left(-\sec\chi \int_z^{z_\infty} [\mathrm{O}_2] \sigma_{\mathrm{O}_2}^{\mathrm{S}}(\lambda)\, dz' \right) \tag{A.7}$$

$$F_{\mathrm{H}}(\lambda, z) = F_{\mathrm{H}}(\lambda, z_\infty) \exp\left(-\sec\chi \int_z^{z_\infty} [\mathrm{O}_3] \sigma_{\mathrm{O}_3}^{\mathrm{H}}(\lambda)\, dz' \right) \tag{A.8}$$

Note that variable expressions for $F_{\mathrm{A}}(z_\infty)$, $F_{\mathrm{B}}(z_\infty)$, $F_{\mathrm{L}}(z)$, $F_{\mathrm{L}}(z_\infty)$, and $\sigma_{\mathrm{O}_2}^{\mathrm{L}}$ do not express spectral dependence because they are single values with respect to spectrum.

The attenuated flux for A and B-bands in Equations A.4 and A.5 require incident solar flux values $F_{\mathrm{A}}(z_\infty)$ and $F_{\mathrm{B}}(z_\infty)$ in terms of wavenumber instead of wavelength. The data acquired from SORCE is wavelength dependent, and so requires conversion. Because of inverse proportionality between wavenumber and wavelength, the full differential derivation is required in order to obtain a unit conversion formula:

$$F(\nu, \infty)\, d\nu = F(\lambda, \infty)\, d\lambda$$

$$F(\nu, \infty) \left| \frac{d\nu}{d\lambda} \right| = F(\nu, \infty) \left| \frac{d}{d\lambda}\left(\frac{1}{\lambda}\right) \right| = F(\nu, \infty) \left(\frac{1}{\lambda^2}\right) = F(\lambda, \infty)$$

$$F(\nu_{\mathrm{cm^{-1}}}, \infty) = F(\lambda_{\mathrm{nm}}, \infty)\, \lambda_{\mathrm{nm}}^2 \left(10_{\mathrm{cm/nm}}^{-7}\right) \tag{A.9}$$

Here it is assumed that wavelength is in units of nm, and that the desired wavenumber has units of cm^{-1}. The factor 10^7 is only required to convert the order of magnitude in these units, and should be adjusted if working in anything other than nm to cm^{-1}. Also recall these are single averaged values for each the A and B-bands, so interpolation along the wavenumber array is not necessary.

Figure A.3 shows examples of attenuated solar flux spectra at various altitudes. Note the Lyman-α line is represented as a profile, since it occurs at only one wavelength. Also note the attenuation in the A and B-bands has higher resolution due to the high-resolution absorption calculations and are in terms of wavenumber rather than wavelength.

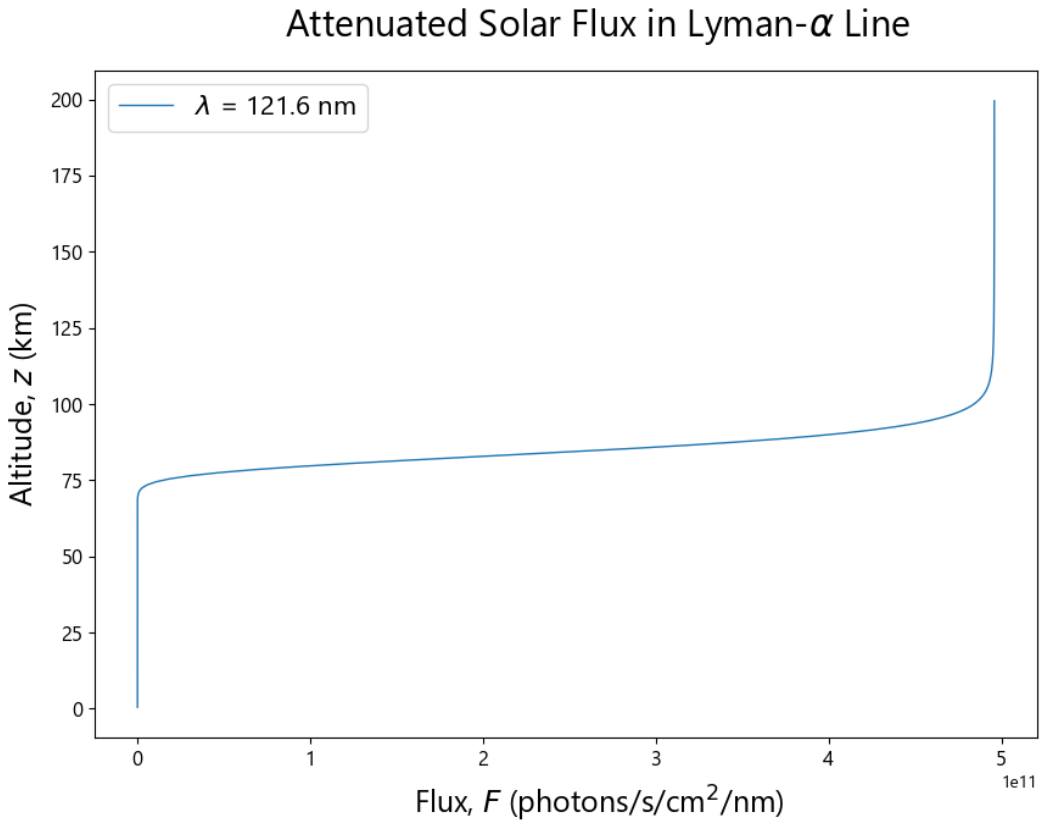

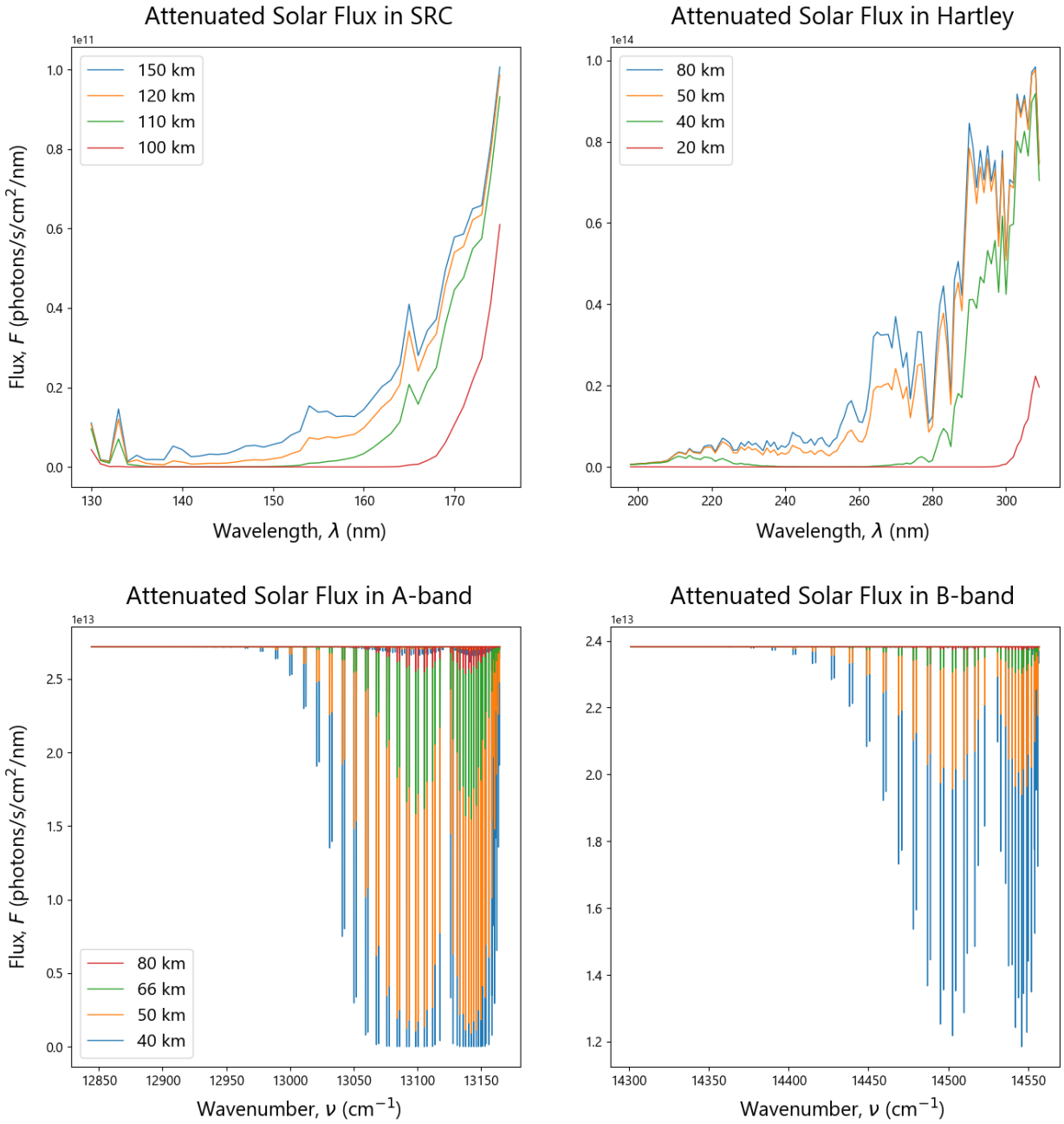

Figure A.3: Attenuated solar flux spectra in five regions of interest at varying altitudes.

A.4.2 Photochemical Reaction Rates and Photolysis Coefficients

The g-factors for photon absorption in the A and B-bands have rate units of s^{-1} and their formulas can be presented more explicitly for their respective spectral regions:

$$g_{\mathrm{A}}(z) = \int_{\nu_{\mathrm{A}}} F_{\mathrm{A}}(\nu, z)\sigma^{\mathrm{A}}_{\mathrm{O}_2}(\nu, z)\, d\nu' \tag{A.10}$$

$$g_{\mathrm{B}}(z) = \int_{\nu_{\mathrm{B}}} F_{\mathrm{B}}(\nu, z)\sigma^{\mathrm{B}}_{\mathrm{O}_2}(\nu, z)\, d\nu' \tag{A.11}$$

The coefficients for photolysis in the Lyman-α line, Schumann-Runge continuum (SRC), and Hartley bands are found similarly, but also depend on the unitless quantum yield, ϕ. Their equations can be stated more explicitly as:

$$J_{\mathrm{L}}(z) = F_{\mathrm{L}}(z)\ \sigma^{\mathrm{L}}_{\mathrm{O}_2}\ \phi_{\mathrm{L}} \tag{A.12}$$

$$J_{\mathrm{S}}(z) = \int_{\lambda_{\mathrm{SRC}}} F_{\mathrm{S}}(\lambda, z)\sigma^{\mathrm{S}}_{\mathrm{O}_2}(\lambda)\phi_{\mathrm{S}}\, d\lambda' \tag{A.13}$$

$$J_{\mathrm{H}}(z) = \int_{\lambda_{\mathrm{Har}}} F_{\mathrm{H}}(\lambda, z)\sigma^{\mathrm{H}}_{\mathrm{O}_3}(\lambda)\phi_{\mathrm{H}}(\lambda)\, d\lambda' \tag{A.14}$$

Note that the photolysis coefficient J_{L} for Lyman-α in Equation A.12 does not require spectral integration, as it only concerns one wavelength.

References

Alpers, M., Gerding, M., Hoffner, J., and Von Zahn, U. (2000). NLC particle properties from a five-color lidar observation at 54°N. *Journal of Geophysical Research*, 105:12,235-12,240.

ARG (Atmospheric Research Group) (2018). Welcome to SASKTRAN's Documentation! *Institute for Space and Atmospheric Studies, University of Saskatchewan.* Retrieved from: arg.usask.ca/docs/sasktran/.

Babcock, H. D. and Dieke, G. H. (1927). The structure of the atmospheric absorption bands of oxygen. *Proceedings of the National Academy of Sciences of the United States of America,* 13:670-678.

Babcock, H. D. and Herzberg, L. (1948). Fine structure of the red system of atmospheric oxygen bands. *Astrophysical Journal,* 108:167-190.

Barth, C. A. and Hildebrandt, A. F. (1961). The 5577 Å Airglow Emission Mechanism. *Journal of Geophysical Research*, 66:985-986.

Bathgate, A. F. (2010). *Modeling Polarized Radiative Transfer for Improved Atmospheric Aerosol Retrieval with OSIRIS Limb Scattered Spectra.* MSc thesis, University of Saskatchewan, Saskatoon, Saskatchewan.

Bernath, P. F. (2005). *Spectra of Atoms and Molecules.* Oxford University Press, New York, New York.

Bourassa, A. E., Degenstein, D. A., Gattinger, R. L., and Llewellyn, E. J. (2007). Stratospheric aerosol retrieval with optical spectrograph and infrared imaging system limb scatter measurements. *Journal of Geophysical Research*, 112:D10217.

Bourassa, A. E., Degenstein, D. A., and Llewellyn, E. J. (2008). SASKTRAN: A spherical geometry radiative transfer code for efficient estimation of limb scattered sunlight. *Journal of Quantitative Spectroscopy and Radiative Transfer,* 109:52-73.

Bourassa, A. E., McLinden, C. A., Sioris, C. E., Brohede, S., Bathgate, A. F., Llewellyn, E. J., and Degenstein, D. A. (2011). Fast NO_2 retrievals from Odin-OSIRIS limb scatter measurements. *Atmospheric Measurement Techniques*, 4:965-975.

Brasseur, G. P. and Solomon, S. (2005). *Aeronomy of the Middle Atmosphere*. Springer, Netherlands.

Brion, J., Chakir, A., Daumont, D., Malicet, J., and Parisse, C. (1993). High-resolution laboratory absorption cross section of O_3. Temperature effect. *Chemical Physics Letters*, 213:610-612.

Bucholtz, A., Skinner, W. R., Abreu, V. J., and Hays, P. B. (1986). The dayglow of the O_2 atmospheric band system. *Planetary and Space Science*, 34:1031-1035.

Burch, D. E. and Gryvnak, D. A. (1969). Strengths, Widths, and Shapes of the Oxygen Lines near 13,100 cm(-1) (7620 A). *Applied Optics*, 8:1493-1499.

Chapman, S. (1931). Bakerian Lecture - Some Phenomena of the Upper Atmosphere. *Proceedings of the Royal Society of London*, 132.

Cho, J. Y. N. and Rottger, J. (1997). An updated review of polar mesosphere summer echoes: Observation, theory, and their relationship to noctilucent clouds and subvisible aerosols. *Journal of Geophysical Research,* 102:2001-2020.

Christensen, A. B., Yee, J., Bishop, R. L., Budzien, S. A., Hecht, J. H., Sivjee, G., and Stephan, A. W. (2012). Observations of molecular oxygen atmospheric band emission in the thermosphere using the near infrared spectrometer on the ISS/RAIDS experiment. *Journal of Geophysical Research, Space Physics,* 117:A04315.

Daumont, D., Brion, J., Charbonnier, J., and Malicet, J. (1992). Ozone UV Spectroscopy I: Absorption Cross-Sections at Room Temperature. *Journal of Atmospheric Chemistry*, 15:145-155.

Degenstein, D. A., Bourassa, A. E., Roth, C. Z., and Llewellyn, E. J. (2009). Limb scatter ozone retrieval from 10 to 60 km using a multiplicative reconstruction technique. *Atmospheric Chemistry and Physics,* 9:6521-6529.

Dieke, G. H. and Babcock, H. D. (1927). The structure of the atmospheric absorption bands of oxygen. *Physics*, 13:670-678.

Evans, W. F. J. and Llewllyn, E. J. (1973). Atomic Hydrogen Concentrations in the Mesosphere and Hydroxyl Emissions. *Journal of Geophysical Research,* 78:323-326.

Goody, R. M. and Yung, Y. L. (1995). *Atmospheric Radiation*. Oxford University Press, New York, New York.

Green, J. G., Shi, J., and Barker, J. R. (2000). Photochemical Kinetics of Vibrationally Excited Ozone Produced in the 248 nm Photolysis of O_2/O_3 Mixtures. *The Journal of Physical Chemistry,* 104:6218-6226.

Kauffman, M., Gusev, O. A., Grossmann, K. U., Martin-Torres, F. J., Marsh, D. R., Kutepov, A. A. (2003). Satellite observations of daytime and nighttime ozone in the mesosphere and lower thermosphere. *Journal of Geophysical Research,* 108:4272.

Kernahan, J. A. and Pang, P. H. (1975). Experimental Determination of Absolute *A* Coefficients for 'Forbidden' Atomic Oxygen Lines. *Canadian Journal of Physics,* 53:455-458.

Khomich, V. Y., Semenov, A. I., and Shefov, N. N. (2008). *Airglow as an Indicator of Upper Atmospheric Structure and Dynamics*. Springer, Berlin.

Kramer, H. J. (2015). MATS (Mesospheric Airglow/Aerosol Tomography and Spectroscopy) Mission. *Earth Observation Portal*. Retrieved from: directory.eoportal.org/web/eoportal/satellite-missions/m/mats.

Lacoursiere, J., Meyer, S. A., Faris, G. W., and Slanger, T. G. (1999). The O(^{1}D) yield from O_2 photodissociation near H Lyman-α (121.6 nm). *Journal of Chemical Physics*, 110:1949.

Llewellyn, E. J., Lloyd, N. D., Degenstein, D. A., Gattinger, R. L., Petelina, S. V., ..., and Nordh, L. (2004). The OSIRIS instrument on the Odin spacecraft. *Canadian Journal of Physics*, 82:411-422.

Malicet, J., Daumont, D., Charbonnier, J., Parisse, C., Chakir, A., and Brion, J. (1995). Ozone UV Spectroscopy II: Absorption Cross-Sections and Temperature Dependence. *Journal of Atmospheric Chemistry*, 21:263-273.

McClatchey, R. A., Benedict, W. S., Clough, S. A., Burch, D. E., Calfee, R. F., ..., Garing, J. S. (1973). *AFCRL Atmospheric Absorption Line Parameters Compilation*. Air Force Cambridge Research Laboratories, Bedford, Massachusetts.

McDade, I. C., Murtagh, D. P., Greer, R. G. H., Dickinson, P. H. G., Witt, G., Stegman, J., Llewellyn, E. J., Thomas, L., and Jenkins, D. B. (1986). Eton 2: Quenching Parameters for the Proposed Precursors of $O_2(b^1\Sigma)$ and O(^{1}S) in the Terrestrial Nightglow. *Planetary and Space Science*, 34:789-800.

Nappo, C. (2002). *An Introduction to Atmospheric Gravity Waves, Volume 102*. Academic Press, San Diego.

NASA (National Aeronautics and Space Administration) (2015). India-Pakistan Border at Night. *NASA Earth Observatory.* Retrieved from: earthobservatory.nasa.gov/ images/86725/india-pakistan-border-at-night.

Nicholls, R. W. (1965). Franck-Condon Factors to High Quantum Numbers VI: C_2 Band Systems. *Journal of Research of the National Bureau of Standards – A. Physics and Chemistry*, 69:397-400.

Nishida, S., Taketani, F., Takahashi, K., and Matsumi, Y. (2004). Quantum Yield for O(^{1}D) Production from Ozone Photolysis in the Wavelength Range of 193-225 nm. *Journal of Physical Chemistry*, 106:2710-2714.

OrangeDog. (2009). Spectral lines of hydrogen, divided into series. Shown on a logarithmic scale. Retrieved from https://en.wikipedia.org/wiki/Hydrogen_spectral_series#/media/File:Hydrogen_spectrum.svg

Petty, G. W. (2006). *A First Course in Atmospheric Radiation*. Sundog Publishing, Wisconsin.

Reddmann, T. and Uhl, R. (2003). The H Lyman-α actinic flux in the middle atmosphere. *Atmospheric Chemistry and Physics*, 3:225-231.

Roth, C. Z., Degenstein, D. A., Bourassa, A. E., and Llewellyn, E. J. (2007). The retrieval of vertical profiles of the ozone number density using Chappuis band absorption information and multiplicative algebraic reconstruction technique. *Canadian Journal of Physics*, 85:1225-1243.

Rothman, L. S., Rinsland, C. P., Goldman, A., Massie, S. T., Edwards, D. P., ..., Varnasi, P. (1998). The HITRAN Molecular Spectroscopic Database and HAWKS (HITRAN Atmospheric WorkStation): 1996 Edition. *Journal of Quantitative Spectroscopy and Radiative Transfer*, 60:665-710.

Rymdstyrelsen (2016). Space Activities in Sweden: Mats. *Swedish National Space Board.* Retrieved from: www.snsb.se/en/Home/Space-Activities-in-Sweden/Satellites/Mats.

Sander, S. P., Friedl, R. R., Ravishankara, A. R., Golden, D. M., Kolb, C. E., Kurylo, M. J., ..., Orkin, V. L. (2006). *Chemical Kinetics and Photochemical Data for Use in Atmospheric Studies: Evaluation Number 15*. Jet Propulsion Laboratory, Pasadena, California.

Sheese, P. (2009). *Mesospheric ozone densities retrieved from OSIRIS observations of the O_2 A-band dayglow.* PhD thesis, York University, Toronto, Ontario.

Sheese, P. E., Llewellyn, E. J., Gattinger, R. L., Bourassa, A. E., Degenstein, D. A., Lloyd, N. D., and McDade, I.C. (2010). Temperatures in the upper mesosphere and lower thermosphere from OSIRIS observations of O_2 A-band emission spectra. *Canadian Journal of Physics*, 88:919-925.

Sheese, P. E., Llewellyn, E. J., Gattinger, R. L., Bourassa, A. E., Degenstein, D. A., Lloyd, N. D., and McDade, I.C. (2011). Mesopause temperatures during the polar mesospheric cloud season. *Geophysical Research Letters*, 38:L11803.

Slanger, T. G. and Black, G. (1977). O(1S) in the lower atmosphere – Chapman vs Barth. *Planetary and Space Science,* 25:79-88.

Smith, A. K. (2004). Physics and chemistry of the mesopause region. *Journal of Atmospheric and Solar-Terrestrial Physics,* 66:839-857.

Takahashi, K., Hayashi, S., Matsumi, Y., Taniguchi, N., and Hayashida, S. (2002). Quantum yields of $O(^1D)$ formation in the photolysis of ozone between 230 and 308 nm. *Journal of Geophysical Research*, 107:4440.

Talukdar, R. K., Longfellow, C. A., Gilles, M. K., and Ravishankara, A. R. (1998). Quantum yields of $O(^1D)$ in the photolysis of ozone between 289 and 329 nm as a function of temperature. *Geophysical Research Letters*, 25:143-146.

MISU (Department of Meteorology) (2016). MATS Science. *Stockholm University, Research, MATS.* Retrieved from: www.misu.su.se/research/2.47409/mats-science.

UCAR (University Corporation for Atmospheric Research) (2015). Layers of Earth's Atmosphere. *UCAR: Center for Science Education.* Retrieved from: scied.ucar.edu/atmosphere-layers.

Videlov, K. (2014). Noctilucent Clouds over Stockholm, Sweden. Retrieved from: www.flickr.com/photos/125283887@N08/14448519568.

Wallace, L. and Hunten, D. M. (1968). Dayglow of the Oxygen A Band. *Journal of Geophysical Research,* 73:4813-4834.

Witt, G., Stegman, J., Solheim, B. H. and Llewellyn, E. J. (1978). A Measurement of the $O_2(b^1\Sigma - X^3\Sigma)$ Atmospheric Band and the $O(^1S)$ Green Line in the Nightglow. *Planetary and Space Science,* 27:341-350.

Yankovsky, V. A. and Manuilova, R. O. (2006). Model of daytime emissions of electronically-vibrationally excited products of O_3 and O_2 photolysis: application to ozone retrieval. *Annales Geophysicae, European Geosciences Union,* 24:2823-2839.

Yoshino, K., Parkinson, W. H., Ito, K., and Matsui, T. (2004). Absolute absorption cross-section measurements of Schumann-Runge continuum of O_2 at 90 ad 295 K. *Journal of Molecular Spectroscopy*, 229:238-243.

Zawada, D. J., Dueck, S. R., Rieger, L. A., Bourassa, A. E., Lloyd, N. D., and Degenstein, D. A. (2015). High-resolution and Monte Carlo additions to the SASKTRAN radiative transfer model. *Atmospheric Measurement Techniques*, 8:2609-2623.